UCRL-CR-120949
B239745

Russian Academy of Sciences
Institute for Dynamics of Geospheres

Final Technical Report
June 9, 1994-October 9, 1994

COMPARISON OF THE EFFECTS IN THE ROCK MASS OF LARGE-SCALE CHEMICAL AND NUCLEAR EXPLOSIONS

A. A. Spivak

April 1995

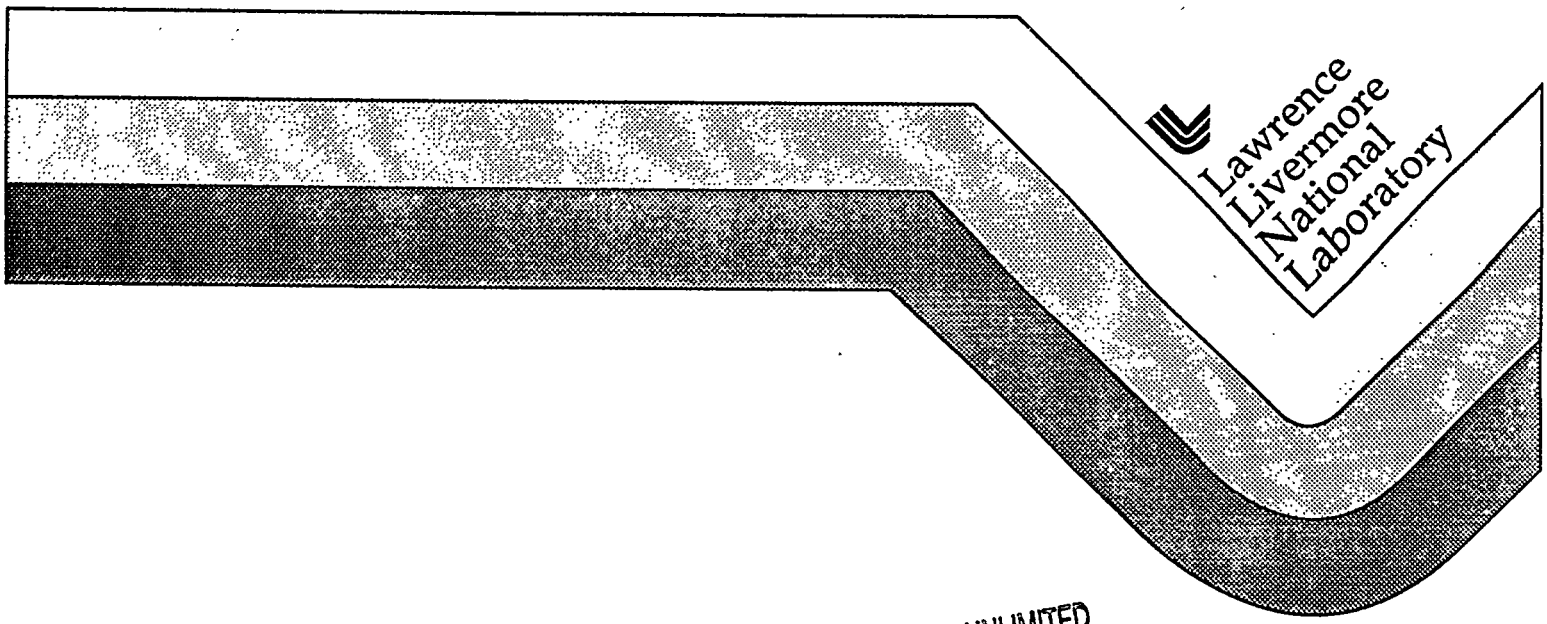

DISCLAIMER

Institute for Dynamics of Geospheres
Russian Academy of Sciences

Finale Technical Report

on the work done through the period
from June 9, 1994 to October 9, 1994
under the contract No. B239745
between the IDG and the LLNL

Comparison of the Effects in the Rock Mass of Large-Scale Chemical and Nuclear Explosions

INSTITUTE FOR DYNAMICS OF GEOSPHERES
RUSSIAN ACADEMY OF SCIENCES
* * *
UNIVERSITY OF CALIFORNIA
LAWRENCE LIVERMORE NATIONAL LABORATORY

COMPARISON OF THE EFFECTS IN THE ROCK MASS OF LARGE-SCALE CHEMICAL AND NUCLEAR EXPLOSIONS

January 1995

Technical Report

CONTRACT No. B239745

Moscow-1995

CONTENTS

INTRODUCTION

Full extent of significant knowledge accumulated by mankind for a long time, when explosions were used in minig and war industry, was used in study of processes, which accompany an underground nuclear explosion. It was found that in the first approximation the mechanical effect of underground nuclear explosion is analogous to the effect of chemical explosion. Really, qualitative analysis shows that accompanying mechanical effects of nuclear and chemical explosions are the same: in the both cases explosion consequences are characterized by formation of the camouflet cavity (crater after explosion near free surface), destruction of the rock massif near explosion centre, creation of the stress wave, which forms seismoexplosive effect a long distance from explosion epicentre. Qualitative likeness of underground nuclear explosions and chemical explosions is the base of modelling the mechanical effects of the underground nuclear explosion.

Later, in model investigations of the influence of underground explosion conditions on the stress wave and medium destruction characteristics, it was founded that there is great influence of the initial energy density in the explosion epicentre on its mechanical effects. At the same time firstly it was raised a question about comparability of the mechanical effects after nuclear and chemical explosions and possibility of the forecasting the action of the underground explosion whith another conditions of its realization on the basis of the data from model experiments (including large-scale) with chemical explosives.

Recently, the interest to comparision the mechanical effects of nuclear and chemical explosions has increased considerably. It is connected with the problem of full and general nuclear tests prohibition, that is elaboration the methods of the nuclear tests control, including tests with different attempts of their concleament. It's not a secret that now, that some countries want to improve nuclear weapon in an underground way, without other members of the Treaty of nuclear tests prohibition. The country, which attempts to realize a secret test and avoid control, apparently will use all possible means to conceal the underground nuclear explosion. One of the successful method of this concealment is an nuclear test realization under cover of large power chemical explosion.

Large-scale underground chemical explosions are used widely in minig (ore mass cutting, stripping and so on) and building (canals, dams construction and so on). When we carry out the control of the observance the Treaty of low power tests prohibition or the Treaty of full and general nuclear tests

prohibition, there is a fear that large power chemical explosions may be used to mask all signals from underground nuclear explosions. In contrast to the earthquakes, these nuclear and chemical explosins may be coordinated in time. There is no doubt, that this method of the deviation from the control creates some difficults for control party. The effect of the tests conclement will be more considerable if the nuclear explosion will be realized in the cavity, since in this case the signal will be decreased by the cavity (decupling effect) and will be masked by a signal from simultaneous large-scale chemical explosion, or even may be put down to this chemical explosion.

The study of the mechanical effect characteristics of nuclear and chemical explosions certantly permits to solve, in future, a problem about principal opportunity to identify an explosion, and to imrove available and create new perspective methods of the nuclear weapon tests control.

In this paper we'll compare two explosions: nuclear (15.04.84) and chemical (27.06.85) with large power. These explosions were realized at the same geological conditions at the Degelen test area, which is a part of the Semipalatinsk Test Site. In the case of the nuclear explosion, the charge was disposed in the face of the deep horizontal gallery. The charge of the chemical explosion was a semisphere from explosives at the rock massif surface. In the both case rock massif behavoir after explosions was investigated at underground conditions (in the case of chemical explosion - in the long underground excavation from explosion epicentre).

Mechanical effects from the nuclear and chemical explosions were investigated with the same methods. It gives an opportunity to do a realiable comparison of the mechanical consequences after these nuclear and chemical explosions. In particular, we'll discuss stress wave characteristics, rock deformations and angular displacements of the excavation walls. Since the deformation of the real rock with block structure under external forces acts mainly along zones of the structural destructions and zones of the strength characteristics decrease, in these experiments medium deformations at the tectonics faults and large cracks were studied espessially.

The changes in geological medium after a large-scale explosive actions will be analysed in detail too. For this purpose engineering and geological characteristics of the rock massifs and their parts before and after explosions will be compared. Also we'll discuss some problems, connected with influence of tectonic structure of the rock massif on the destroying action of the explosion and deformation.

Investigations of the influence of tectonic energy on the mechanical effects after underground nuclear explosions represents the main interest. In this paper we'll discuss this question on the data from underground nuclear explosion, realized 08.09.89 in the deep well at the Balapan test area, at the Semipalatinsk Test Site. The influence of the tectonic energy on the parameters of seismo-explosive wave passing through deep tectonic fault and the release of the stored elastic energy after explosion were analysed in this experiment.

This work is considered by the authors as the first attempt to compare the mechanical effects after underground nuclear and large-scale chemical explosions. So, there are not solution of all appeared problems in this paper. But our results show that it is necessary to compare mechanical effects of the nuclear and chemical explosions and that this problem must be taken into account in the next investigations, especially in preparation some suggestions about nuclear weapon tests control within limits of the Treaty of full and general nuclear tests prohibition.

1. MODEL INVESTIGATIONS OF THE INFLUENCE OF THE ENERGY DENSITY IN THE EXPLOSION SOURCE ON THE EXPLOSIVE EFFECTS IN SOLID MEDIUM

For some methodical reasons, it is impossible to obtain a detailed data of the medium motion parameters and the influence of the explosion realization conditions. So, to study the explosive effects in the zone nearest to the charge (zone of the seismo-explosive source formation) a laboratory experiment was used. It allows to investigate explosive effects in detail and, sometimes, to do general qualitative conclusions comfortable to the problem of comparision of the underground nuclear and large-scale chemical explosions.

It should be noted, that model investigations of the explosion in the real rocks are connected with a numerous dificulties, that arises, in general, because of the necessity to locate recorders in the rock model and to destroy its solid structure, that excludes the use of the microexplosion realization as a source of the disturbance. So, the real rocks are used in model rarely. More frequently, the material, more or less homogeneous, similar to the real rocks and convinent in laboratory experiment is used as a medium. In the present case, such materials were: the colophony, the sodium theio-sulphate and the plexiglass.

Spherical charges of TEN (pressed pentaerythretetranitrite $C_5H_8O_{12}N_4$) with weight q from 0.17 to 2.6 g (the explosive density was equal 400-1500 kg/m^3) were used in these experiments.

The measurement results show that area of the explosive deformation might be divided into two independent parts with different character of the medium deformation in time: at distances, smaller $r = R_*$, medium moves only from explosion epicenter (mass velocity epure typical for the nearest to the charge zone is presented in Fig. 1.1a), but at distances $r > R_*$ phase of the motion from epicenter is replaced by phase of the returned medium motion (Fig. 1.1b), the amplitude of the returned motion tends to increase with incresing of distance from the explosion. Radius of the character area R_* is equal to 11-13 charge radii for sodium theio-sulphate (explosive density is 1500 kr/m^3) or to 4-5 charge radii for plexiglass.

Mass velocities epures show that medium fractions acceleration by the substance speed-up exceeds the acceleration by the substance braking in 6-7 times. It is clearly shown at Fig. 1.2, where normalized times of the growth $\theta_0 = \theta/q^{1/3}$ (curves b) and the duration of the positive motion phase $\tau_0 = \tau/q^{1/3}$ (curves a) in dependence on the normalized distance $r_0 = r/R_0$ are represented. It should be noted, that the duration

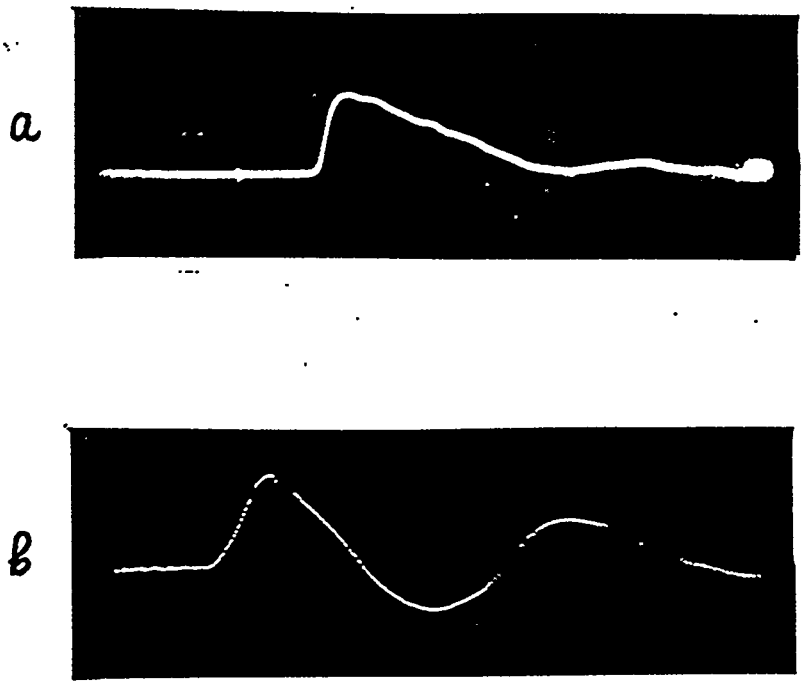

Figure 1.1. Mass velocity oscillograms in the proximal (a) and distal (b) explosion zones.

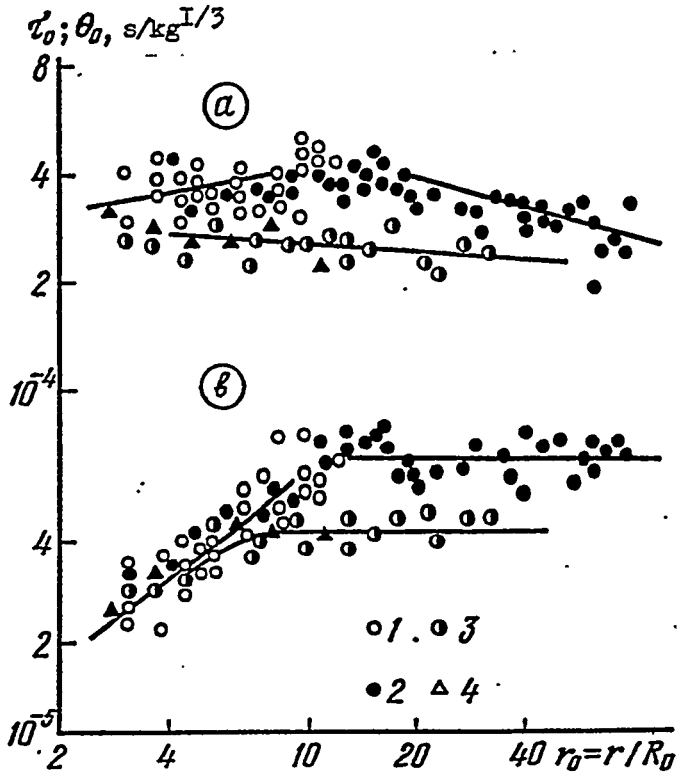

Figure 1.2. The scaled period of positive motion phase (a) and the wave rise time (b) in sodium thiosulfate (1,2) and plexiglass (3,4); detonated PETN charges (density 1500 kg/m^3) are in weight: 1.7×10^{-4} kg; 2.1×10^{-4} kg; 3.4×10^{-4} kg; 2.6×10^{-3} kg.

of the positive motion phase exceeds time of the growth almost in 10 times.

In spite of the fact, that there is an area of the evident medium destruction around explosive charge, no signs of irreversible change in medium because of this destruction are presented in the mass velocity epures. This fact points that either this medium destruction don't break a continuous motion, or the change of the motion parameters at the destruction front is negligible.

Bellow, we'll use the next conventional signs: R - the radius of the wave "front" (coordinate where at the present moment the medium fractions have a maximum velocity v_0), $u_0(r)$ - maximum displacement of the medium fractions at the distance r from the explosion; $r_0 = r/R_0$, $r_* = r/R_*$.

Let's consider the results recived in this experiment. Maximum mass velocities in medium with respect to a distance for the explosion of charge with density of 1500 kg/m^3 are presented in Fig. 1.3. As it can be seen from these curves, for sodium theio-sulphate as well as for plexiglass it's possible to mark out two areas with a different attenuation degree of the compression wave with respect to the distance: around the charge at the distances $r_0 < 12.6$ for the first and $r_0 < 5.5$ for the second medium the attenuation of the mass velocity by the amplitude is more stronger than at the larger distances.

It should be noted, that from these distances returned motion phase is formed in compression wave. The boundary $r = R_*$ will be considered as a boundary of the destruction zone, because it is supposed that outside the destruction zone the material begins to gain an elastic features and, consequently, returned motion phase begins to form into the compression wave.

The treatment of the experimental data gives the next dependences of the maximum mass velocities from a distance:

$$v_0 = \begin{cases} a_0 r_0^{-n}, & \text{when } r_0 < r_* \\ b_0 r_0^{-n}, & \text{when } r_0 > r_* \end{cases}$$

The values of the constants are presented below:

Medium	a_0	b_0	n	p	F_0	s
Theio-sulphate	2300	760	2.16	1.71	0.23	1.88
Plexiglass	3400	1250	2.14	1.57	0.17	1.57

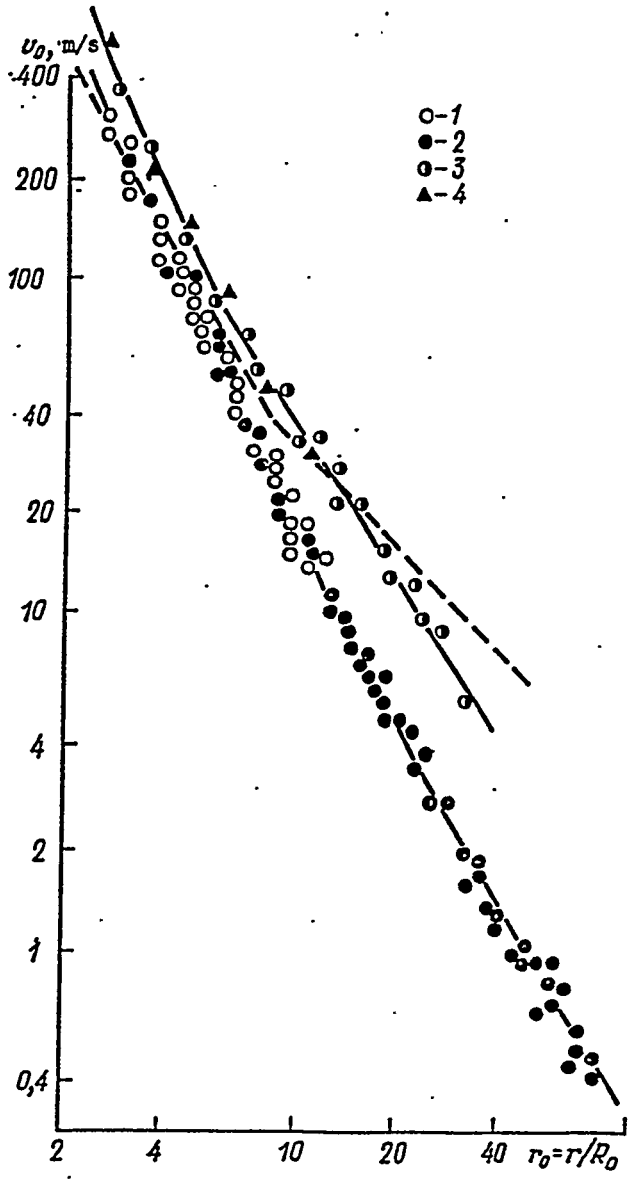

Figure 1.3. Maximum mass velocities in sodium thiosulfate (1,2) and plexiglass (3,4); for notation, see Fig.1.2; dashed curve refers to the maximum mass velocity in rosin.

The experimental results at Fig 1.3 show that maximum mass velocities received in explosions of the charges with different weight, in normal coordinates, lie on the same dependences. It again confirms the truth of the principle of the geometric similarity in the description of the wave motion after a different scale explosions.

The wave disturbance spreading in the medium, results in the displacement of the medium fractures with respect to their primary location. According to the mass velocities epures it is easy to define the value of the medium fractions displacement in each space points with time:

$$u(\omega) = \int_0^w v d\omega,$$

where $\omega = t - r/c$ is the time from the moment of the wave arrival at this distance r; and v is mass velocity.

The dependences $u(\omega)$ for some distances (sodium theio-sulphate) are represented at Fig. 1.4 as an illustration. For times $\omega < \tau/4$ the experimental data are not pointed, since they lay on the averaged dependences, shown by a solid line.

It is the most interesting to consider a maximum and a residual displacements W in the medium after explosion togethe

Since in the area $r < R_*$ no returned motion are observed in the wave, around the charge the next ratio is true:

$$u_0 = \int_0^\tau v d\omega = \int_0^\infty v d\omega = W.$$

When $r > R_*$, the residual displacements are smaller than maximum displacements, because of the returned motion formation.

Maximum displacements in medium received by numerical integration of the mass velocities epures are shown at Fig. 1.5 and in whole area of the explosive motion they are described by the next general ratio:

$$u_0/q^{1/3} = F_0 r_0^{-s} \text{ m/kg}^{1/3}.$$

The values of the constants F_0 and s are presented in the Table at the page 8.

The residual displacements after explosion W are shown in Fig. 1.5 only for the sodium theio-sulphate. But for the both media (theio-sulphate and plexiglass) the following ratio is

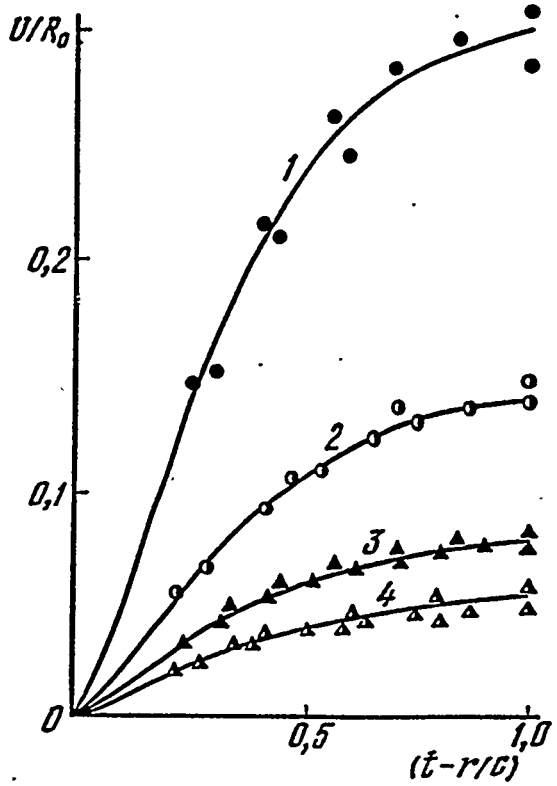

Figure 1.4. The displacement of medium particles within the compressional wave with time at scaled distance r/R_0: 1 - 4.0, 2 - 6.0, 3 - 8.0, 4 - 10.0.

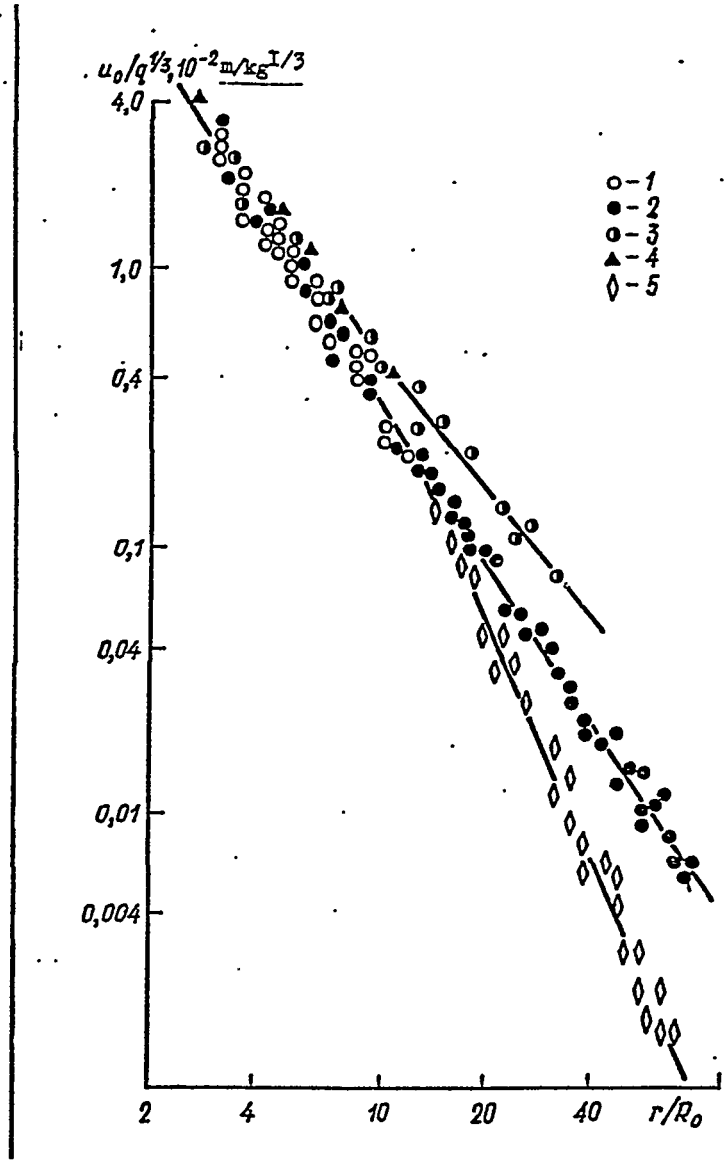

Figure 1.5. Scaled maximum displacements (1-4) and residual displacements (5) in the medium under explosion (for notation, see Fig. 1.2).

correct:

$$W = u_* (r/R_*)^{-2.7},$$

where u_* - the maximum displacement of the boundary $r = R_*$.

In the each fixed time moment, it is possible to construct the distribution of the mass velosity beyond the wave front from the mass velosities epures obtained at different distances from the explosion. The results of this construction are shown in Fig. 1.6 (sodium theio-sulphate). The distribution $v(r)$ has a smooth character (within scattering of the experimental data), and the following power dependences take place near the wave front:

$$v(r) = v_0 (R) \left[\frac{r}{R}\right]^{-k}.$$

For $R < 15R_0$, this ratio is correct in all area of the medium motion. In this case the exponent k is about 1.4. For $R > 15R_0$, in the nearest to the wave front area, the exponent k decreases with increasing of the wave front radius.

In the case of the nuclear charge use, the process of the explosive source formation is accompanied by the decrease of the material density in the explosion centre when the camouflet cavity walls are expanded. It is important, that the shock wave with a large amplitude in the nearest to the charge chamber area itself is the source of the gaz working body because of the evaporation and decomposition of some rock components. Therefore, the charge chamber of the underground nuclear explosion can't be considered as a source of the mechanical action as it is convinient for the chemical explosions. The source definition in this case is directly connected with the analysis of the explosive action with change of the main characteristic of the epicentre - that is volume density of the explosion energy. In this sense, the use of the chemical explosives in underground explosion model gives certain possibities.

In further, initial density of the energy in the explosion centre will be characterized by effective density of the explosives loading, defined as

$$\rho_1 = q/V_0,$$

where V_0 - the volume of the charge chamber.

The basic parameters of the medium motion after the

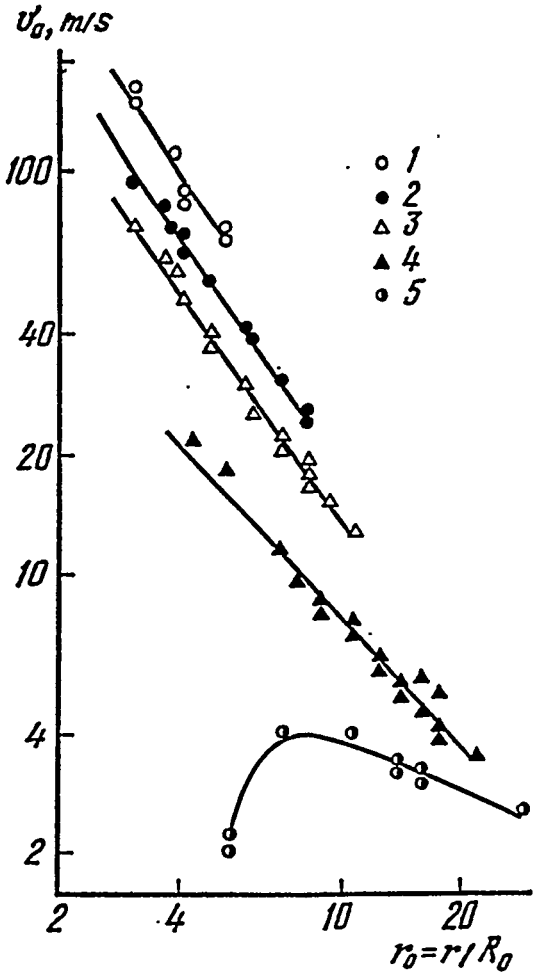

Figure 1.6. The mass velocity distribution behind the wave front, r/R_0: 1 - 5.0; 2 - 8.0; 3 - 11.0; 4 - 22.0; 5 - 27.0.

explosion of the charge with density of 1500 kg/m^3 were determined previously. Further, we'll consider the results of the model investigations of the combined charge explosion, with charge density equal to 400 kg/m^3 (poured TEN), 500 kg/m^3 (poured double-precipated TEN) and 1000 kg/m^3 (pressed TEN).

The basic parameters of the stress waves in the medium (sodium theio-sulphate) v_o and u_o, obtained from mass velocities measurements with respect to the normalized distance $r_o = r/R_o$, are presented at Fig. 1.7 and 1.8. For comparison, stress wave parameters for the explosion of charge with density ρ_1 = 1500 kg/m^3 are shown at the figure by a dotted lines.

It should be noted, that with the decrease of the loading density, the intensity of the explosive action in medium decreses too. It corresponds to conceptions about decay of the rupture at the boundary "detonation products - solid medium" with a different explosives density.

The decrease of the stress wave intensity with the reduction of the loading density results in the decrease of the destruction zone volume and, therefore, of the efficiency of the explosion destructive effect. Radius of the destruction zone R_* estimated on the changes of the attenuation power of the maximum mass velocities, is shown at Fig. 1.9 in dependence on the values of parameter ρ_1.

Fig. 1.10 and 1.11 present a maximum velocity of the charge chamber walls displacement v_p and normalized wave duration $\tau/q^{1/3}$ at the distance $r = R_*$, correspondingly.

The dependences $R_*(\rho_1)$ and $\tau(\rho_1)$ obtained from experiments allow to write the next formulas, convenient for estimations:

$$R_o/R_* = 0.11\rho_1{}^{0.65}; \quad \tau/q^{1/3} = 4\cdot10^{-5}\rho_1{}^{0.3} \text{ s/kg}^{1/3},$$

where ρ_1 is the loading density measured in kg/m^3.

The maximum velocity of the charge chamber walls displacement, shown at Fig. 1.10 by a solid line, is following:

$$v_p = 0.25\ \rho_1{}^{1.4} \text{ m/s},$$

where ρ_1 is measured in kg/m^3.

The parameters of the explosive effect, shown at Fig. 1.7-1.11, point, that the effective loading density considerably influences on the basic characteristics of the explosive effects from underground explosion. So, it should be expected, that the similar characteristics of the nuclear and large-scale explosions are different.

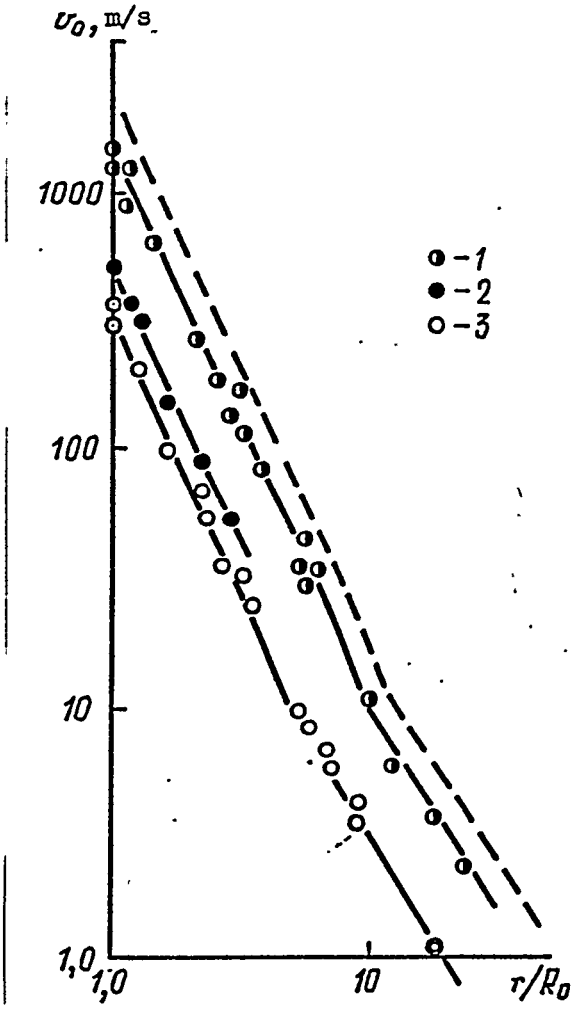

Figure 1.7. Maximum mass velocities in sodium thiosulfate under explosion; PETN density, $10^3 \cdot kg/m^3$: 1 - 1.0; 2 - 0.5; 3 - 0.4.

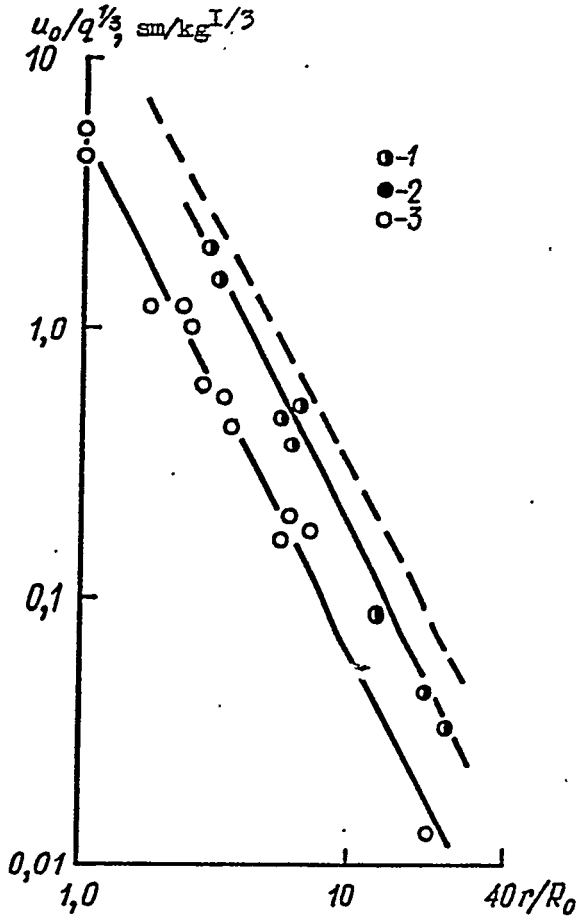

Figure 1.8. Scaled maximum displacements in sodium thiosulfate under explosion (for notation, see Fig. 1.6).

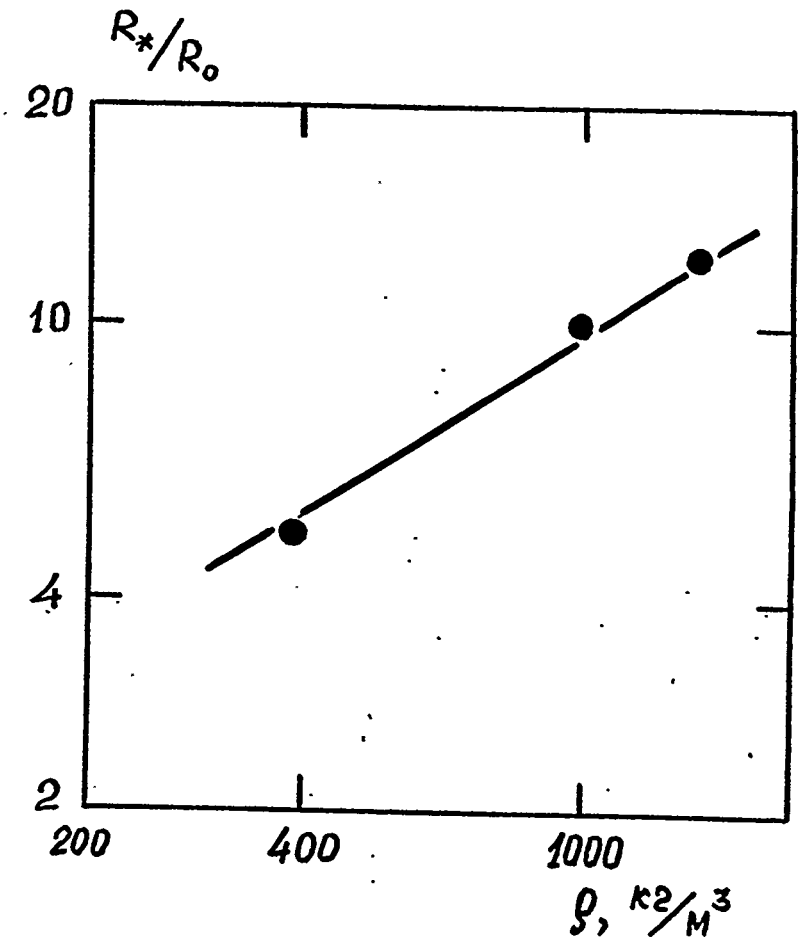

Figure 1.9. Relative radius of the destruction zone in dependence on the values of effective density of charge.

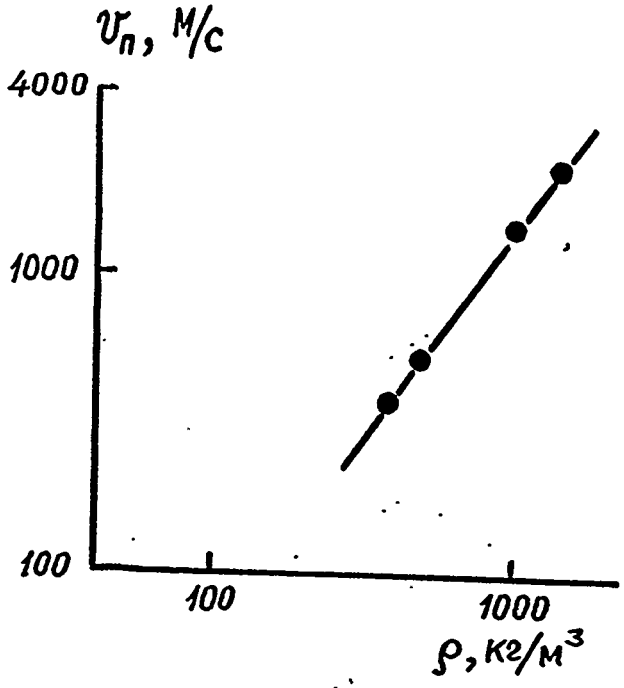

Figure 1.10. Velocity of the crarge chamber walls.

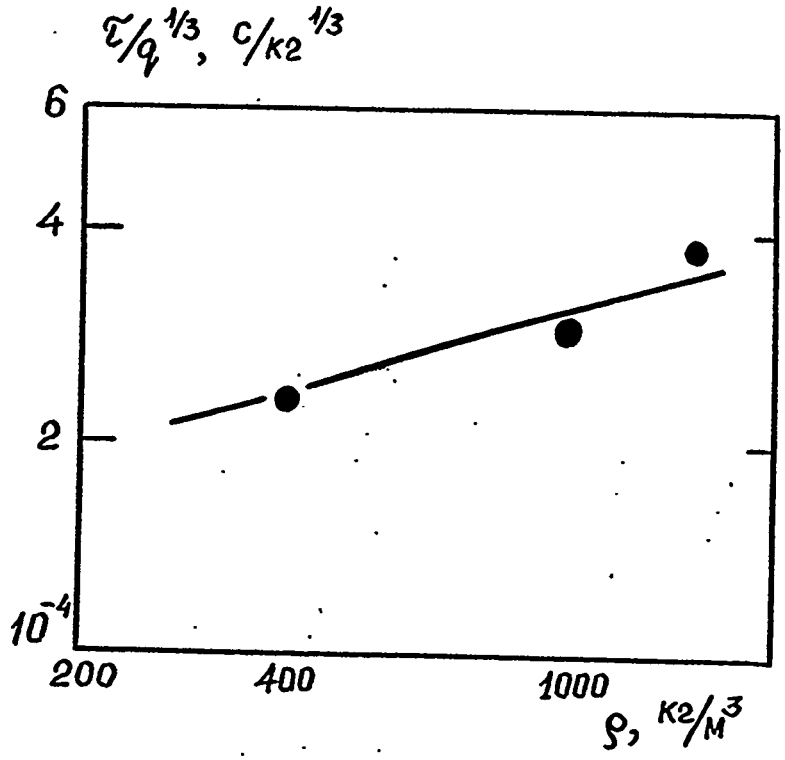

Figure 1.11. Normalized wave duration of the positive phase of motion in compressive wave at the distance $r = R_*$.

2. GEOLOGICAL CHARACTERISTICS OF THE SEMIPALATINSK TEST SITE

The Semipalatinsk Test Site contains a number of spatially distant test areas. The Balapan (for realization of underground nuclear explosions in the deep vertical wells) and the Degelen (for realization of nuclear and large-scale chemical explosions in galleries) localities are the major among them. The scheme of the test areas is given at Fig. 2.1.

The test site is located within the Shagan-Kazakhstan interfluve in the eastern part of the Central Kazakhstan low hills, that are a socle lowland region with absolute altitudes from 500 to 1000 m. The large altitude of some rock massifs exceeds even 1300 m. The erosional dissection is, in whole, shallow and varies within a range of 50-200 m, but sometimes it reaches 500 m.

In spite of the absence of flat relief characteristics in the morphological surface complexes, in whole this region may be considered as a lowland with the evident block differentiation. The fact that the Earth's crust is similar to the mountain system rather than pediment plains confirms this conclusion too. The Earth's crust thickness varies within a range of 46-55 km.

From a geologo-structural viewpoint, this region is related to the eastern part of the Central Kazakhstan elevation, formed in the Caledonian Central Kazakhstan folded system. Only a north-eastern part of this territory extends to the Hercynian Zaisan folded structure. The boundary between the regions of the differen age passes along the deep Kolba-Chingiz fault (Fig. 2.1).

The block structure of the morphostructural territory plane is its main specific feature (Fig. 2.2). The block is considered as a fragment of the Earth's crust upper part bounded by faults. This unit has an individual tendency and temp of the tectotic motions against a background of general macrostructure development. In relief, the blocks are expressed by free-standing mountains, uplands and massifs of them, steps of the mountain and cavity slopes, separate cavities, expansions of the bottoms and watershed areas.

The shape and size of the block in plane reflect, to a some degree, the character of the region stresses. It confirms the fact, that block shape varies in dependence the distance from the regional structural seams. Oblong blocks are more frequent along structural seams, whereas isometric blocks are more typical to the central parts of the boulder uplifts. The block size near the seams tends to decrease. These data test the predominant origin of the blocks under geodynamical conditions

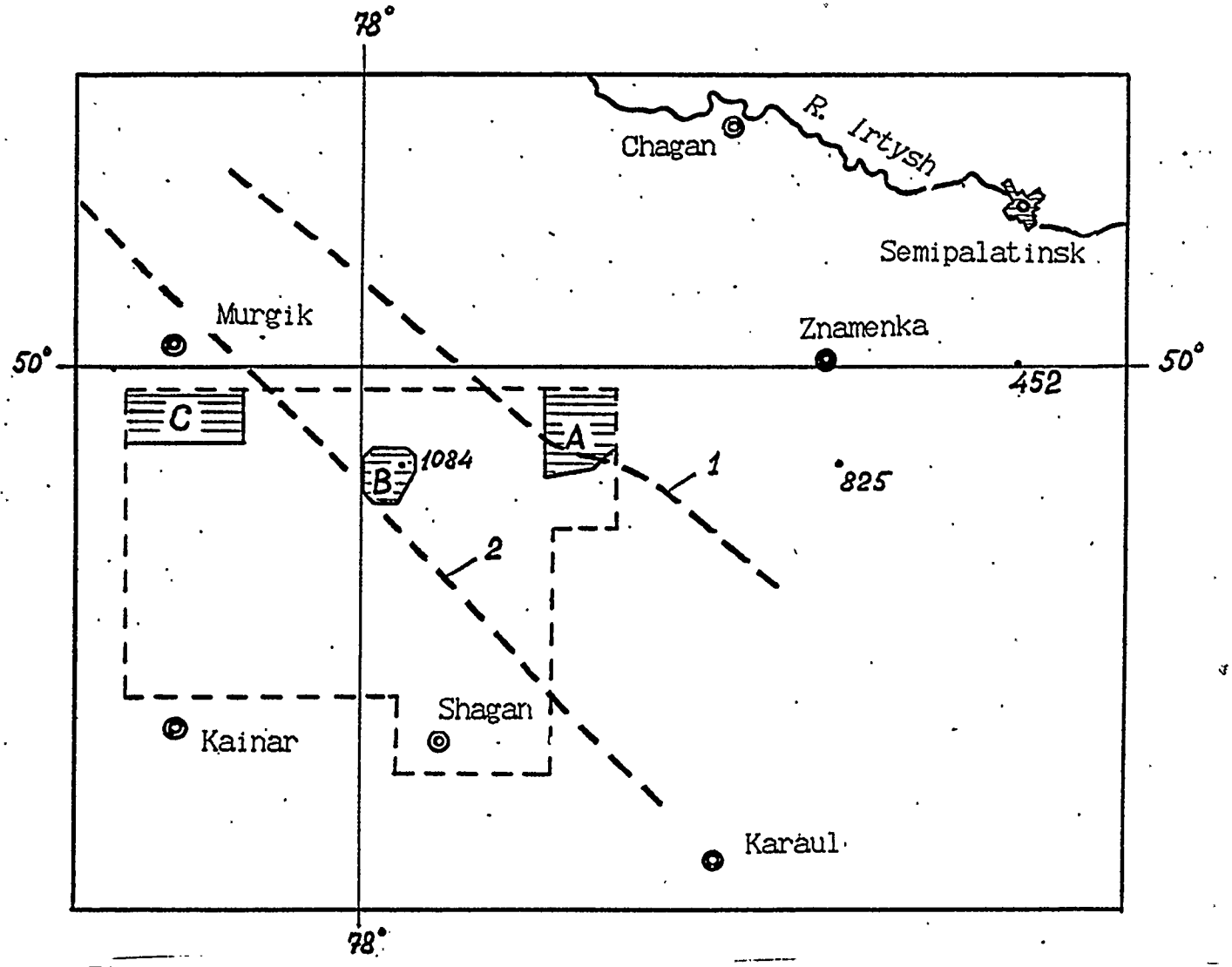

Figure 2.1. Semipalatinsk Test Site (parts, marked by A and B, are the main test areas: Balapan Test site and Degelen Test site, correspondingly);
1 - Kolba-Chingiz deep tectonic fault,
2 - Chingiz tectonic fault,
891 - absolute heights of the mountains (m).

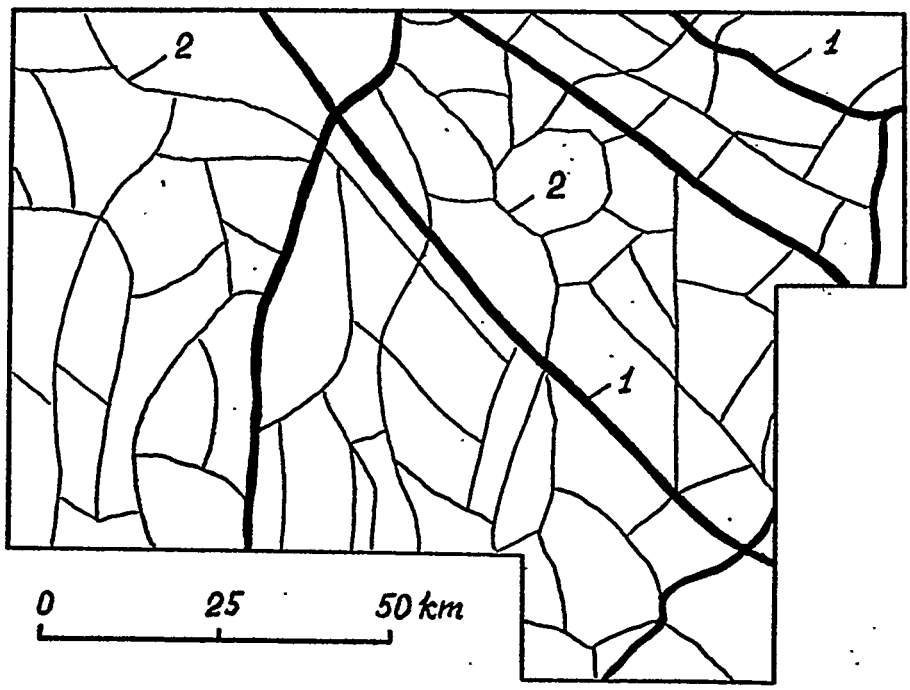

Figure 2.2. Morphostructural scheme of the Semipalatinsk Test site:
1 - tectonic faults,
2 - boundaries of the mesostructures.

of regional compression and extension in the upper parts of the Earth's crust.

2.1 Rock characteristics of the Degelen area

The geological situation at the Degelen test area is defined by its location. It is located, in general, within a rounded intrusive massif of about 20 km in diameter. From the geologist's viewpoint, the intrusive massif is a jut of the Earth's crust aganst a background of a collapse caldera composed of sedimentary and sedimentary-effusive formations.

Rocks of the intrusive massif, in its the biggest western part, outcrops and are represented by granites of the Upper Paleozonic age and by granite-porphyries of the Lower Carboniferous age (Fig. 2.3). In this part, host rocks (predominantly acidic effusive rocks) are retained in the thin cover as a bounded rare areas. In the eastern part of essentially smaller size, and along the southern and northern bounders of the intrusive area, thickness of the enclosing rocks increases. In this part the rocks trace as a nearly continued cover and are represented not only by acidic rocks, but also by the basic effusive rocks of the Lower Carboniferous system.

In the Upper Paleozonic granits, a rupture tectonics is expressed claerly. The tectonic ruptures are also traced in the field of the effisive formations development in the eastern part of the area and form a general system of the structural tectonic blocks (Fig. 2.3).

Except a large tectonic ruptures, there are (espessially in granites) a great number of the small ruptures variously oriented in space. The main factor of the rupture formation in granite appears to be drop in stress at the granite massif after its uplifting during the collapse caldera formation.

The granites are intruded by porphyrite and microgranite dikes and, rarely, by quarts veins. The dike and veins thickness varies from 0.2 to 5 m. Incident azimuth commonly is equal to 220-290° at an angle of 20-60°. The contacts of dikes and host granites are explicit, without visible rock alterations.

The rock-made minerals are: feldspar (65-75%), quartz (25-30%), and biotite (1-3%).

All rock massifs of the Degelen test area are composed of homogeneous intrusive and effusive rocks of magmatic genesis and are classified as hard rocks with high strength (Table 2.1).

According to the classification in Table 2.2, there are

Table 2.1. Phisico-mechanical properties of the Degelen rock system.

Rock type	Density, kg/m^3	Porosity, %	Water content, %	Strength to the one-axis compression, MPa		Velocity, m/s		Young's modulus, GPa	Poisson's ratio
				in the dry state	in the water saturated state	P-wave	S-wave		
Granit	2560	3.42	0.30	119	129	4900	2800	51	0.26
Quartz porphyrite	2660	2.11	0.22	148	110	5200	2800	56	0.29
Andesite porphyrite	2890	-	0.09	210	130	5700	3000	66	0.29
Diabasic porphyrite	2880	0.74	0.26	105	98	5000	2700	55	0.29

Table 2.2. Classification of the structural blocks, faults, and cracks.

Order of block structures	Order of the disturbance of the massif solidity	Disturbance length	Thickness of the zone of the faults breaking up and cracks width
I	faults of order I, deep, seismogenic	Hundreds and thousands of kilometers	hundreds and thousands of meters
II	faults of order II, deep seismogenic and non-seismogenic	tens and hundreds of kilometers	a few meters and tens of meters
III	faults of order III	a few kilometers and tens of kilometers	a few meters and tens of meters
IV	faults of order IV	hundreds and thousands of meters	tens and hundred of centimeters
V	small faults and large cracks of order V	tens and hundreds of meters	tens of centimeters
VI	mean cracks of order VI	a few meters and tens of meters	a few milimeters and a few centimeters
VII	small cracks of order VII	a few centimeters and a few meters	parts of milimeters and a few milimetres
VIII	thin cracks of order VIII	less than tens centimeters	less than two milimeters

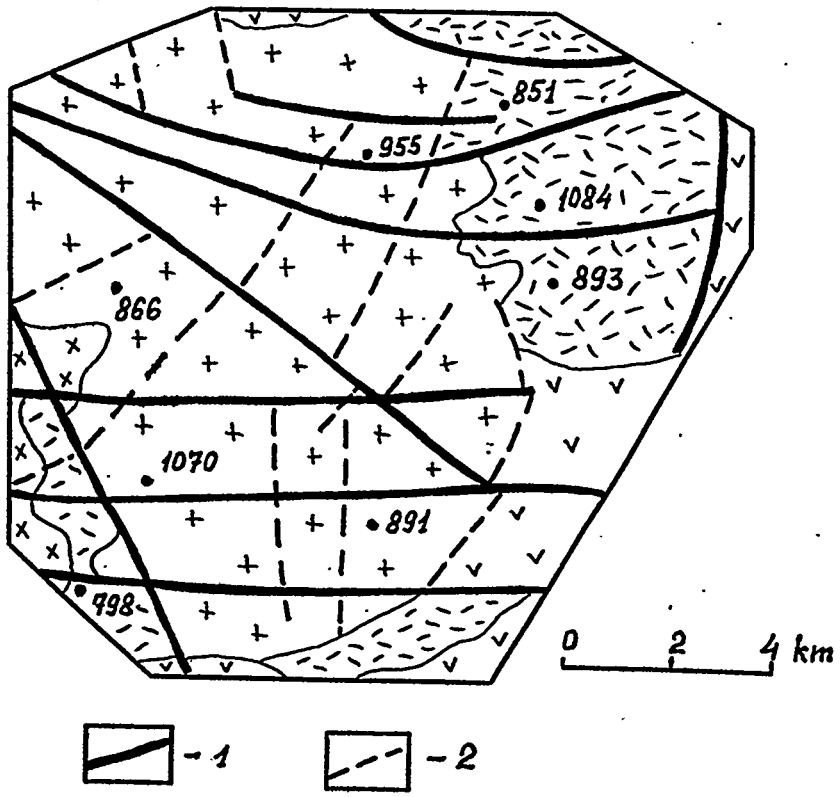

Figure 2.3. Scheme of the tectonic disturbances at the Degelen Test site:
1 - main tectonic faults,
2 - accompanying faults;
Geological formations:
3 - granites of the Upper Paleozonic age;
4 - granites of the Lower Carboniferous age;
5 - acidic effusive rocks of the Lower Carboniferous age;
6 - basic and mean effusive rocks of the Lower Carboniferous age;
7 - boundaries between different geological formations;
·891 - absolute heights of the mountains (m).

structural blocks of order III - VIII in the Degelen mountain massif structure. Tectonic ruptures, which bound blocks of order III-IV and often blocks of order V, are realiably indentified in aerial photographs and in visial investigations of the rock massif surface.

In the areas covered by underground excavations, position of the tectonic faults in the rock massif can be established with high accuracy. In this case it is possible to define the shape and size of the structural blocks.

Blocks of order III have size in plane about a few tens of square kilometers. The rock excavations for nuclear explosions are, as a rule, situated in the same block of order III, or, more rarely, in two adjucent blocks of order III such that only one boundary of order III is uncovered by the excavation.

Size of blocks of order IV varies in plane from (200-300)×(300-600) m^2 to (450-600)×(800-1500) m^2. Probably, the vertical block size is comparable with the maximum depth of the excavation.

Blocks of order V have size (15-150)×(40-400) m^2 in plane and (30-300) m in depth. The block shape approximates to an oblique irregular parallelepiped or, sometimes, a truncated prism. The size of blocks of order V varies within the same rock massif essentially. Commonly, the sizes increase with depth.

The mean linear size of blocks of order V varies from 12 to 243 m at the different parts of the Degelen massif (Table 2.3).

Elementary structural blocks of order VII and VIII are the lowest hierarchical level of the Degelen massif structure and may be indentified only in documentation on the excavation exposure or on the massif surface. The size of elementary blocks varies from 0.1×0.2×0.3 m^3 to 1.3×1.5×2 m^3. As an illustration, the mean linear sizes of the elementary structural blocks along the excavations N° 4 and N° 5 are presented in Table 2.3. These sizes were obtained as a result of the size averaging for elementary blocks in the excavation parts 5 km long.

The boundaries of the structural blocks of order III are extensive (10 km or more in length) tectonic faults visible on the rock massif surface as narrow gullies, small ravines or ledges in the terrain relief with the depth up to a few meters. The thickness of the zone of influence for tectonic faults of order III is 2-4 km. The fissuring modulus in this zone reaches 50-100 fissures per meter. From seismoprospect data, the thickness of the zone of influence for tectonic faults of order III is large and equal 6-15 m for the gallery N° 4 (inside the excavation) and 15-40 m on the rock massif surface.

Table 2.3. Mean linear size A of the structural blocks of order V for some parts of the Degelen rock massif.

N°	Date of the explosion	Explosion energy, kT	Gallery length, m	A, m
1	October, 18, 1984	1.6	211	12
2	June, 6, 1985	0.5	170	17
3	October, 16, 1987	1.0	209	52
4	July, 17, 1987	80.0	1238	88
5	November, 11, 1988	15.0	745	106
6	May, 5, 1983	17.0	788	113
7	April, 4, 1984	55.0	1290	116
8	April, 22, 1988	2.5	485	243

The boundaries of blocks of order IV are represented by tectonic faults of about 1 km in length and mixing zone with thickness from a few centimeters to a few tens of meters. The internal structure of zones of order IV is greatly various. It might be a single strong fissure with argillaceous-detrital filler as, for example, in the excavation N° 3 (thickness of the mixing reaches 30 cm and influence zone up to 2-4 m), or two adjacent fissures, as in excavation N° 7 with opening 2 and 3 cm and common influence zone of 15 m in length. Also it might be a fissure healed with a granodirite dike. Really, this situation is observed rather often (excavations N° 4, 5 and 7; the thickness of dikes reaches 3 m, and of influence zones - 15-20 m).

The boundaries of blocks of order V are represented by both tectonic faults and tectonic fissures with a small length (up to a few tens and a few hundreds of meters long). The thickness of the mixing zones is usually equal to 1-2 cm, rarely - 5 cm. The thickness of the influence zones varies within a range of 0.15-0.5 m, the fissuring modulus reaches 10-30 fissures per running meter.

The tectonic structure of some rock excavations are presented at Fig. 2.4-2.5 as an example.

The elementary blocks are bounded by tectonic and litogenic fissures a few of centimeters or a few tens of meters long. In excavations, the fissure thickness varies from fractions of milimeters to 1-2 mm.

Usually, there are 3-5 systems of the closely alternating fissures with the intervals among them about a few tens of centimeters and 3-4 systems of the less frequent fissures, spaced apart to a several meters.

The fissuring system data typical for the Degelen rock massif are given in Table 2.4. It is evident, that fissures of sublatitudial trend with N-N-W incidence and of N-W trend with S-W incidence are the most frequent for this area.

Within the period of 1961-1989, about 200 nuclear tunnel explosions were realized in the Degelen rock massif.

2.2 Rock characteristics of the Balapan area

Rocks of the Devonian, Carboniferous, Triassic, Jurassic, Neogenic and Quaternary ages take part in the formation of the geological structure of the Balapan test area (Fig. 2.6). .

The Konndin suite (C_1 tkn). In the lower part of the

Table 2.4. System of the cracks, formed in the Degelen rock massif.

N°	Elements of the crack system bedding		Object number (according to Table 2.2)
	Azimuth of incidence	Angle of incidence	
1	0 - 30	70 - 80	7
2	15 - 25	5 - 20	7
3	80 - 125	60 - 80	5, 6, 8
4	105 - 140	50 - 80	3, 6, 7
5	120 - 130	25 - 35	8
6	150 - 180	45 - 70	1, 3
7	175 - 210	70 - 80	4, 7
8	180	25 - 30	7
9	180 - 240	75 - 85	5
10	205 - 240	50 - 80	1, 5, 6, 7
11	230 - 260	45 - 65	3, 8
12	260 - 285	50 - 70	1, 4, 8
13	310 - 350	10 - 35	5
14	310 - 350	40 - 70	1, 3, 6

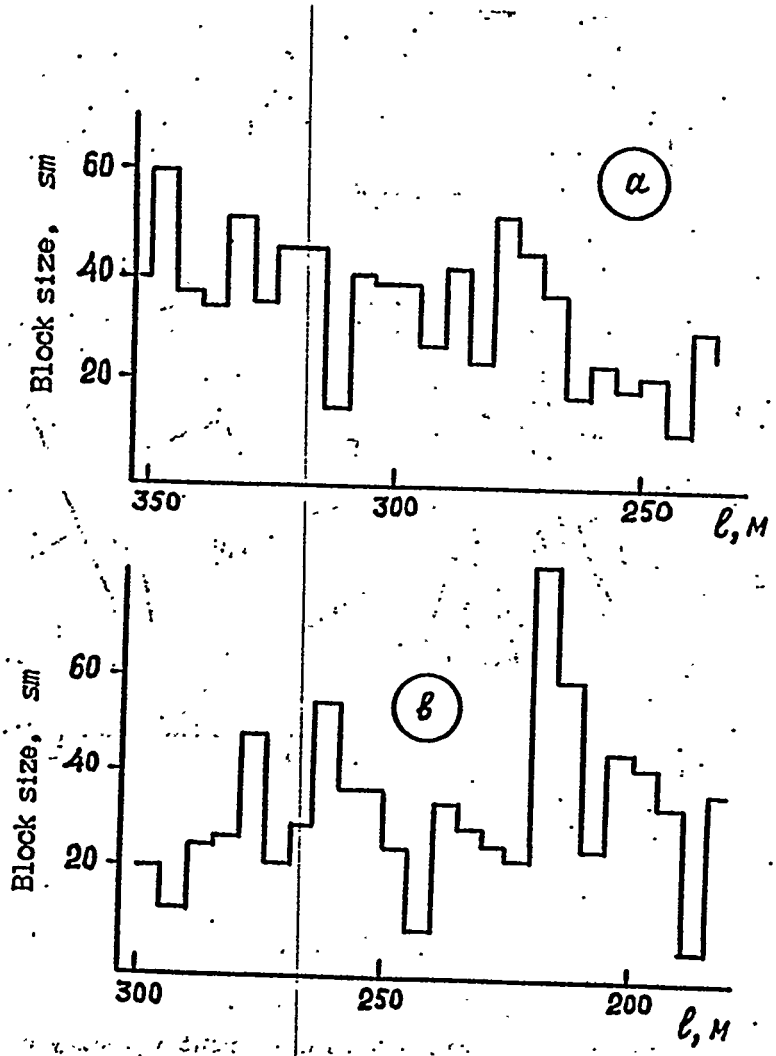

Fig. 2.4

Graphical representation of elementary block structure along the mine workings no. 4 (a) and no. 5 (b).

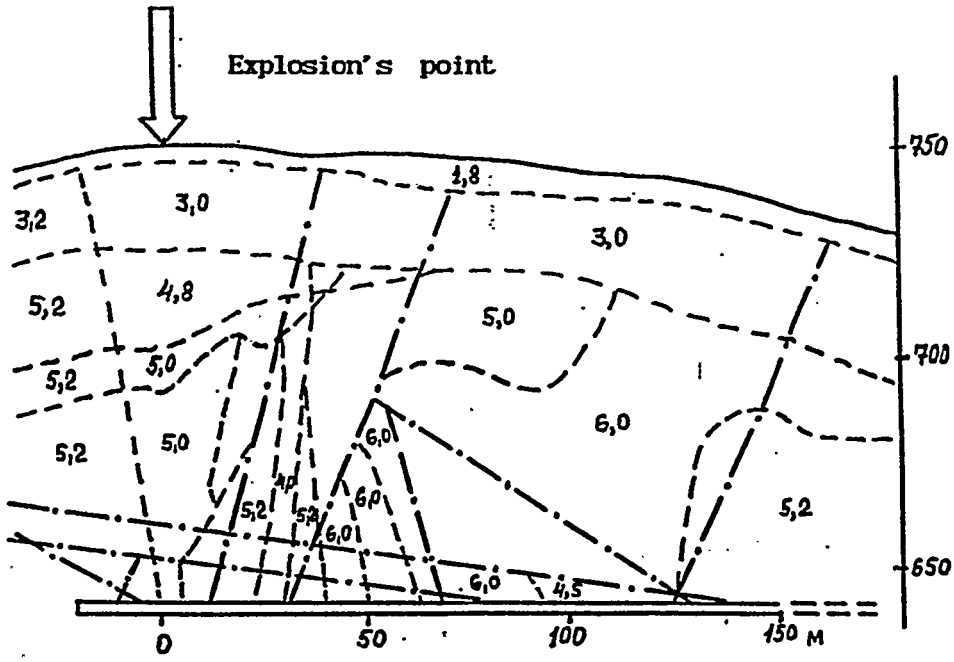

Fig. 2.5

Geologic section of tunnel no. 2;

- tectonic dislocations of order V;

- boundaries of regions with different velocity characteristics or variously affected by explosion;

- contact explosion site of a chemical explosive.

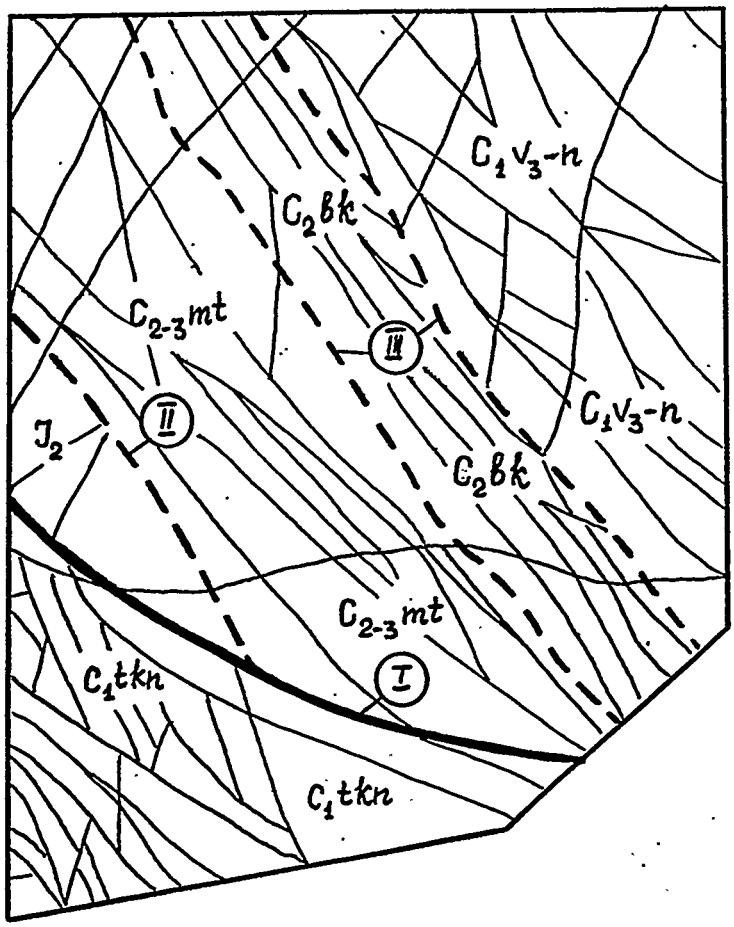

Figure 2.6. Structural-tectonic scheme of the Balapan Test site:
1 - deep tectonic faults;
2 - boundaries of the structural blocks.

geological section, flinty and chlorine-sericitic slates with subordinated interlayers of quartzy sandstones, conglomerates, and limestones are of predominant spreading. In the upper part of the section, the predominant rocks are coal-clay slates, in part with aleurolite and sandstone interlayers and lenses.

The suite deposits are spread in the south-western part of the Balapan test area and their thickness is about 2300 m.

The Kokpektin suite (C_1 v_3-n). The tuffs of basic and medium composition, interlayered with tuff sandstones, and, sometimes, with coal-clay aleurolites, in the lower section are predominantly spread in the north-eastern part of the Balapan test area and are about 3000 m thick.

The Bukon suite (C_2 bk). This suite is represented by aleurolites and sandstones, replaced by conglomerates in the lower part of the geological section. In the central part of the area, the suite rocks form a band of the north-western trend about 3 km wide and about 2000 m thick.

The Maityub suite (C_{2-3} mt). The deposits have molassic features. In the lower part of the section, conglomerates with sandstone and aleurolite lenses and interlayers have a predominant occurrence. Sandstones and aleurolites (often carbonized), coal-clay slates with conglomerate lenses and interlayers predominate in the upper part of the section. There are crush, schistosity and cataclastic zones in the deposits. The deposits range as a band in the eastern part of the Balapan test area and form a tectonic block with north-western extension.

Intrusive rocks are widely spread. They are represented by complexes, that are different in morphology, composition and age:

- granitoids of the Upper Paleozoic age;
- granite intrusion of the Upper Carboniferous age;
- Lower Carboniferous Upper Visean-Namurian complex of subvolcanic minor intrusions;
- subvolcanic Upper Carboniferous porphyrites intrusions of basic and medium composition;
- dike bodies of andesite porphyries of the Permian age.

The underground waters within the studied area are spread everywhere and are uncovered by wells at the depth from 5 to 96 m (most commonly, 20-40 m) depending on neogenic clays thickness.

From the conditions of the underground waters formation and circulation, the waters are classified into the follow types:

- crevice water, confined to the upper fissuring zone of

weathering in the Paleozoic and Mesozoic deposits 40 to 120 m, rarely 150 m, thick;
- crevice-vein water, confined to the zones adjacent to tectonic dislocations and to fractured rock zones;
- pore water, confined to deposits of the Quaternary and Neogenic age.

The crevice waters are of predominant occurrence. They are located in the upper part of the hard-rock formations of the Meso-Paleozoic age. The crevice waters, commonly, have a presure character. Waterproof layer is formed by neogenic clays, that creates unevennesses on the surface of the hard-rock basement. The piezometric levels are formed at the depth from 5 to 33 m and create a head up to 87 m.

The rocks of the Balapan mountain massif are poor aquiferous. The well outputs vary from $1 \cdot 10^{-6}$ to $1.21 \cdot 10^{-3}$ m^3/s when the level falls to 14.7 and 13.7 m, correspodingly. The rocks are characterized by a low water permeability. The filtration coefficients, commonly, vary within a range from $5.8 \cdot 10^{-11}$ m/s to $3.9 \cdot 10^{-7}$ m/s, but sometimes (in fissured rocks and in limestones), the filtration coefficient increases up to $0.35 \cdot 10^{-5}$-$7 \cdot 10^{-5}$ m/s.

The pore waters are confined to loose Cainozoic deposits. In watershed areas, the underground waters of this type are confined to lenses and interlayers of the sand, sandstone and conglomerates at the base of a neogenic clays. The thickness of the water-learing rocks doesn't exceed 20 m, and the spreading of these rocks is sporadical. They are revealed at depth of 11-84 m. The pore waters are pressure-supported, their levels are formed at depth of 3-24 m and create a head within a range of 4-72 m. The well output varies from $1.6 \cdot 10^{-3}$ to $7.7 \cdot 10^{-3}$ m^3/s when the level falls to 18 and 7.9 m, correspodingly. The filtration coefficient of the rocks is equal to 2-20 meters per day.

From a geologic engeneering viewpoint, the Balapan area is characterized by a two-stage structure, that is conditioned by the existance of the hard-rock basement of the Paleozoic and Meozoic age, overlapped by loose cainozoic deposits with thickness varying from a few meters to a hundred meters.

In the upper part of the section all hard rocks are subject to weathering. The thickness of the upper heavily weathered zone varies from 40 to 120 meters. From the seismic data, the third refracting boundary corresponds to the base of the heavily weathered hard rocks. The boundary velocities of the longitudial waves spreading, which characterize rocks underlying the refracting boundary, vary within a range of 4200-6000 m/s. The velocities from 5600 to 6200 m/s correspond to the effusive and intrusive rocks. The velocities from 2800 to 3200 m/s

correspond to the zones of weakness and rupture areas.

Physico-mechanical and elastic parameters typical for the Balapan massif rocks are presented in Table 2.5.

At the Balapan test area it was realized about 100 nuclear explosions in wells, and 7 explosions in wells under the program of peaceful use of nuclear explosions (within a period 1965-1968) with the aim to optimize the parameters of the loading of the charge with excavating action for crater formation (including a salvo shot of three row explosions to produce a trench).

Table 2.5. Phisico-mechanical properties of the Balapan rock system.

Rock type	Density, kg/m^3	Porosity, %	Water content, %	Strength to the one-axis compression, MPa		Velocity, m/s		Young's modulus, GPa	Poisson's ratio
				in the dry state	in the water saturated state	P-wave	S-wave		
Tuff	2760	1.9	0.11	96	113	5600	3250	71	0.25
Tuffstone	2740	1.4	0.25	71	68	5540	3330	71	0.25
Tuffaleurolite	2720	2.2	0.10	98	84	5690	3380	78	0.26
Slate	2720	0.7	0.24	86	49	5580	3020	65	0.39
Sandstone	2740	0.8	0.27	80	54	5530	3000	65	0.29
Porphyrite	2700	2.2	0.20	96	104	4900	3200	70	0.29
Metasomatite	2740	0.9	0.20	64	38	4990	2820	56	0.26
Granite	2660	1.1	0.28	96	106	5560	3220	68	0.23
Granite-porphyry	2630	1.5	0.17	94	88	5100	-	-	-
Granodiorite	2660	2.3	-	-	-	4600	2850	53	0.18
Basaltic porphyrite	2760	3.5	0.35	-	66	4800	2970	57	0.24

3. MECHANICAL EFFECTS OF THE LARGE-SCALE CHEMICAL EXPLOSION, CARRIED OUT IN JUNE 27, 1985

3.1 Geological conditions of the explosion realization

The large-scale experiment with the demolition of 500 tones of chemical explosives was realized in June 27, 1985 at the one of the test areas in the Degelen rock massif.

The experimental explosion was realized on the low mountain (Fig. 3.1). The top of the mountain has an oval form with a latitudinal extension, its slopes are asummetrical, the northern slope is more steep (30-40°) and dismembered. The depth of the errosive V-form cuts reachs 10-15 meters. The southern slope is gentle (15-20°) and less dismembered by errosive cuts with a gentle sides and a low depth (about 5 meters).

The top of the mountain is covered with a low-powered stratum of the Quaternary (Q) eluvial-deluvial sediments (crudefragmental rocks with sandy-loam filler), its slopes are covered with deluvial-proluvial sediments (crude-fragmental rocks, detritus with a loamy filler), their thickness reaches 5 meters in the gutter gullies, the territory uncovering is bad.

The rock massif consists of the volcanogenious formations (diabasical porphyrite, liparity-porphyry) of the Lower Carboniferous age (C_1V_3-n) disbanded by the intrusion of the quartz syenits conditionally dated the Lower Carboniferous age too ($\mu\xi C_1V_3$-n ?) and by granitoid formations ($\gamma\pi_2 PZ_3$ III). The rock contact passes on the top part of the moutain and gently falls to the south-west. The nearest to the top dislocation of the quartz syenits are observed at the southern slope, in this area the distance from the contact to the explosion centre is equal to 80 meters. The central part of the object is composed by porphyrites. The contact of the syenits and diabasical porphyrites is obtained from the data of the magnito- and seismoexplorations. In the magnetic field the contact is detected by anomalies in ΔT (58200/57300 nTl). Furthermore, there is the difference of the T dispersion in the porphyrites field (σ/D = 470-825 nTl) and quartz syenits field (σ/D = 163 nTl). The direction of the contact insidence is defined from the data of the magnitoexploration.

Effusive rocks are massive, the structure is porphyritic, the great mass of the diabasical porphyrites consists of the plagioclase microlits, peached glass, and, in the porphyritic disseminations, pelited feldspar. The main mass of the liparity-porphyries consists of the small crystals of the feldspar, quartz, and biotite. Porphyritic dissiminations are represented by melted quartz and pelited potassium feldspar. Eroded

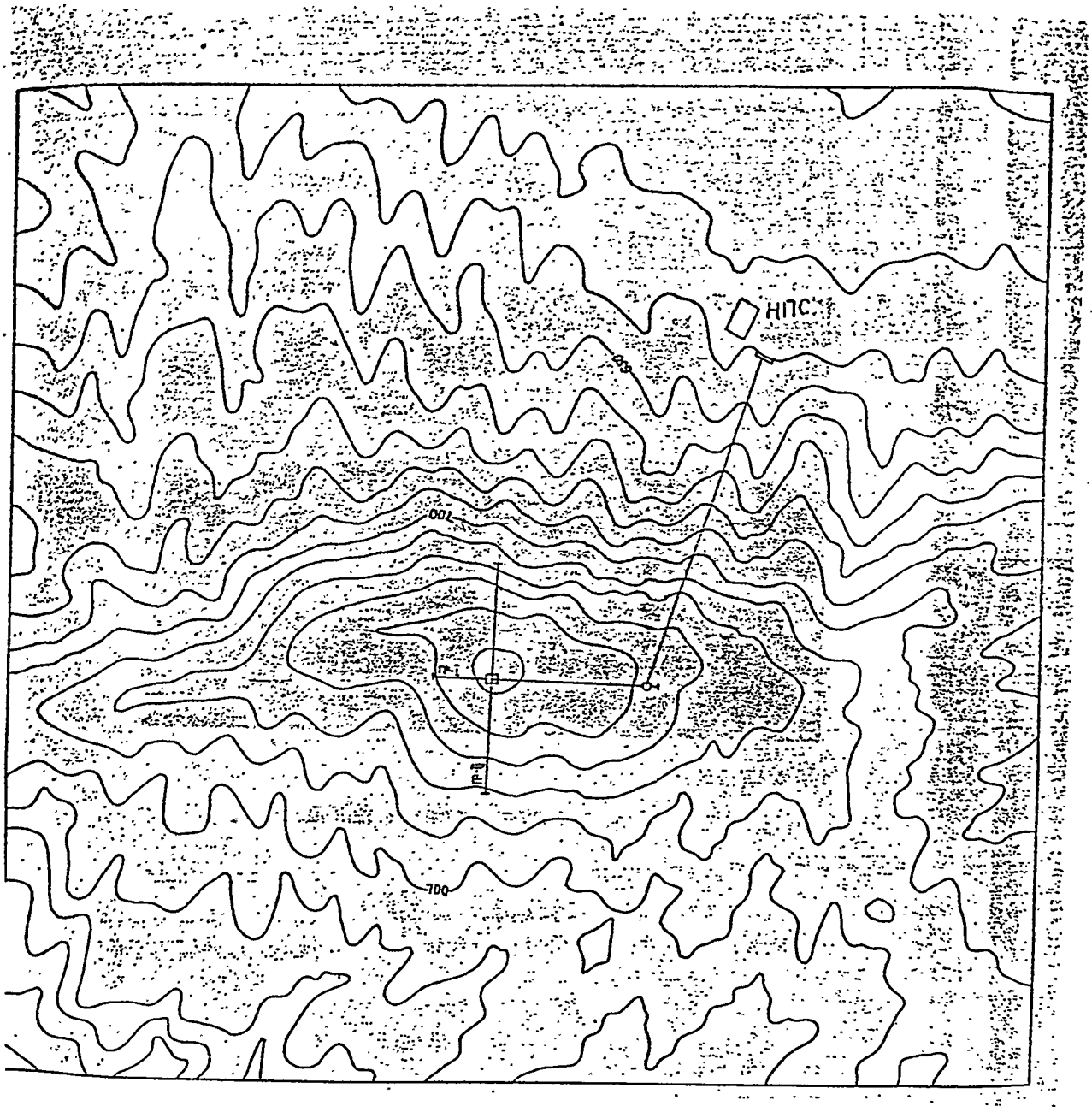

Figure 3.1. Topographical scheme of the object location, scale 1:25000

porphyrites (the crack void coefficient is K_{cv} = 2.7%) are solid (the temporal resistance to the one-axis compression is R_c^w = 86 MPa), weakly deformable (P-wave velocity is V_p = 5.39 km/s, Young's modulus - 0.62), with a great number of cracks (crackness module is $M_{cr} \sim 11$).

Here and futher in text, we use average statistical characteristics of the physico-mechanical properties of the rocks, in which three practically orthogonal systems of the cracks (337° ∠ 78°; 62° ∠ 68°; 244° ∠ 30°) have a primary development, and, in whole, the cracks form chaotic continuous net. The zone of the eroded diabasical porphyrites is expressed by a high degree of the rock crackness and has two-layered structure: up to 9-12 m the rocks have the highest crackness (boulder zone), and further, up to 15-45 m crackness of the rocks is high, the cracks net is interrupted.

The elementary block has an irregular form, its sizes vary, in average, from 0.045 to 0.220 m^3, depending on the rock crackness. P-waves velosity (V_p) in the boulder zone is equal to 1.0-1.6 km/s. Increasing of the hypergenesis zone thickness up to 8-12 m usually is connected with zones of the influence of tectonic disturbances. The minimum thickness (3-6 m) is connected with the areas of the eluvial-deluvial sediments development. In the high-crackness zone the velocities are equal to 1.8-3.2 km/s. The thickness of the whole weathering zone is equal to 15-45 m. At the eminence crest the thickness, in general, is equal to 25-35 m, but at the part of the dike intrusion and in zones of the tectonic disturbances influence it increases up to 45 m, and at the watershead areas it is equal to 15-25 m.

Noneroded rocks (middle crackness) are solid, the cracks net in it is interrupted. Practically, the weathering hasn't an influence on the strength characteristics of the rock sample. Noneroded porphyrites are characterized by follow values of the physico-mechanical characteristics: R_c^w= 104 MPa; V_p= 5.03 km/s; M_{cr} = 5-6; K_{cv} = 0.4%. P-wave velocities in massif vary within the limits of 4.5-6.4 km/s.

Intrusive formations - quartz syenits - are massive and completely decrystallized and consist of the potassium feldspar (75-80%), plagioclase (3-5%), quartz (5-10%), biotite and hornblende (3-5%). There are apatite, zircon, rutile, ore minerals, leucoxen, sphene and garnet in the accessory minerals. Eroded quartz syenits (K_{cv} = 3.86%) are solid (R_c^w = 65 MPa); highly deformable (V_p = 3.46 km/s), with a mean number of cracks (M_{cr} = 9). Interrelation of the basic cracks systems (the next three orthogonal systems: 350° ∠ 80°; 62° ∠ 60°; 248° ∠ 30° have a primary development) shows that the intrussive formations have, in general, petrogenetic crackness. In whole, the cracks

net is regular and continuous, the elementaru block is a parallelepiped with average size 0.078 m^3. Rocks profile was studied up to 200 m in depth (by the well N°4017). From the profile shooting we know that the rocks are under the influence of weathering up to 20-45 m in depth.

The weathering zone is two-layered. The thickness of the upper layer (boulder zone) is about 2-12 m, and the velocity in this layer is equal to 1.0-1.4 km/s. In the highly cracked zone (the lower layer) the velocities are 1.8-3.0 km/s, and in the safe syenits these velocities usually are equal to 4.4-6.0 km/s.

At the surface, the quartz syenits are destroied to the rotten stones and detritus.

The vein complex is represented by the bodies of quartz porphyries and basalts ($\gamma\pi_2 PZ_3 III$) geneticaly connected with the intrusive complex of the Upper Palaeozoic age (γPZ_3). Half-edge cracks of two directions (M_{cr} = 19.4; K_{cv} = 8.54%) predominate in aplits. The complex rocks are revealed by the well N°4015 at the depth of 43.5-52 m. At this depth the aplits are middle cracked, and the cracks, usually, are narrow, hairbreath and half-edge.

Quartz porphyries ($\gamma\pi_2 PZ_3 III$) are revealed at the depth 21.3-22.8 m by the well N°4014, the rocks are broken by half-edge narrow cracks. The host rocks are highly cracked near the contact zone.

From the structural-tectonic viewpoint the rock massif is a system of the structural-tectonic blocks of the fifth order (STB-V), with form and size determined by small tectonic faults and large cracks. Usually, STB-V have a form of oblique irregular paralelipiped with the probable volume about 100000 m^3.

A number of the structural boundaries were revealed by rock excavation. It is a complex of half-edge straight or slightly curved small ruptures (cracks) with solid, relatively flat sides. The thickness of the cracks displacement zone varies from 0.5 to 15 cm, more often it is about several centimeters. Broken quartz-carbonate material, iron hydroxyle and clay gouge were found as a filler. There are gentle cracks with branching, curved, more thick (in average, the thickness is equal to 5 cm) crack displacement zone and hilly sides.

Hydrogeological conditions of the object are characterized by the absence of any natural displays of the underground waters at the surface. The underground waters are revealed by the wells N°4013, 4015, and 4017 at the object area, as well as at the nearest territory. So, it is expediently to show the hydrogeological conditions not only at the object area, but also

at the whole territory, presented at the hydrogeological scheme (Fig. 3.2).

At this territory the undeground waters of the crack-soil type are developed in zone of the exogenous crackness of the effusive (C_1V_3-n) and intrusive ($\mu\varepsilon C_1V$-n ?, γPZ_3) rocks. It is a common future, that the waters are located in valleys, they wedge out to the mountains and are observed only in the lower parts of the slopes. The water stream moves down the valley. The stream slope is similar to the valley slope, and only in the upper parts the surface of the valley have a slope, which is greater than the underground water slope.

The low boundary of the underground water spreading is defined by the attenuation of the rock crackness, usually, at the depth of about 40-45 m on the slopes and at the 50-55 m in depth on the bottom of the wide valleys. So, the high-rock areas are under conditions of the full drainage. There are two disconnected streams of the underground water at this territory.

The larger stream are placed to the east and to the north from the object, with the general north-western direction of the water motion. The smaller stream begins at the southern part of the object (the well N°4017) and are oriented to the south-west. Two streams are divided by the drainage area. At the region limits the underground waters in effusive and intrusive rocks create the common water-bearing level.

The level of the underground waters decreases down the valley, at the north-east its average slope is equal to 6% and with the valley expansion to the north from the object the slope decreases to 1%.

The depth to the water at slopes and upper reaches of the valley is the greatest and equal to 14-39 m. In the middle part of the valley the depth is 2.9-7.5 m. The underground waters are nonheaded, and only to the north from the object they gain some head because of the overlaping the rocks by the clay of the Neogenic age (the well N°320). The information about the level variations is presented in Table 3.1.

The velocity of the natural variation of the water level in the wells in spring-summer period reaches 0.25 m/day (the well N°4013) and even 0.4 m/day (the well N°4017).

The degree of the water abundance is low and characterized by the specific outputs usually varied from 0.006 l/s to 0.152 l/s for wells in the effusive rocks and from 0.11 l/s to 0.25 l/s for wells in the intrusive rocks.

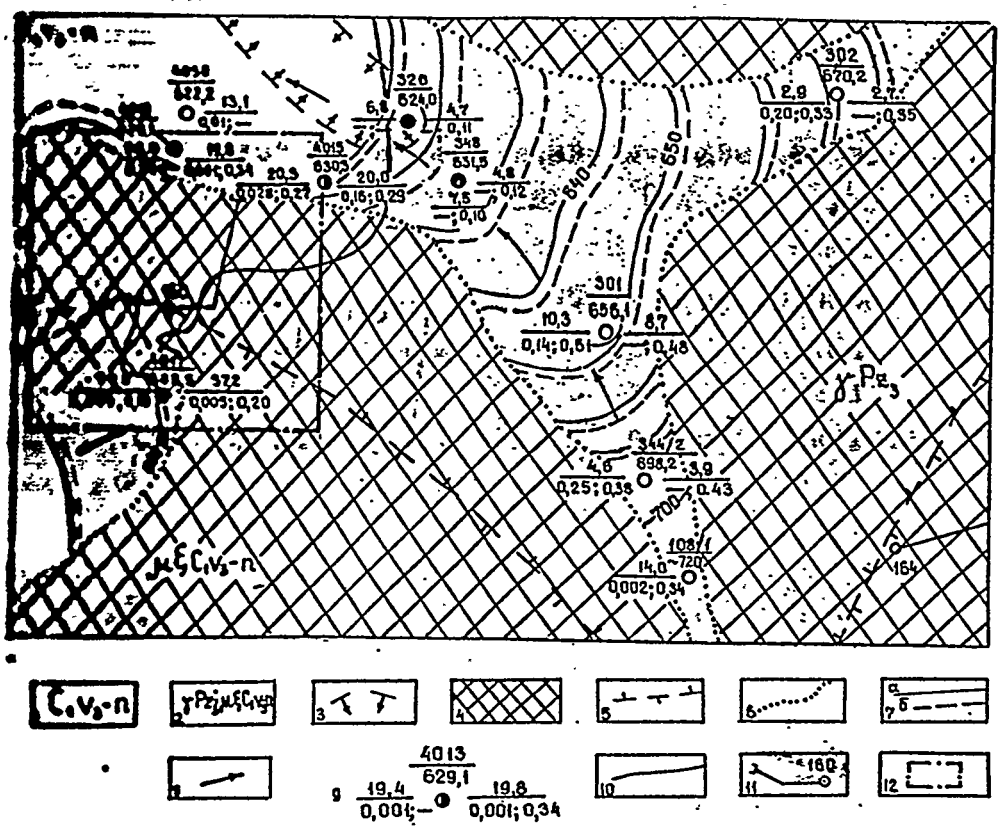

Figure 3.2. Schematic hydrogeological map, scale 1:25000

1 - underground waters in the effusive formations of the lower Carboniferous age (verhnevizeisky-namyursky layer) - liparite porphyries, rarely;
2 - underground waters in the intrusive rocks of the Upper Paleozonic age - granites (γP_{z3}) and quartz syenites ($\mu\xi C_1 V_{3-n}$) in the south-west part;
3 - waterproof Neogene shales (berghachures points the direction of the shales spreading);
4 - watershead area;
5 - watershead line
6 - boundary of the spreading of rocks, supplied by water, and draining rocks;
7 - hydroisogypsums: a) in 1984, b) in 1987;
8 - main direction of the underground water motion
9 - well characteristics: overhead - well number is represented at the numerator, and absolute level of the outfall (m) is at the denominator; left and right marks represent the the state in 1984 and 1987, correspondingly, and give the next characteristics: underground water level (m) at the numerator and specific yield (l/sec) at the denominator; the circle color shows type of the predominant anion: black - hydrocarbonates, white - sulphates;
10 - stratigraphical boundary;
11 - gallery line and its number;
12 - investigated areas;

Comment: Hydroisogypsums are ploted according to the average annual values of the underground water level.

Table 3.1. Annual amplitudes of the underground water levels

Regime	Well number	1984	1985	1986	1987
flat	4013	1.7	1.1	0.7	0.9
flat	4015	1.5	1.0	0.4	1.2
foothillen	4017	-	3.4	1.1	8.7
foothillen	301	1.1	4.2	2.1	5.1
foothillen	302	2.2	1.2	1.6	3.7

The total water mineralization is equal to 0.15-0.57 g/l, and, as a rule, it is smaller in the wells, located in upper reaches of the valleys. Among the anions the hydrocarbonates have a predominant development (up to 67% mg-eqv) and, rarely, the sulphates are predominant there. Among the cations, in the most cases, the alkaline metals and sometimes the calcium are predominant. The water is moderately hard, and the reaction is weakly alkaline.

Within an year, the total mineralization varies slightly from 0.06 to 0.33 g/l, and it is less in the upper reaches of the valleys and at the slopes.

From the results of the studing of the underground water regime two types of them - flat and foothillen - might be destinguished. The first regime type is characterized by slight seasonal variations from 0.4 to 1.7 m (the wells N°4013, 4015), but the second - by the largest variations from 1.1 to 11 m because of the nearness of the watershead (see Table 3.2). During the dry 1966 year the level variations for flat and foothillen types were equal to 0.4-0.7 m and 1.1-2.1 m correspondingly. The last year is characterized by the highest amplitude of the variations.

The gallery N°160, by hydrogeological conditions, are located in the foothills zone and its biggest part is located below the boundary of the exogenous crackness, permeable to water, so any water displays in this gallery are absent.

3.2 Conditions of the experiment

In the experiment N°1 the explosive charge was located at the top of the low mountain (Fig. 3.3) with the absolute levels from 620 m (the mountain foot) to 753 m (the mountain top).

Before the first explosion a horizontal platform was

Table 3.2

Well number	Year	Underground water level				Annual amplitude of the level oscillations, m	Average annual depth of the water level, m
		depth, m		month			
		max	min	max	min		
4013	1984	21.17	19.05	april	september	2.12	19.95
	1985	20.50	18.85	april	may	1.75	19.80
	1986	20.20	19.45	april	february	0.65	19.88
	1987	20.35	18.90	april	june	1.45	19.82
4015	1984	21.33	19.61	april-june	september	1.72	20.31
	1985	20.65	19.60	april	june	1.05	20.03
	1986	20.35	19.60	april	june	0.75	20.00
	1987	20.50	19.20	may	june	1.30	20.05
301	1984	17.70	6.60	the end of march	november	11.1	10.26
	1985	11.20	5.65	the beginning of april	the end of may	5.55	8.23
	1986	9.60	6.23	april	june	3.37	7.82
	1987	10.75	5.29	april	may	5.46	8.69
344	1984	8.87	2.54	april	september	6.33	4.62
	1985	-	-	-	-	-	-
	1986	-	-	-	-	-	-
	1987	6.15	1.70	january	june	4.45	3.92
320	1984	3.95	1.38	april	september	2.57	2.93
	1985	4.30	1.70	january-april	april	2.60	2.52
	1986	4.10	2.35	march	june	1.75	3.55
	1987	4.20	0.20	february	may	4.00	2.70
4017	1984	-	-	-	-	-	-
	1985	40.00	35.05	december	may	4.95	38.76
	1986	40.45	38.80	april	june-july	1.65	39.80
	1987	40.45	30.50	february	may	9.95	37.45

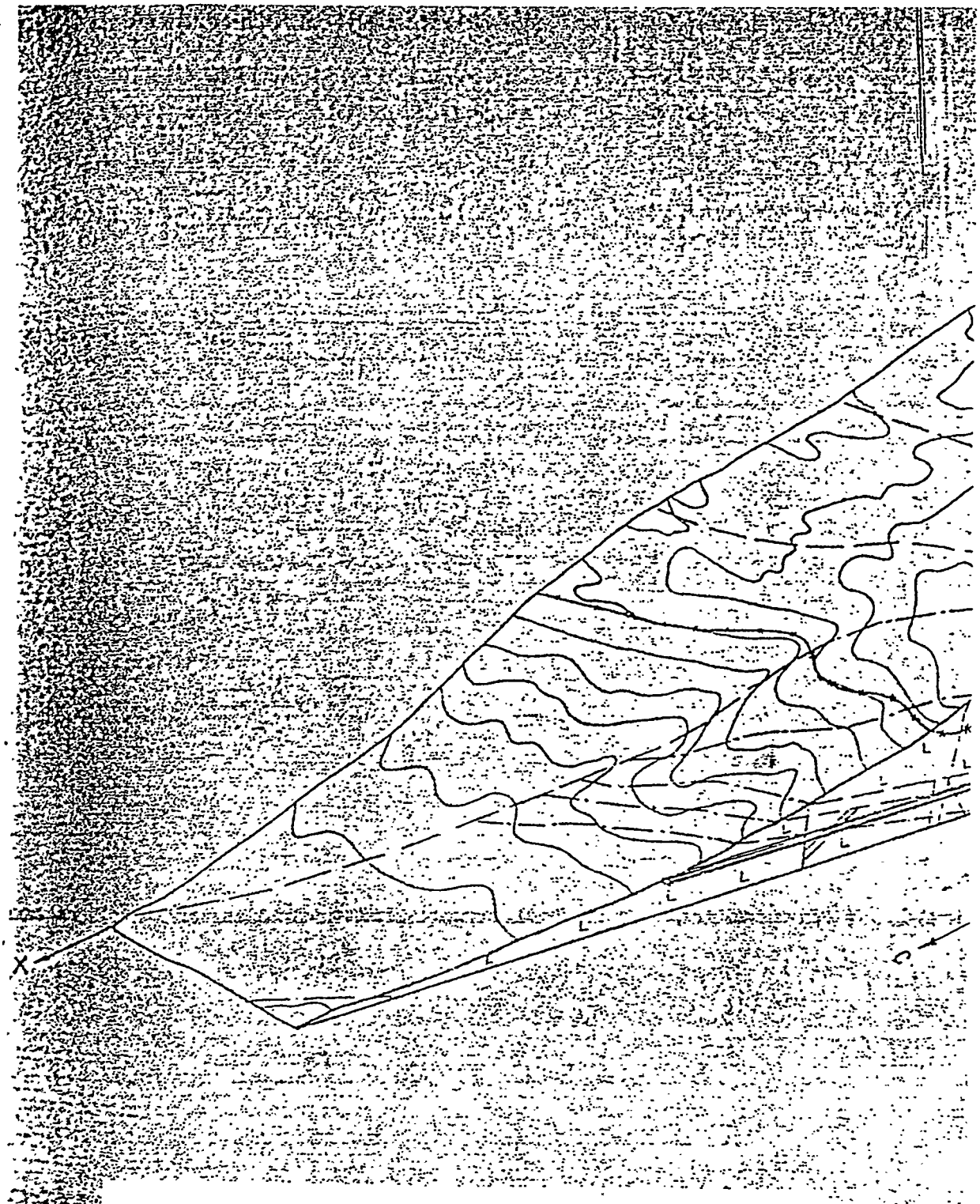

Figure 3.3. Isometrical scheme of the experiment
Conventional signs:

- Volcanogenic complex. Carboniferous system, Lower part, Vizey-namyur layer (non-broken) 1 - liparite porphyries; 2 - diabasic porphyrites
- Complex of the subvolcanic small intrusious of quartz syenites.

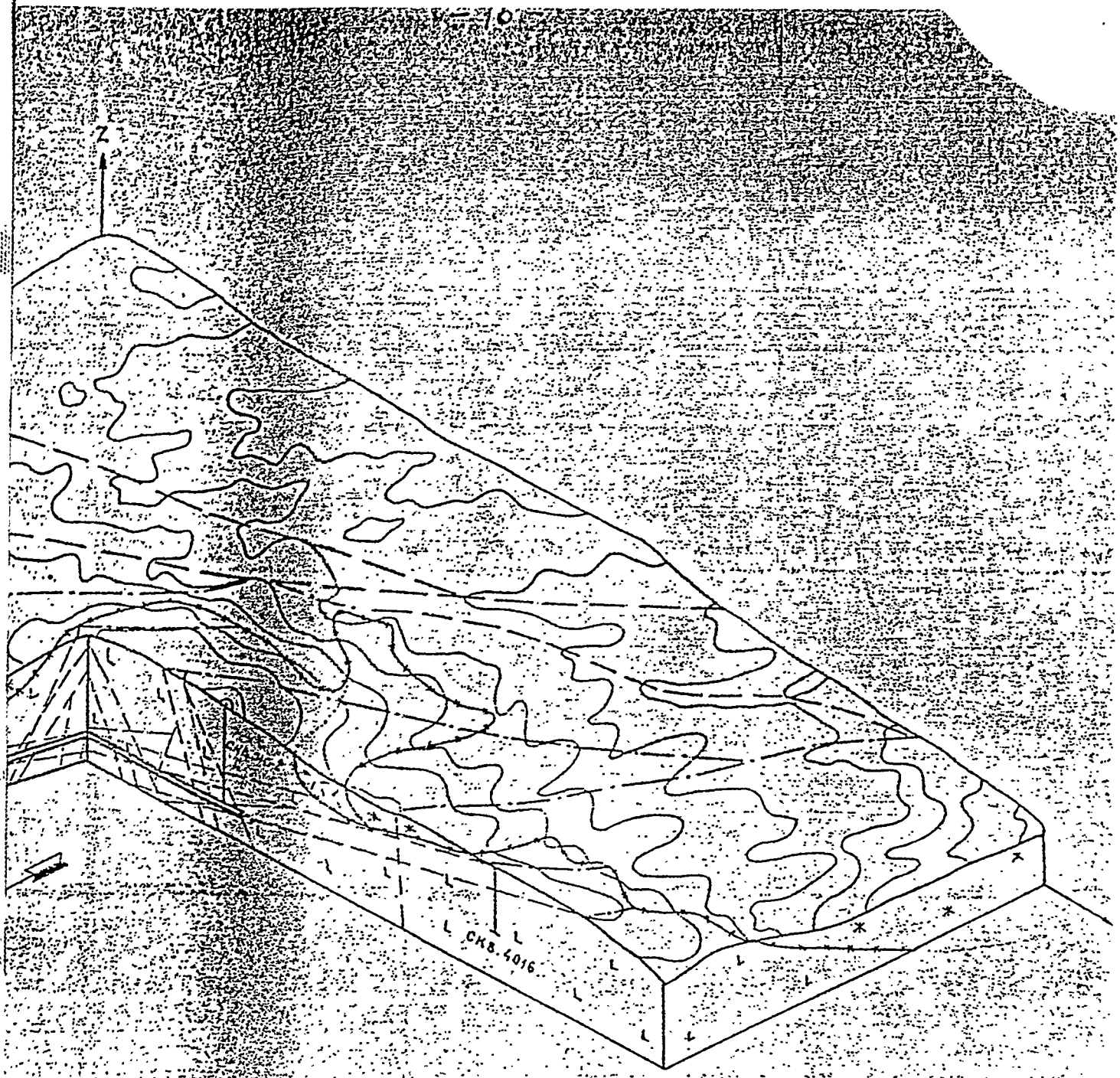

Tectonic cracks:
- covered by mellow formations
- represented in the relief

Stratigraphical boundary

- Assumed boundary of the lithologic subdivisious of the same age

СК8.4016 - Well and its n

⊙ - Explosion centr

created at the upper part of the mountain, with smoothing by a mellow soil, for a disposition of the boring equipment and the charge, so the absolute level of the top was changed from 752.9 to 751 m. The research gallery passed at the depth of 108-112 m bellow the charge. The modern area relief was formed under the influence of the weathering and gravitation processes. The mountain top has an oval form with a latitudinal extention and is covered by a thin layer of the eluvial-deluvial sediments (crude-fragmental rocks with a sandy-loam filler) with thickness of 0.2-2.0 m. The slopes are covered by a deluvial-proluvial sediments (crude-fragmental rocks with a loamy filler) and its thickness in the gutter gullies reaches 5 m.

The rock massif is created from the volcagenious formations (diabasical porphyrites, liparity-porphyries) breaked by the intrusion of the quartz syenits. The contact between these complexes passes on the upper part of the mountain (Fig. 3.3) and gently falls to the south-west. From the structural-tectonic viewpoint, the massif is the system of the structural tectonic blocks (STB) boundared by a tectonic ruptures (Fig. 3.4). Elements of the rupture bedding vary in wide limits, its supposed length is equal to 120-600 m and its thickness varies from 0.5 to 10 cm.

The gentle cracks are branching and curved, their surface are rough and hilly. The half-edge cracks, usually, are straight with a flat surfaces. The cracks are filled by a tectonic breccia, quartz-carbonate aggregate, clay gouge and iron hydroxiles.

The upper part of the massif is under the influence of the weathering processes. The main feature of the weathering zone is its two-layered structure and nonuniform rock solidity. The thickness of the upper part of the weathering zone (boulder zone) varies from 3 to 12 meters (5-6 meters in the explosion epicenter); the thickness of all eroded zone (boulder zone and zone of high rock crackness) is equal to 15-45 meters (Fig.3.4, 3.5).

From the profile shooting and preliminary treatment of the seismic prospecting, these zones are characterized by the follow P-vawe velocities:

in the boulder zone - 1.0-1.6 km/s;
in the zone of the high rock crackness - 2.0-3.0 km/s;
in the noneroded part of the massif - 4.4-6.0 km/s.

Abnormally low velocities in the noneroded part of the massif (3-3.5 km/s) are connected with zones of the tectonic rupture development.

The massif rocks have predominantly petrogenetic crackness

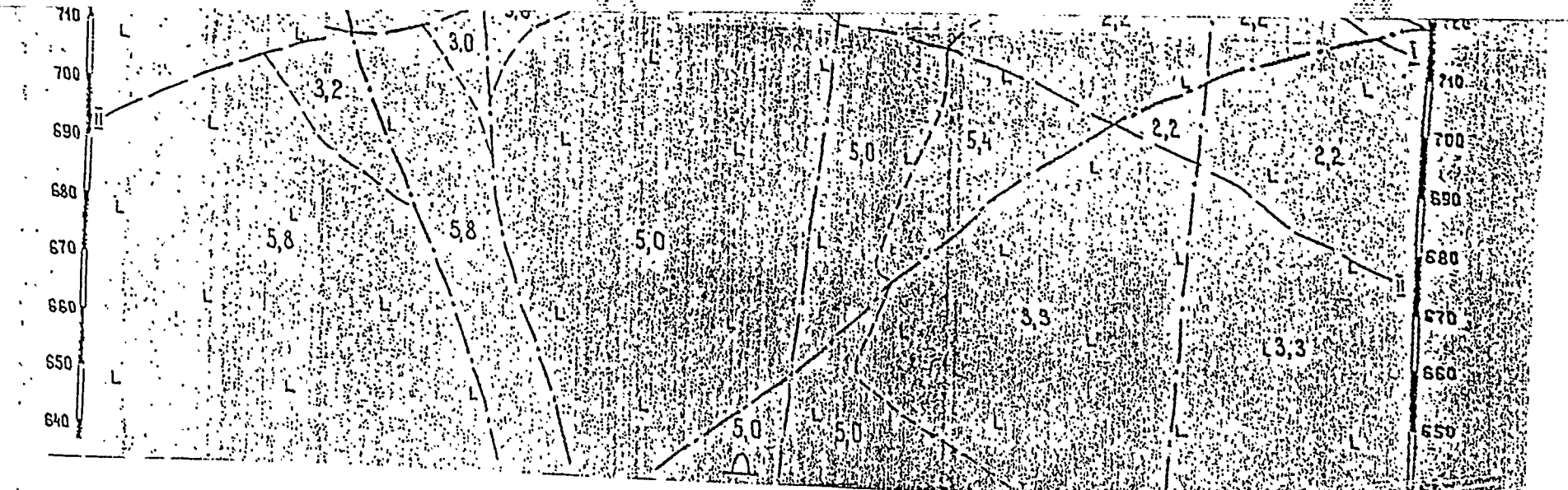

Figure 3.4. Geological and geophysical cross-section.
Scale 1:1000

У С Л О В Н Ы Е О Б О З Н А Ч Е Н И Я

- diabasic porphyrites
- quartz syenites
- rock excavation
- tectonic cracks
- boundaries of the areas with different velocity characteristic
- values of *P*-wave velocity, km/s
- refracting boundary and its number

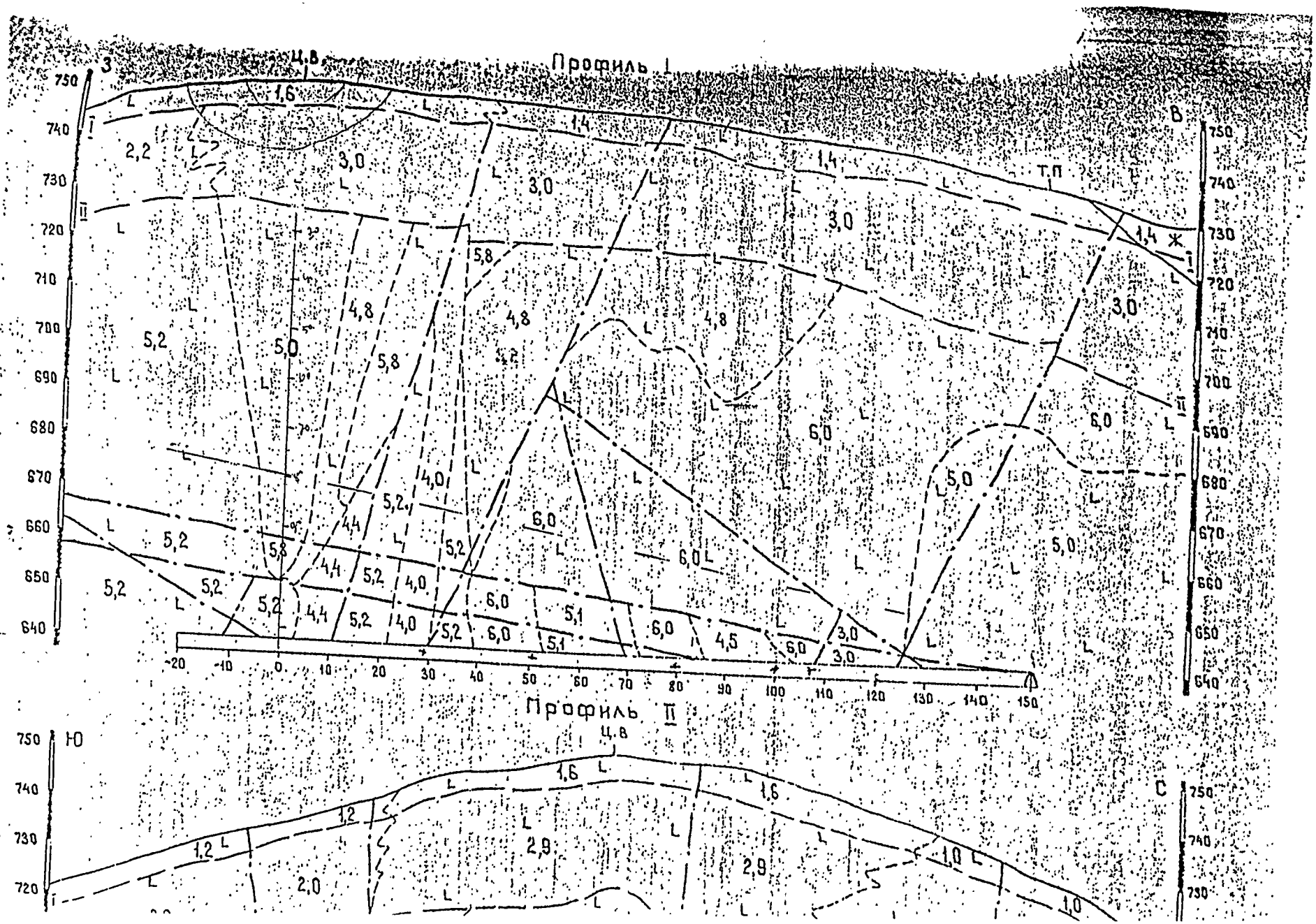
Профиль I
Ц.в
З
В
Т.П
Ж
Профиль II
Ц.в
Ю
С

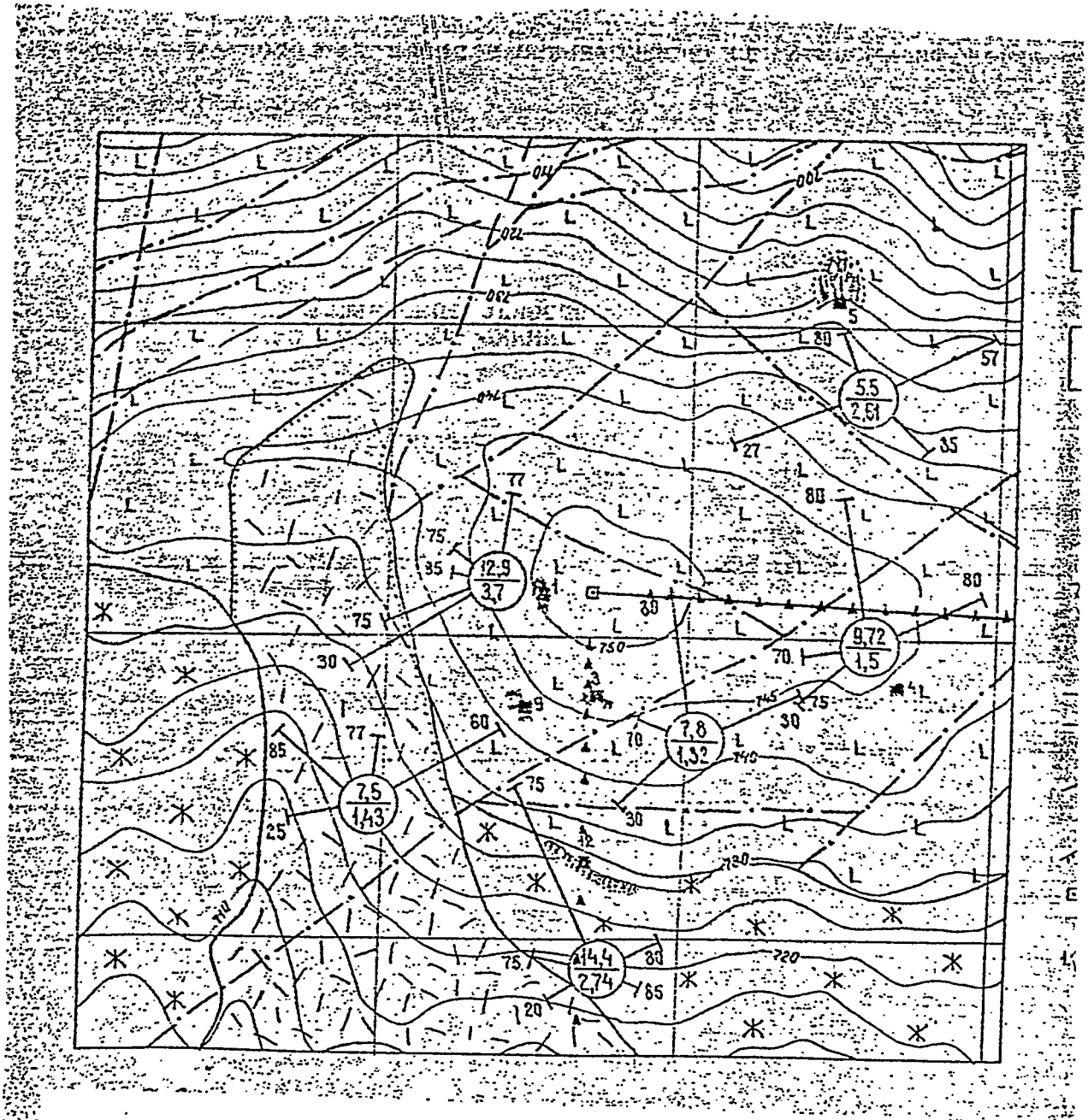

Figure 3.5. Schematic engeneering and geological map, Scale 1:2000

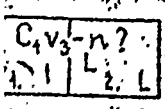

- Carboniferous system, Lower part, Vizey-namyur layer (non-broken).

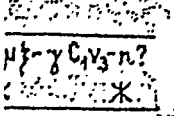

- Complex of the subvolcagenic intrusion. Subvolcanic small intrusions of quartz syenites.

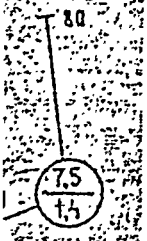

- Diagram of the rocks fissuring
  Vector direction corresponds to the azimuth of the cracks system in percents from total crack number (2% cracks per 1 mm); figure near the vector - to the angle of incidence; figures in the circles represent the next characteristics: numerator - total value of the fissuring modulus, and denominator - total value of the crack porosity of the crack net.
- Tectonic cracks:
  - covered by mellow formations
  - represented in the relief
- Stratigraphical boundary
- Assumed boundary of the lithologic subdivisions of the same age
- Well projection
- Solid rocks outcrops, points of the observations:
  1 - covered by pile, partially or full broken
  2 - non-changed
- Points of the survey of ejecta deposits

complicated by the exogenous crackness in the hypergenesis zone.

There are chaotic interrupted net of the cracks in the diabasical porphyrites. In the block zones and zones of the high crackness the net of the cracks are continuous and broken. The crack net defines the bouldered form of the elementary blocks and their sizes: in the hypergenesis zone the volume of the elementary blocks is equal to 0.045 m^3 and in the noneroded rocks it is equal to 0.220 m^3. The crack thickness varies from 0 to 2.0 cm at the surface and from 0.05 to 0.2 cm in the gallery.

From the detailed treatment of the geological documentation of the rock excavation, which give a more reliable understanding of the value and limits of the linear sizes of the individual blocks, it is possible to see that at the separate parts the block structure of the massif is not the same, i.e. the average block size varies in wide limits (up to 2 times). So, the calculated mean block size for the piquet intervals 20÷30; 30÷150; 150÷220 is equal to 12, 24 and 16 m correspodingly.

These calculations can't be highly exact because of the differences in the elements of the bedding of the tectonic rupture intersecting the gallery; but these calculations give a qualitative estimations of the different block sizes in this intervals. It is naturally to suppose that the differences in the block sizes around the rock excavation can influence on the rock disturbance near the excavation and into it after the explosion.

The follow data represent the physico-mechanical characteristics of the rocks in the noneroded part of the massif:

density, g/cm^3	2.88
density of the mineral part, g/cm^3	2.89
porosity, %	0.74
water content	0.26
temporal resistance to the one-axis compression, MPa, in the dry state	105
in the water saturated state	98
P-wave velocity, km/s	5.017
S-wave velocity, km/s	2.69
Young's modulus, 10^5 MPa	0.55

Poisson's ratio 0.29

The underground waters are revealed in zone of the exogenous crackness of the diabasical porphyrites at the absolute levels below 611 m.

In whole, it is necessary to note that the object is located in the solid waterless rock massif.

3.3 Explosive charge construction

For the investigations of the mechanical influence of the explosion on the rock massif, the surface semi-spherical charge with mass of 500 tons was used in the experiment №1. The charge consisted of the main charge with mass of 499520 kg and the intermediate detonator with mass equal to 480 kg. The main charge consisted of the scaly trotyl in the jute bags, each of them with mass of 40 kg, which were laid out level by the level. The intermediate detonator were made of the trotyl pressed into the briquettes with mass of 19.2 kg each.

The charge was located at the area with the radius of 7 m, covered by the ramed layer of the soft soil with 5 cm in thickness. The geometrical form of the charge was the hemisphere with radius of 6.7 m. The scheme of the charge are represented at Fig. 3.6. The factual density of the main charge from the scaly trotyl was equal to 0.79 t/m^3. The variation of the charge radius in the layer was not greater than 0.5 m.

The charge initiation was realized from the centre of its base. The scheme of the charge initiation was composed from two-channel electroexplosive circuit, two fusen firing-pins and two firing-pins of the initiation, connected by lines of the three-threaded detonational fuse. The initiation of the fusen firing-pins was made by two consecuently connected electrodetonators. These detonators responded to the current impulse from undermining system.

The time of the charge detonation was equal to 1.45 ms, the mean velocity of the detonation - 4600 m/s. The investigations of the explosion area and shell-hole showed that the charge worked completely.

The dependence of the trotyl detonation velocity from the charge density shown in Fig. 3.7. The results of the measurements of the charge detonation velocity in the first and second experiments are shown by asterisks.

Let's suppose the rough truth of the polytropic state equation for the products of the trotyl explosion with $n \approx 3$. So

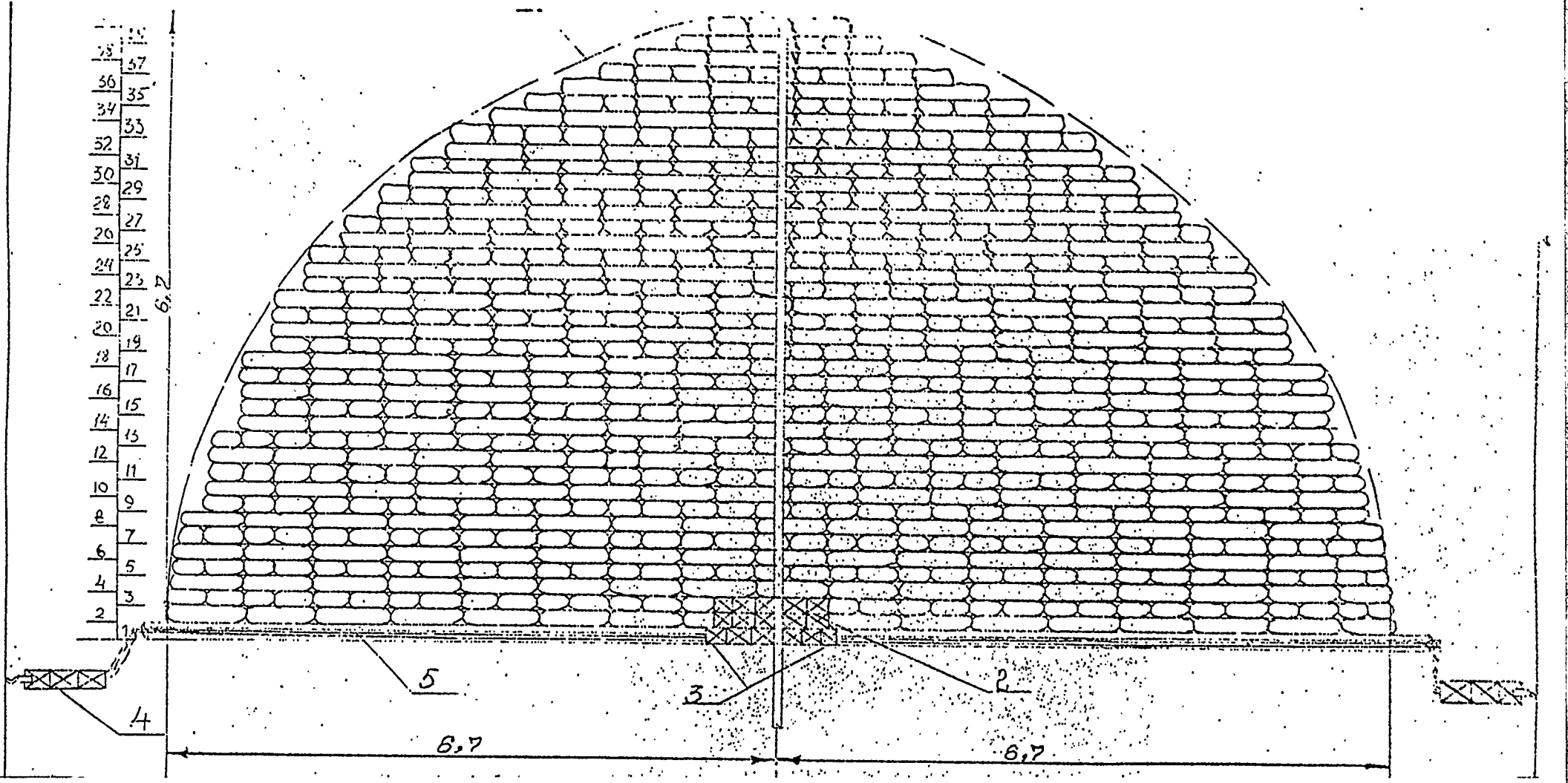

Figure 3.6. Scheme of hemispherical charge.

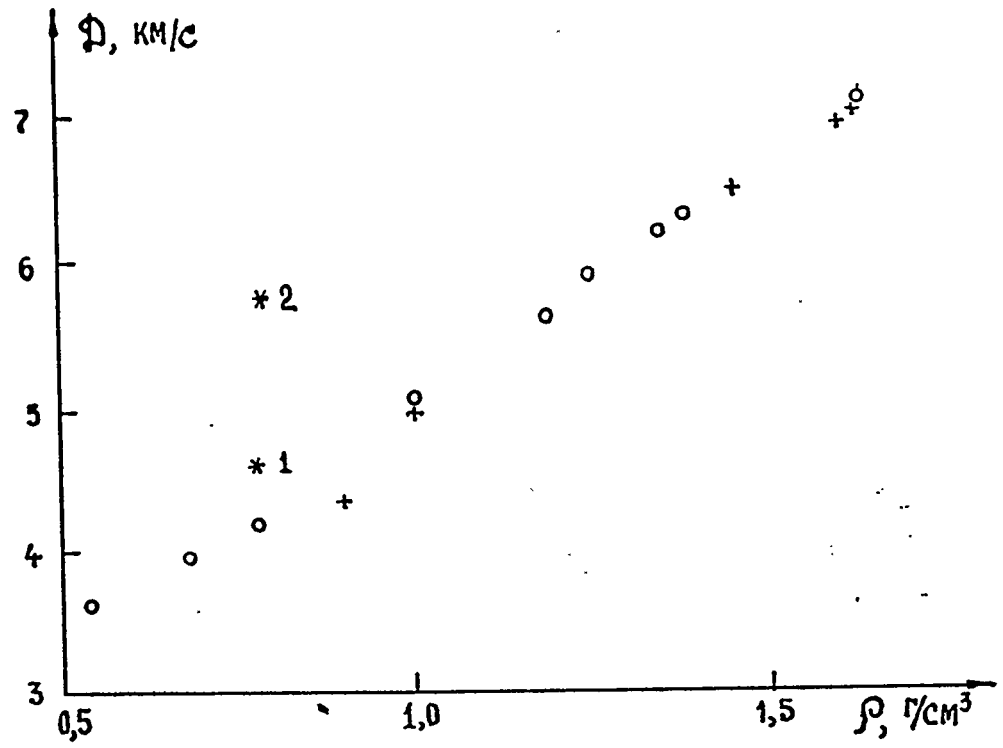

Figure 3.7. The dependence of the trotil detonation velocity from the crarge density.

it's possible to estimate the pressure behind the detonation front as ~ 40 kbar for the detonation velocity of about the 4.5 km/s. Since the detonation spreaded from the base centre, the pressure at the charge-soil surface might be estimated from the well-known solution for the detonation front, which moves on the soil surface. In the experiment "The gallery N°160" the charge was located on the base from the poured material laid on the rocky soil. In the case of the poured soil with density of 2 g/cm^3 and sound velocity of about 0.5 km/s, the estimation of the pressure in the soil connected with the charge base is about 20 kbar with mass velocity in down-directed shock wave of about 600 m/s. The same estimation for the cracked rock with density of 2.7 g/cm^3 and sound velocity of about 1.5 km/s gives the pressure equal to 30 kbar and mass velocity of about 300 m/s.

3.4 Disposition of the measurement equipment in the rock massif

In the experiment, realized in June 27, 1985 the accelerometers EA were located in two wells (I1 and I2) in the niches, maded in the right wall of the gallery. The accelerometers were fastened in the natural hollows in the niches walls by means of the cement solution. Their location is shown at Fig. 3.8 by a black circuls.

The triangles at Fig. 3.8 represent the disposition of the point deformometers DDP. At the level of 20 m the deformometers were located at the surface of the gallery face part, and at the level of 10 m - on the left wall of the gallery. The deformometers were placed in the shallow bore-holes and were fastened by the filling of the melted hyposylphite.

Band and string deformometers were placed on the details cemented into the bore-holes. In the first experiment it was used five band deformographs overlapping the cracks at the levels of 31, 52, 80, 100 and 107 m (Fig. 3.9). The string deformometers were located at the gallery face and at the levels of 80 and 100 m.

To measure the residual slopes the system of the platforms for the optical goniometrical device - Quadrant KO-10 has been placed in the gallery. This system included 15 goniometrical platforms. Ten of them were located in the gallery from the face to the turn (the level 150 m), and five - from the turn to the hermodoor.

The niches of 2 m in depth were created in the left wall of the gallery at the levels of 5 (N1), 15 (N2), and 25 m (N3) by the use of explosives. New measuremental points with electrodynamical accelerometers EA (the niches N1, N2, and N3),

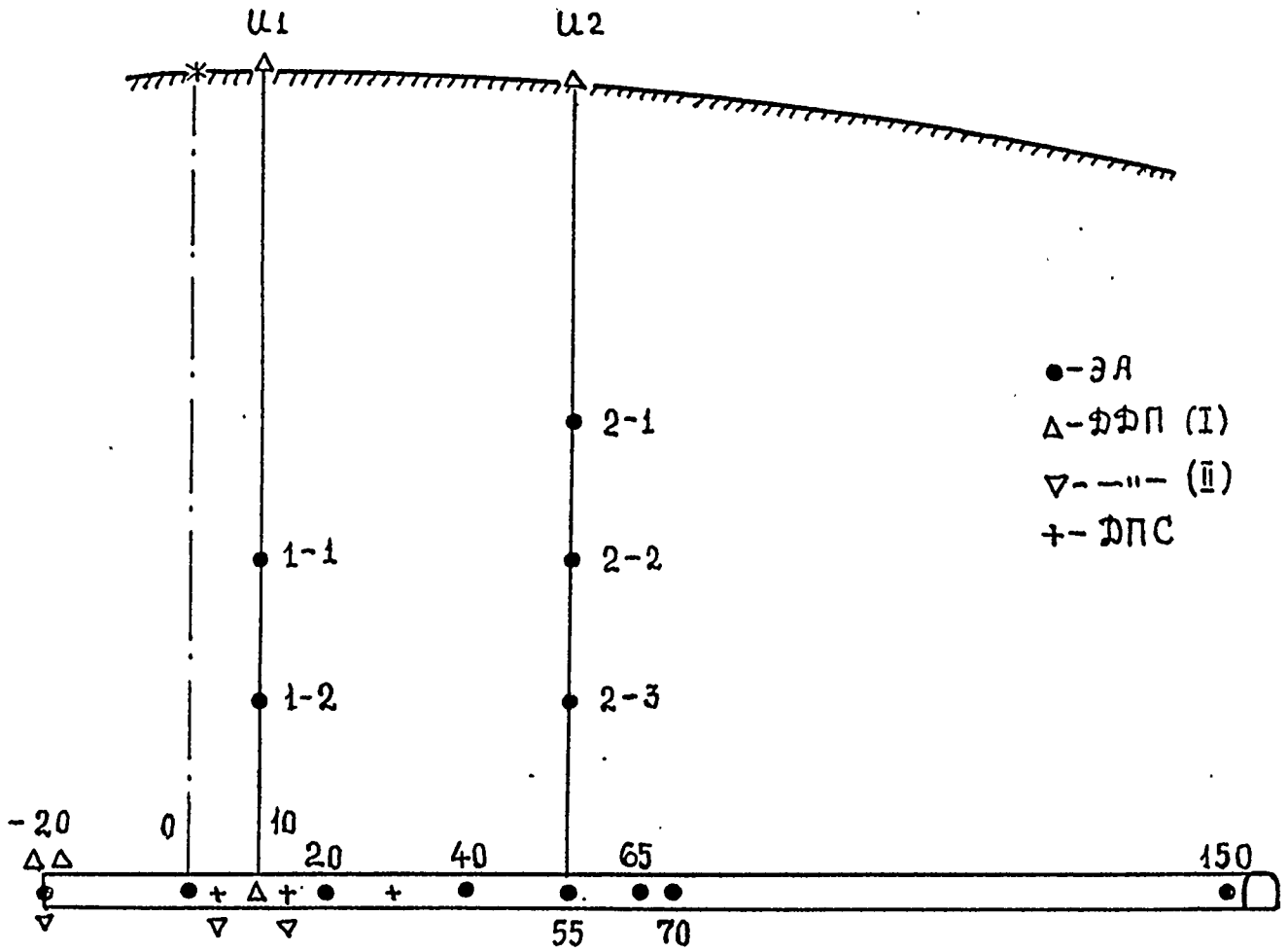

Figure 3.8. Location of the accelerometers EA.

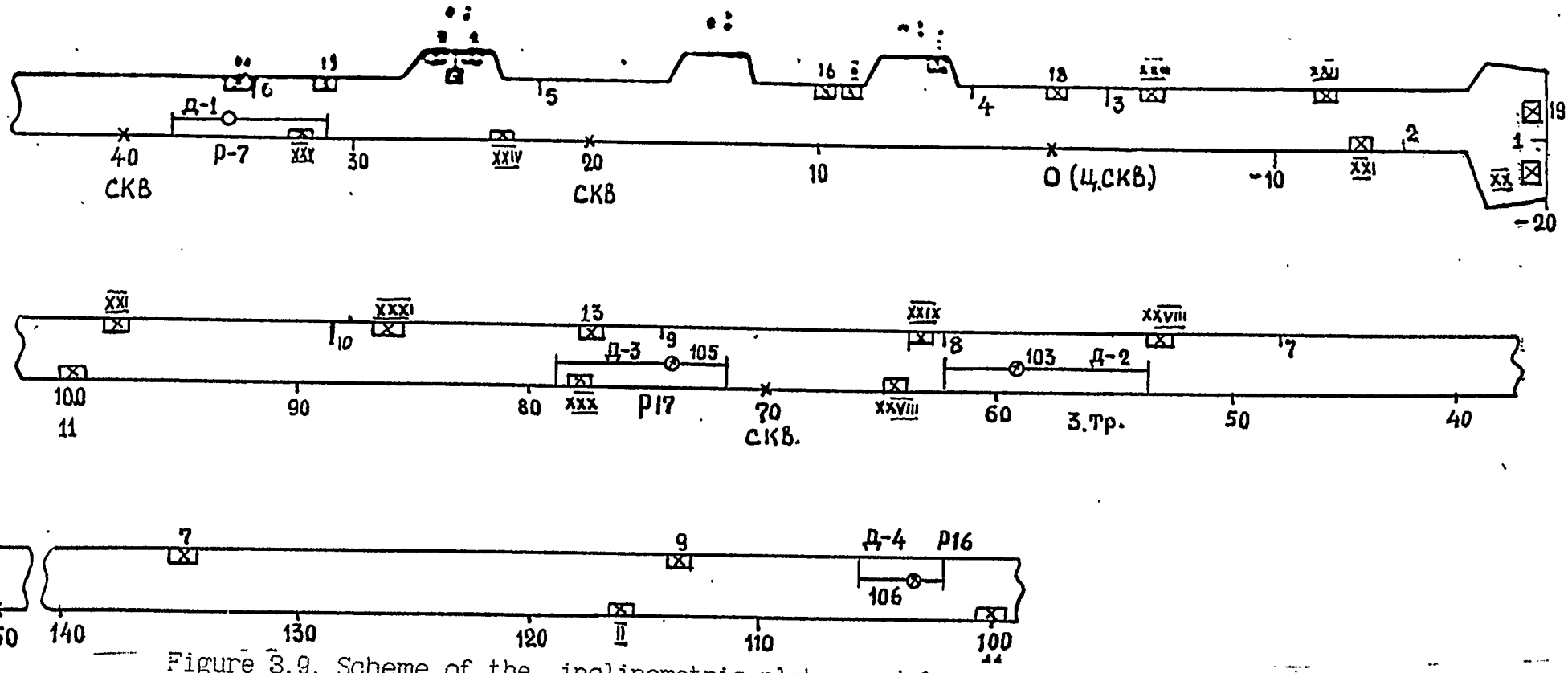

Figure 3.9. Scheme of the inclinometric plates, deformographs and bench-marks disposition.

- inclinometric plate and its number, Niches N1, N2, and N3, created for measurements
- Deformograph and its number
- Bench-mark and its number
- Electrolitic inclinometer IMUS-1
- Distance from the central well, m.

point deformometers DDP (the niches N1 and N2) and the relative displacement detectors RDD (the niches N1, N2, and N3) non-used in the first experiment were located in these niches. In addition, two electrolytic inclinometers IMUS-1 were placed in the niche N3.

To measure the parameters of the seismoexplosive waves the detectors have been placed in the wells, in the pits at the surface of the rock massif and in the gallery. The main measuring profile was located along the mountain ridge in the N1-N5 direction and coincided with the gallery axis passed under the explosion epicentre. The measuring wells were bored from the mountain surface to its intersection with the gallery. The well G1 was bored to 13 m below the gallery level. The scheme of the wells disposition is represented at Fig. 3.10.

The wells G1, G2, G3, G4, G5 and pits N°1-15 were used for the disposition of these detectors. In the gallery the GIS detectors were installed in the niches, roof and soil of the gallery. The scheme of the GIS detectors disposition in the pits of the soil massif surface is shown at Fig. 3.11. Fig. 3.10 gives a disposition of the GIS detectors in the gallery at 10 m away from the intersection of the well G2 and the gallery (A-A cross-section). At the other distances in the gallery the detectors were placed analogously.

In the wells the GIS detectors were installed in the spherical containers. The garland of the containers were prepared in advance and were drew out with a help of the winch from the gallery into the wells.

All cables from the measuring wells were took out into the gallery.

Vertical and horizontal GIS detectors were installed in each container. The orientation of the horizontal detectors to the epicentre was made by three ropes, which were stratched in the wells and passed through the special slotes of the containers, located at an angle of 120° on its circle. At the surface of the mountain and in the gallery at the exit from the well the ropes were fasterned in the preliminary oriented ring. In the well G2 only vertical detectors were installed.

After the detectors installation, the well was cemented by portlandcement M-400. The temperature recorders placed in the wells G3 and G4 showed that the temperature of the solution increased only to +30°C during the period of its induration.

The pits at the mountain surface were holowed out in the rock massif to the depth of 40-50 cm. After installation and orientation of the detectors the pits were filled by the

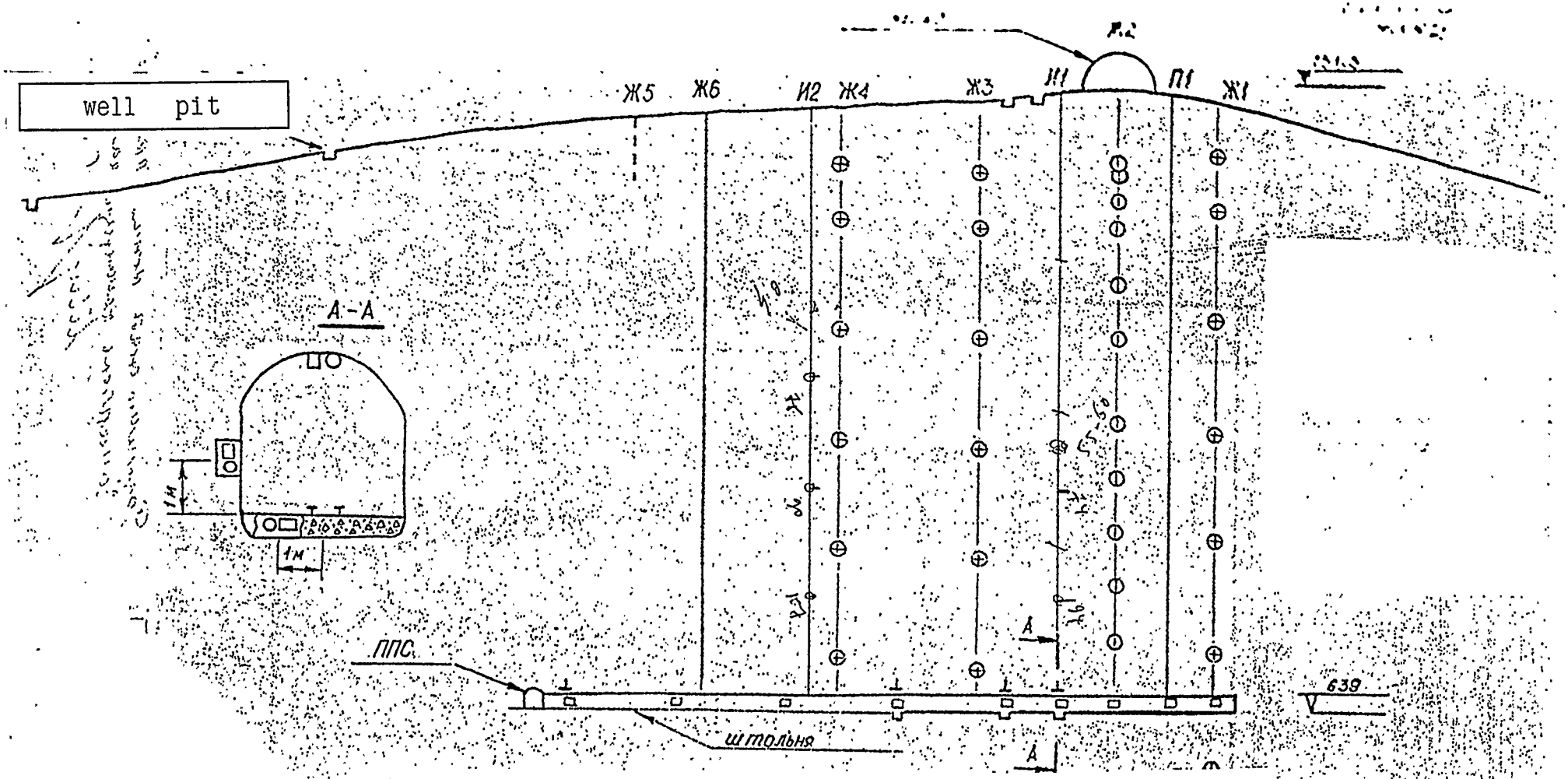

Figure 3.10. Wells disposition; Scale 1:1000;
⊖ - vertical GIS detector
⊕ - vertical and horizontal GIS detector
⊥ - container, installed in the roof
□ - container, installed in the niche
⌐ - pit

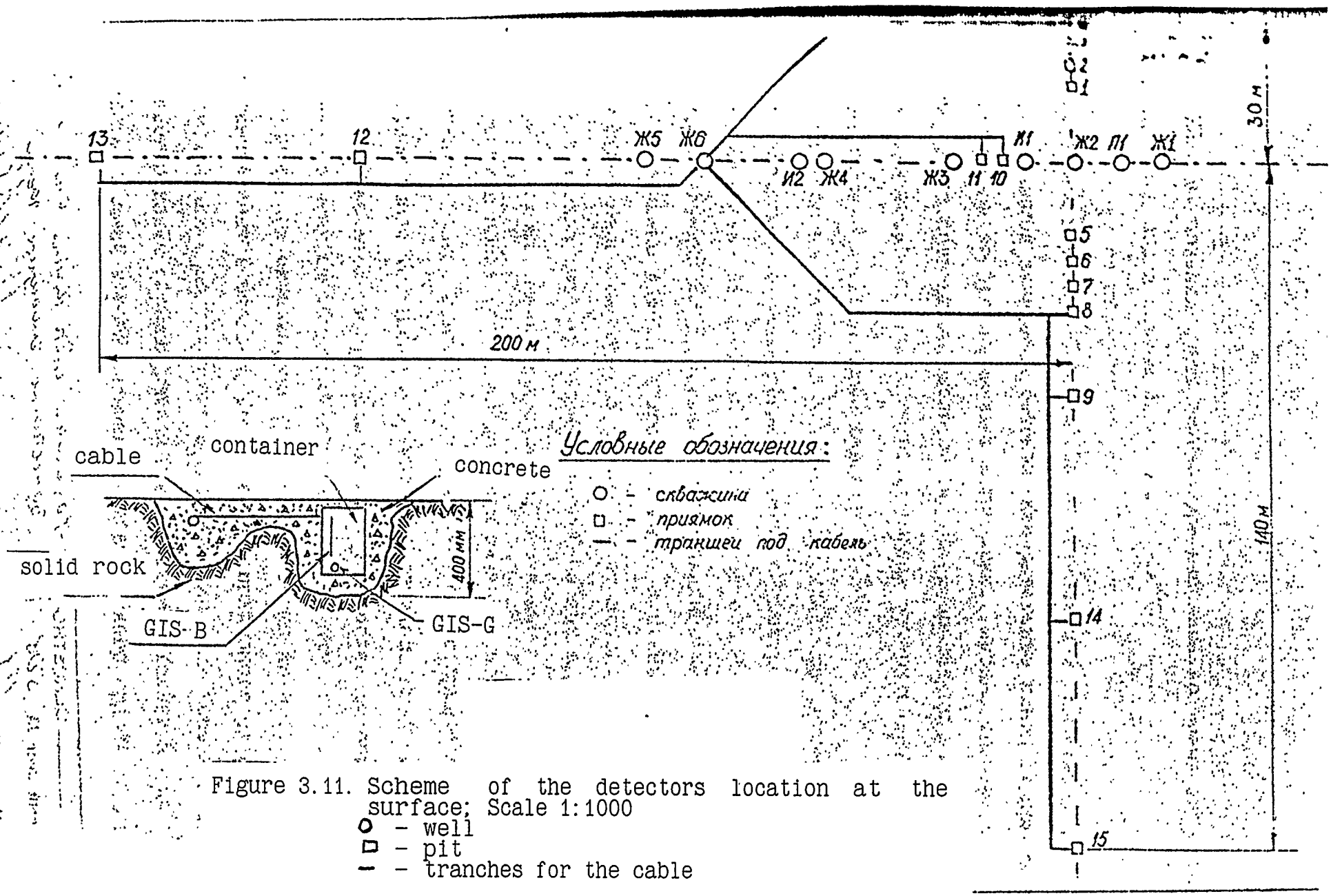

Figure 3.11. Scheme of the detectors location at the surface; Scale 1:1000

o – well

□ – pit

— – tranches for the cable

concrete. The measuring lines from these pits to the well G6 were lain in the trenches. The depth of the tranch in the rocky soil was equal to 30 cm. After the cable laying the trenches were filled up with mellow soil. The measuring cables were took out into the gallery throught the well G6.

In the gallery the detectors were installed to define possible dependence of the recorded parameters from their position and type of their installation. With this aim the vertical and horizontal detectors were placed at the same distances from the exit of the well G2 into the gallery in the roof and soil of the gallery and in the lateral niche, located at 1 m from the soil.

In the roof the detectors were placed on the details fasterned in the rock massif by means of the bars. After the detectors installation the niches were filled by concrete. The pits with the depth of 30-40 cm concreted after the installation and orientation of the detectors were made in the gallery soil. These pits were placed in the crushed rocks with thickness from 50 to 100 cm.

The cable lines from the measuring wells, the cable well G6 and the GIS detectors, installed into the gallery, were laid on the gallery soil in the metal boxes to the underground instrument construction. These boxes were covered by the layer of the soft soil with thickness of 20-30 cm to prevent the cable rupture because of the gallery collapse and stones fallouts.

All recoding instruments and GIS control panel were located in the underground instrument construction on the containers. The shock-absorption of the containers was realized by its hanging up at the rubber plaits to the beams fasterned at the upper part of the undeground instrument construction.

The measurements of the GIS detectors were registered by the oscillographs N-119 with the tape velocity equal to 2 m/s. All GIS detectors, including the detectors placed in the zone of the soil fallout, worked during the experiment. A part of the fallen detectors were torn from a cable lines in the process of the crater formation. All detectors installed in the well and gallery retained their efficiency and might be used at the second stage of the experiment.

It is known, that the parameters of the seismoexplosive waves in the zone, nearest to the explosion, are under considerable influence of the seismogeological and other conditions near the explosion. In this connection the thickness of the soft soil layer, necessary for the charge area creation, must be minimum. Before the creation of the charge area the layer of the eroded rocky soil was removed from the surface of

the massif at the mountain top. Topographic level before the works was equal to 752.9 m, but after the removing of the destroyed rocky soil and some stones it became 751.3 m. The thickness of the added layer, measured immediately before the charge loading, was about 40 cm along the area border and 1-2 cm near the centre.

3.5 Local effects of the explosion

As local effects of the explosion we consider the mechanical effects in the soil medium and at its surface connected with the crater formation: soilfall and pile formation, creation of zones of the distructions and residual displacements.

Typical crater profile after the superimposed explosion and system of the conventional signes are presented in Fig. 3.12.

The crater and pile profiles at N1-N5 and N3-N7 directions are shown at Fig. 3.13 and 3.14, and their paraneters - in Table 3.3.

The radius of the continuous pile was measured from the crater border at given direction down the slope. The pile crest is composed from large-fragmental rock with blocks up to 3.5 m. The pile represents the conglomeration of the rocky soil fragments with sizes up to 2.5 m. The spaces among the fragments are partially filled by small-fragmental materials of the rocky soil.

It was the first purposeful investigation of the soilfall after such large explosion in the rocky soil. It was founded, that the maximum fallout of the soil fragments was equal to $\sim$ 1350 m in N5 direction and $\sim$ 1200 m in N1 direction. The creation of the shock craters after the block fall is the characteristic feature of the soilfall. A great number of the falling stones wasn't destroyed after the impact, although some of them had considerable sizes.

3.6 Characteristics of the wave motion

From the measurements of the arrival time of the epicentral wave under the explosion centre it was ploted the hodograph (Fig. 3.15) showing that at the depth of about 10 m the P-wave velocity in the massif reaches 5300 m/s and it is constant to 120 m in depth.

The average velocity at the depth from 0 to 10 m is equal to 4550 m/s. The measurement of the arrival time by GIS

Table 3.3. Local action parameters.

Parameters	Direction number				Mean value
	1	3	5	7	
r_e, m	21.0	20.0	20.0	22.7	20.9
r_c, m	25.0	22.5	26.0	26.5	25.0
r_p, m	25.0	55.0	55.0	45.0	45.0
h_e, m	8.2	7.5	8.2	7.6	7.9
h_c, m	2.0	1.6	3.0	3.6	2.6
V_e, m^3	4460	5810	5310	6570	5540

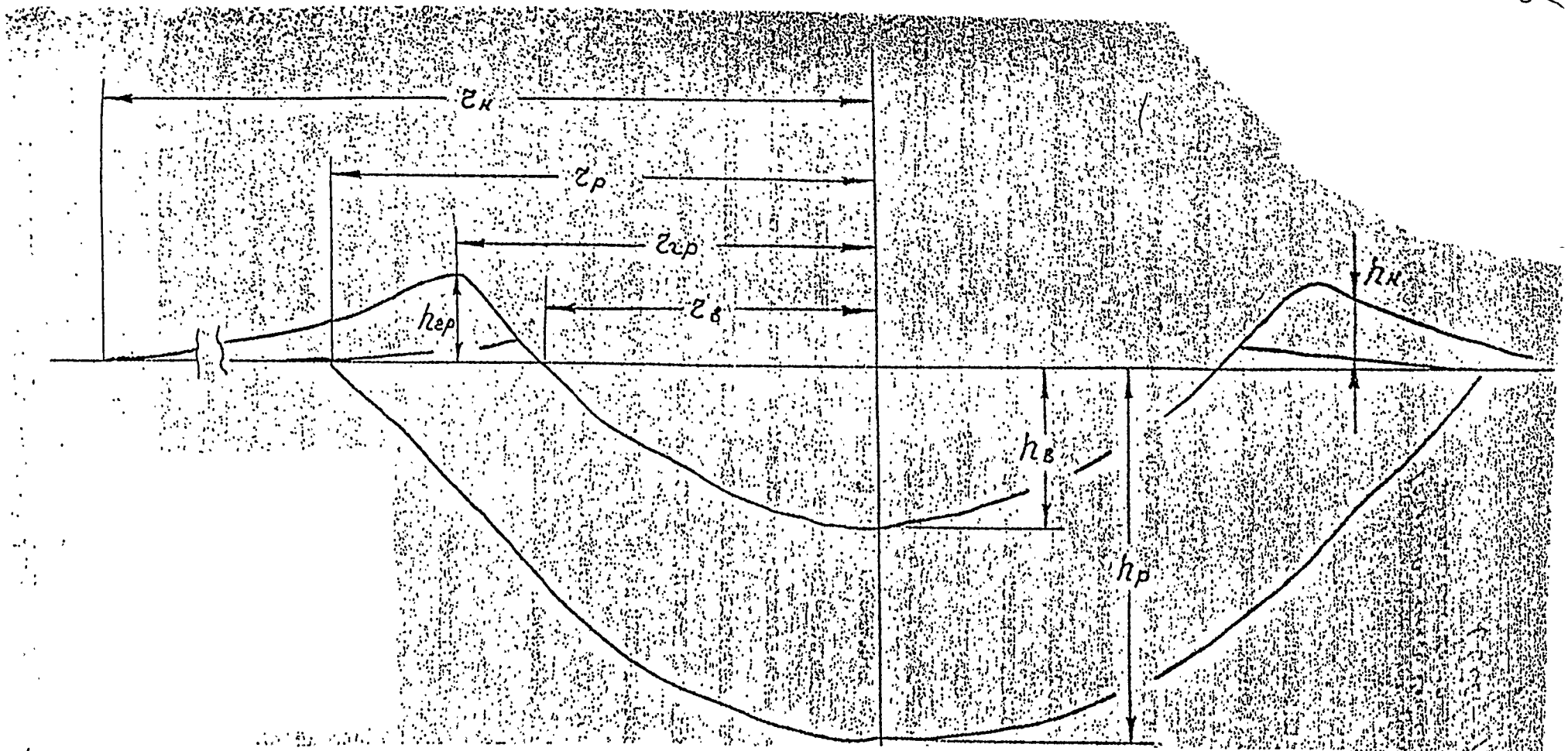

Figure 3.12. Typical crater profile and system of conventional signs:

$r_в$ - crater radius
$h_в$ - crater depth
$r_{гр}$ - crest radius
$h_{гр}$ - crest height
$h_н$ - pile thickness
$r_р$ - radius of the destroyed zone
$h_р$ - depth of the destroyed zone
$r_н$ - pile radius

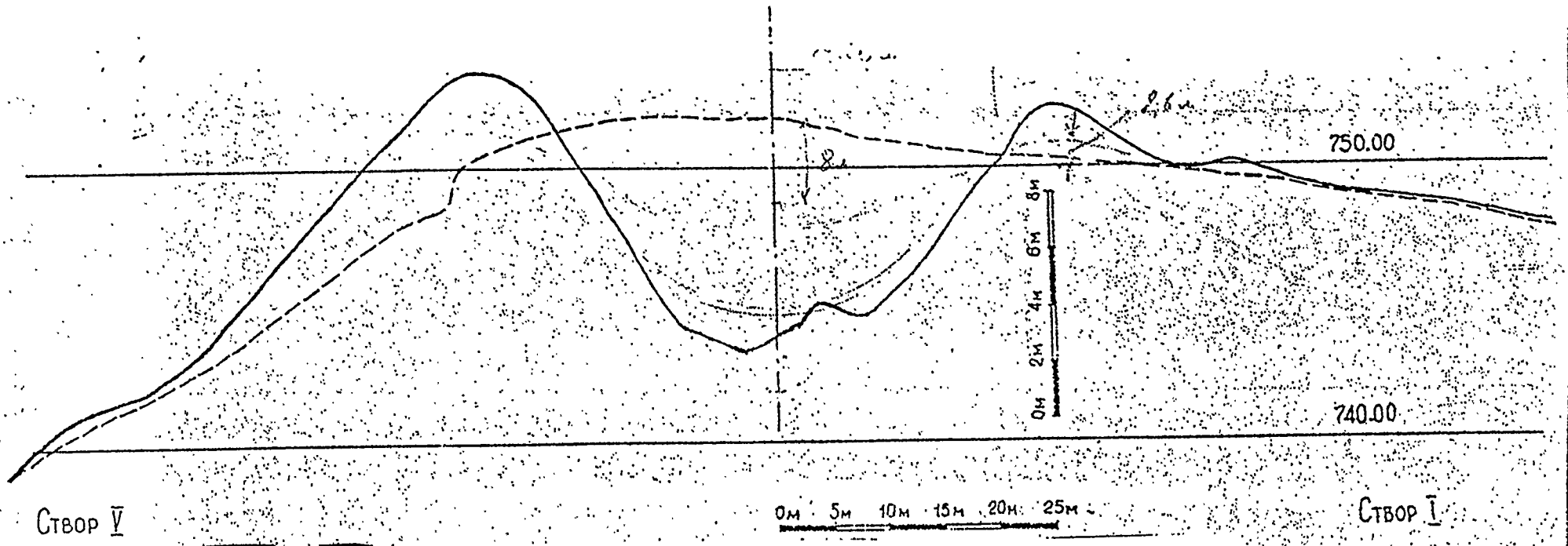

Figure 3.13. Crater profiles N1-N5
- - - - profile of the mountain surface in the direction N1-N5 before the experiment
~~~~ profile of the crater and pile in the direction N1-N5
~~~~

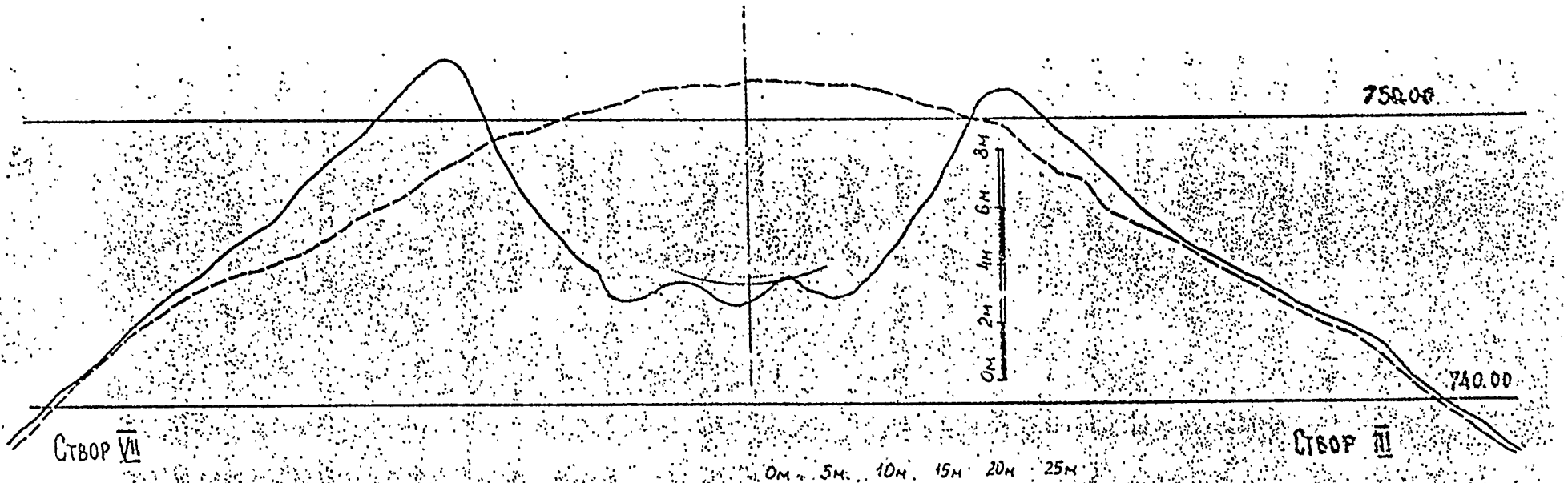

Figure 3.14. Crater profiles N3-N7

- - - - - - profile of the mountain surface in the direction N3-N7 before the experiment

~~~~~~ profile of the crater and pile in the direction N3-N7

Range III	Range VII
~~~~~~

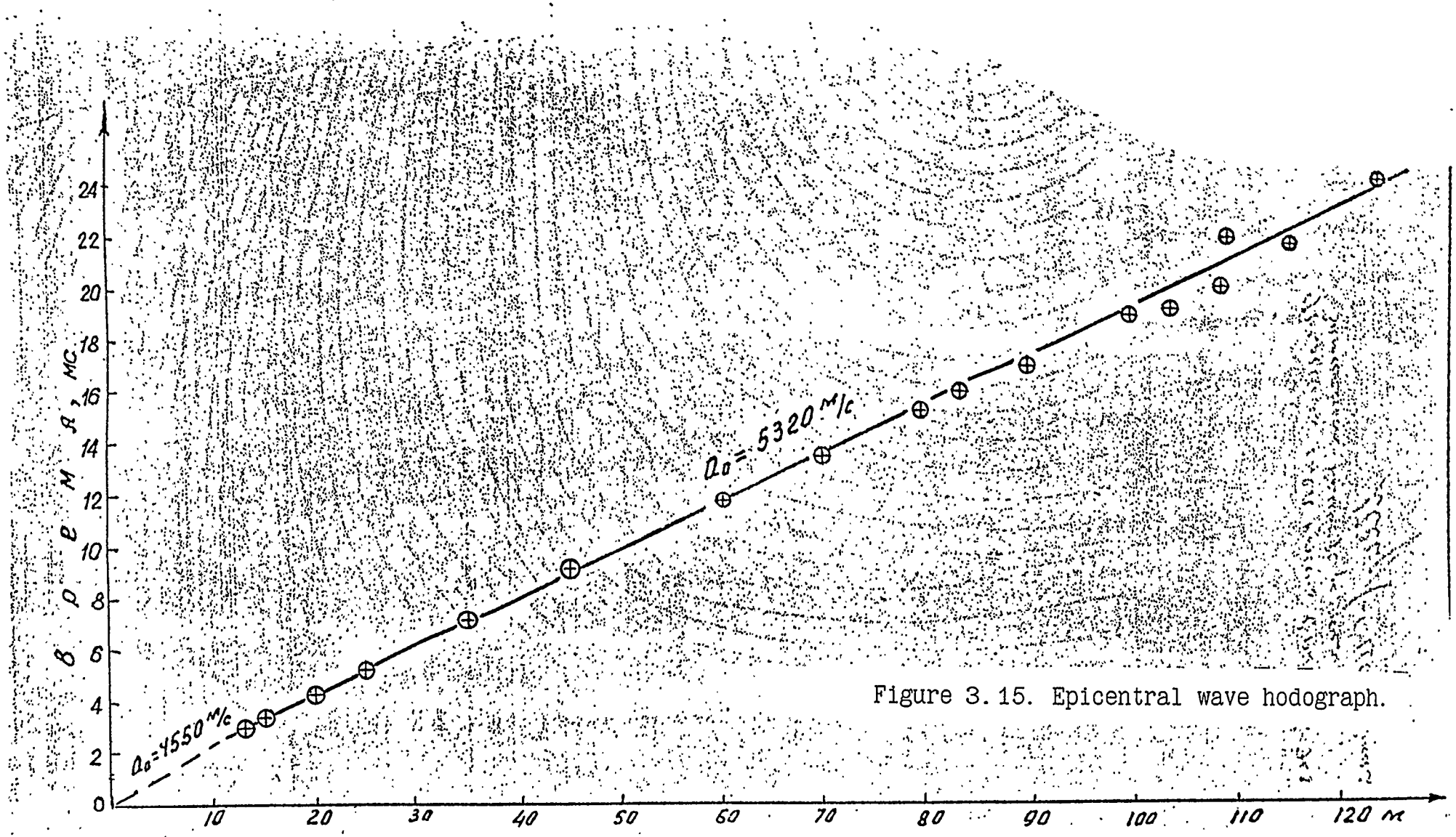

Figure 3.15. Epicentral wave hodograph.

detectors in the wells, gallery and at the mountain surface gives an opportunity to determine the location of the epicentral wave front at the different time moments (Fig. 3.16). The form of these fronts shows that inside the massif the wave is spread with the velocity of 5300 m/s, but along the massif surface this velocity is equal to 3500 m/s.

Apparently, the decrease of the wave velocity along the surface is due to the processes of the rock massif weathering.

Preliminary estimation of the mass velocity parameters in the epicentral wave shows, that under the epicentre there are predominant vertical motion with parameters gradually changing with the distance from the explosion centre (with the depth). When the investigated point approaches to the free surface of the massif (at the same distance from the explosion epicentre) we can observe the declination of the soil motion direction from the vertical line.

So, in the wells G3 and G1 the vertical component of the mass velocity is equal to the horizontal component at the depth of 20-30 m. Near the massif surface the first motion of the vertical component of the mass velocity is directed upwards. It is known that this change of the motion direction is connected with the influence of the free surface of the massif.

Near free surface the amplitude of the horizontal motion, usually, is greater than the vertical motion amplitude. The detectors, situated at the distance of 20 m from the explosion centre, recorded the splitting effects in the nearsurface soil layer.

The oscillograms of the soil mass velocity, recorded by the detectors in the pits, obviously registered the compression wave from the air shock wave. The amplitude of this wave at the distance of 145 m from the explosion centre is 152 sm/s. The compression wave from the second air shock wave are obviously registered 250 ms later. Its amplitude is about 30% from the amplitude of the first compression wave.

The analysis of the measurements of the soil mass velocity in the gallery shows that the value of this velocity is not the same at the different points of the gallery cross-section. The maximum velocity was observed in the roof and the minimum velocity - in the gallery soil. Sometimes, in the gallery soil the first motion is directed upwards and then this motion is directed downwards with the gravity acceleration. Evidently, it might be explained by the fact that the disturbance spreads to the detectors by the diffraction at the gallery walls.

In this case, the motion analogous to the upwards motion

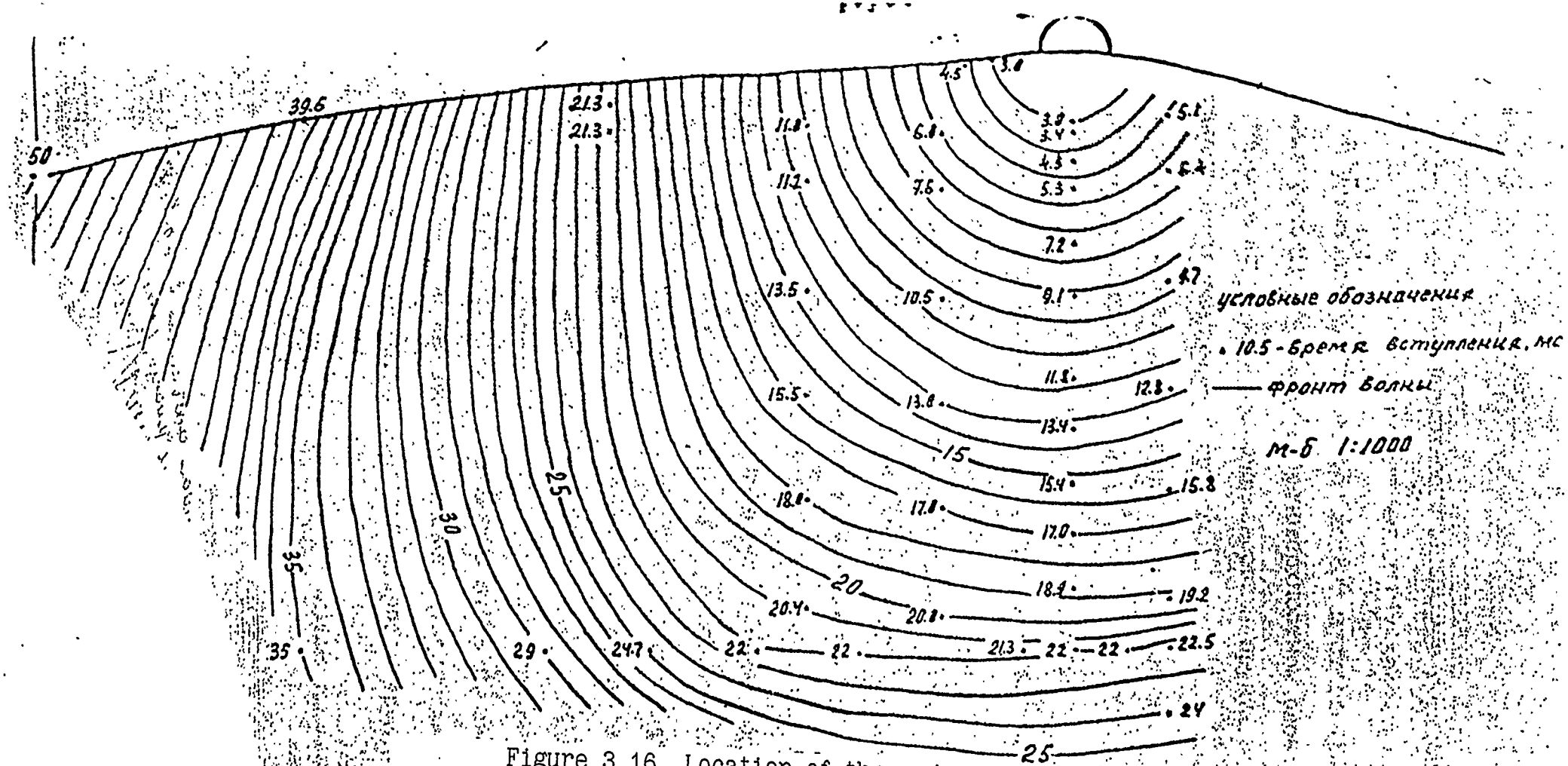

Figure 3.16. Location of the epicentral wave front
Scale 1:1000
•10 - arrival time, ms
—— - wave front

near the free surface of the massif must be observed in the gallery soil. In addition, the oscillograms show that the layer of the destroyed soil in the gallery greatly cuts off the high frequency component of the oscillations and increases the oscillation periods.

The comparision of the mass velocity parameters in the gallery and massif shows that the mass velocity in the niches roughly equal to the velocity in the massif, but the velocity in the gallery roof is greater then the velocity in the massif at 20-30% approximately.

Typical oscillograms of the mass velocity at the rock massif surface, inside the massif and in the gallery are represented at Fig. 3.17.

The motion parameters of the first and second explosions at the symmetry axis (i.e. under their centres) are the most important for the comparision of the motion parameters of these explosions. The motion of the vertical component in the first phase are directed downwards and maximum amplitude at all distances are observed in the first phase of the motion. The time of the mass velocity growth increases with the increase of the distance: from 1 ms at 13-20 m to 2.5 ms at the distance of 90 m. The first phase duration of the mass velocity changes nonmonotonously. It increases up to the distance of 80 m and then decreases.

Such character of changes of the first phase duration, as it is generally known, is observed under the centre in the experiments with all types of the comparatively uniform media and it is the most pronounced in the uniform soft soils.

The second phase of the motion gradually increases with respect to the first phase with the distance from the explosion centre. The maximum parameters of the motion are presented in Table 3.4.

The value of the soil mass velocity under the explosion centre is shown at Fig. 3.18.

The parameters of the seismoexplosive of waves in the distant zone were registered in the distance range of 500-38200 m along two profiles with azimuthes of 0° (in the direction to KPA) and 90° (along the mountain crest). Seismometers S5S, OSP, VEGIK and SM-3 were used for these measurements. The detectors were oriented in the radial (X), tangential (Y) and vertical (Z) directions. Light-ray oscillographs N-700, N-115, and OMS with galvanometers GB were used for the registration. Parameters of the measuring channel of the detectors S5S, SM-3 and VEGIK with the galvanometers permited to record the displacement in the

Table 3.4 Parameters of the rock massif motion under the explosion centre (the well 62)

Depth, m	Arrival time, ms	Time of the velocity increase, ms	First phase duration, ms	Maximum velocity cm/s	Maximum acceleration, m/s^2	Maximum displacement, mm
13	3.0	1.4	3.4	6915	100000	400
15	3.4	0.9	1.4	3458	200000	110
20	4.3	0.7	1.9	1552	32000	50
25	5.3	1.0	12.0	1302	19000	30
35	7.2	1.0	14.4	-	-	-
45	9.1	1.4	15.4	400	4000	20
60	11.8	2.2	15.8	230	1200	15
70	13.5	2.2	16.8	164	1100	15
80	15.4	2.4	21.6	109	600	8
90	17.0	2.5	20.7	61	400	5
100	18.9	2.3	20.2	58	370	5

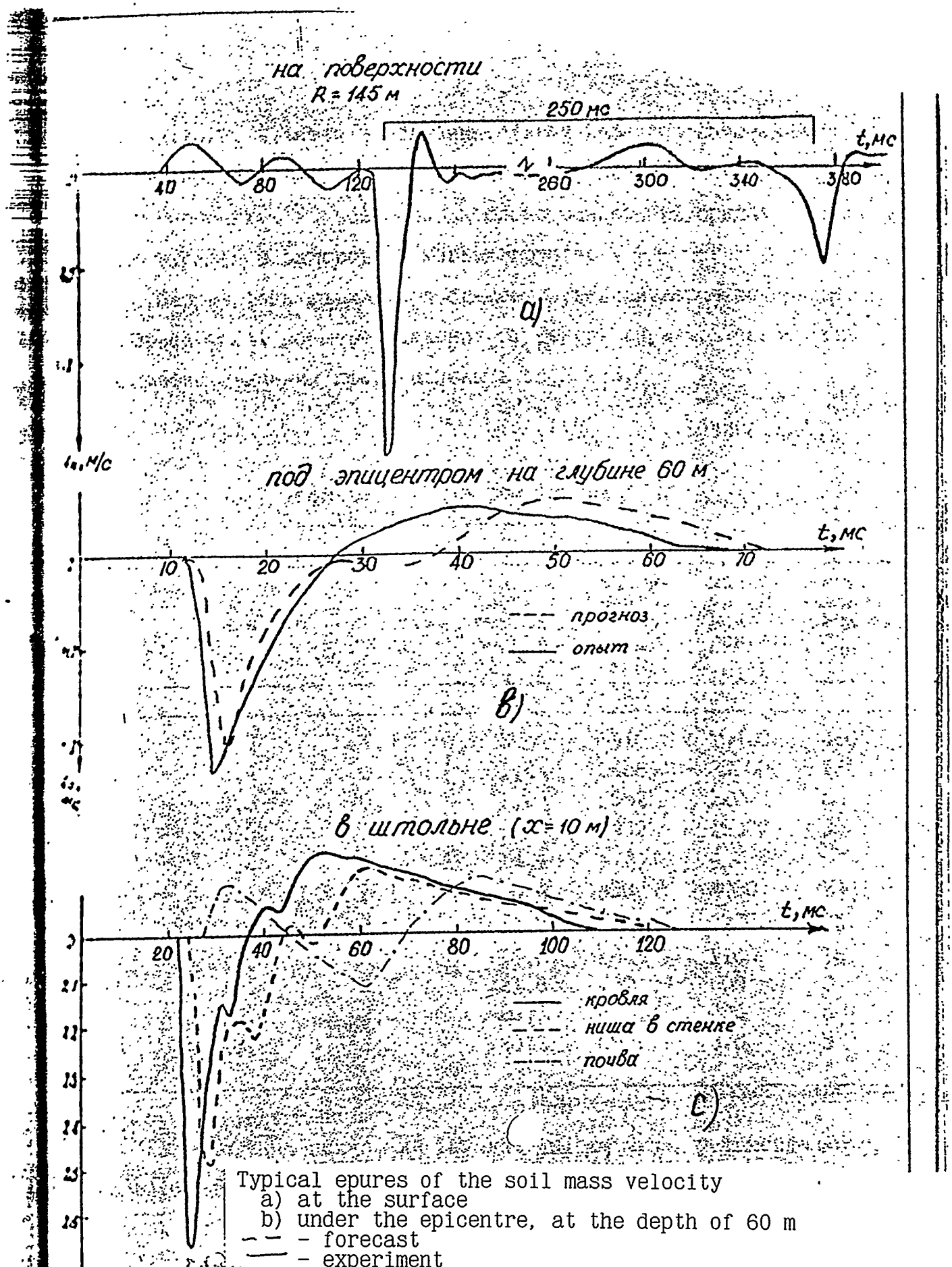

Typical epures of the soil mass velocity
a) at the surface
b) under the epicentre, at the depth of 60 m
– – – forecast
——— experiment
c) in the gallery
——— roof
– – – niche in the well
– · – · – soil

Figure 3.17.

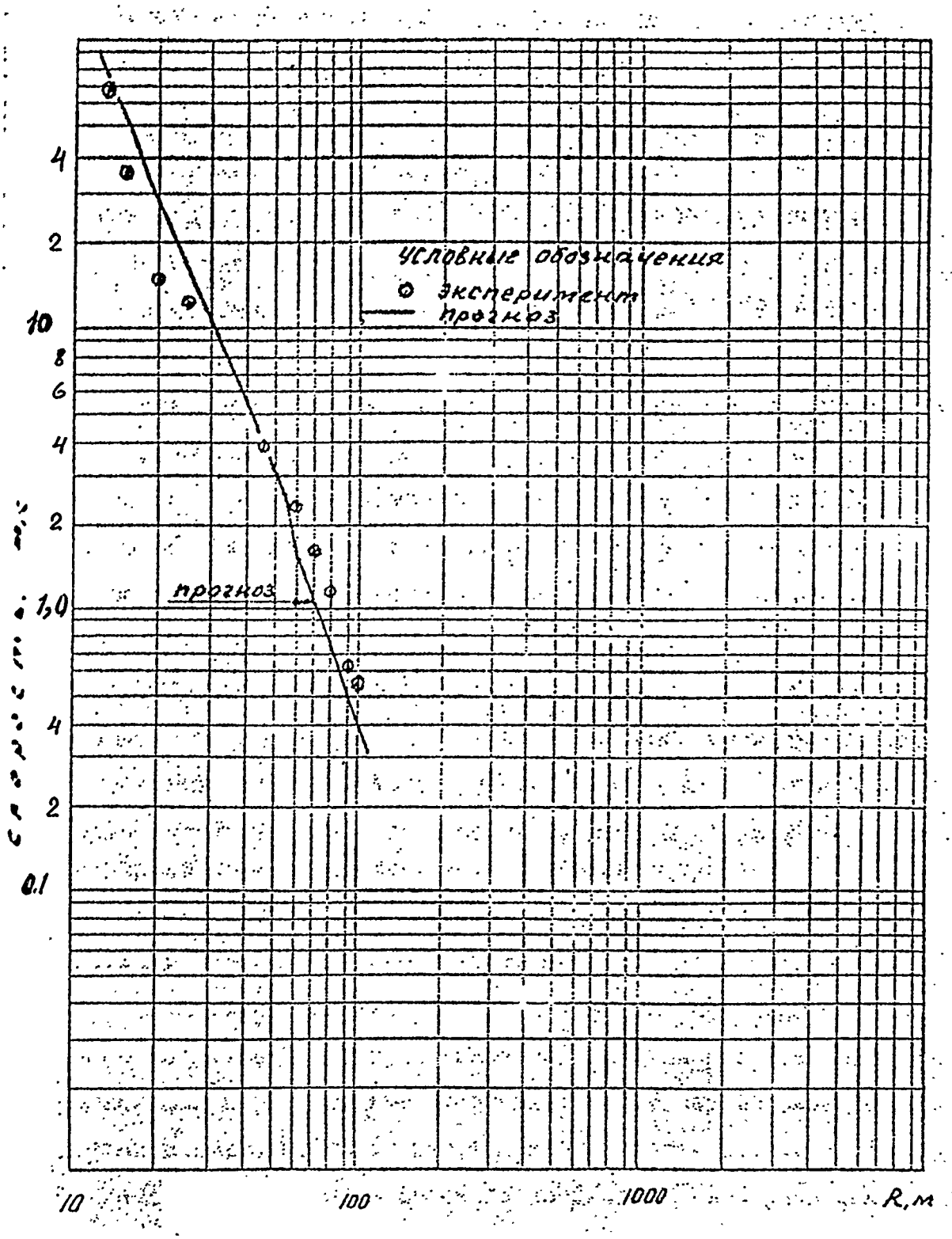

Figure 3.18. Mass velocity of the soil under the explosion centre:
O - experiment
—— - forecast

wave and the OSP detectors, which give an opportunity to measure the displacement velocity. The registration was realized in the frequency band of 0.5-100 Hz with the increasing from 1 to 1050.

As an illustration, the copies of the oscillograms from SM-3 at the distance of 2900 m along the profile with azimuth 0° are shown at Fig. 3.19. There are marked first phases of P-, Sand R-waves at these oscillograms. The velocities of these waves are equal to 5.4 km/s, 3.12 km/s and 2.7 km/s correspondingly.

The most reliable and representative data were obtained from the displacements in P-wave. The maximum radial displacements W_{px} in the first phase of P-wave in dependence on the distance for both profiles are presented at Fig. 3.20. It is obviously from Fig. 3.20, that the displacement in the wave along the pfofile 90° is in twice greater than along the profile 0°, and this discrepancy exeeds the scattering of the experimental data. It is connected, to all appearance, with the differences in the engineering-geological structure of the massif in all directions shown in the site topography.

Along the profile with azimuth 0° the recorded stations were placed up to the distance of 38.2 km. The graphics of the displacements in the first phase of the oscillations at Z- and X-directions (W_{pz}, W_{px}) in whole distance range are presented at Fig. 3.21 and 3.22. From these plots it can be seen that the wave attenuation at the distances up to 10 km is greater than in the distant zone.

Besides the wave types described above, the oscillations due to the air shock wave action are clearly seen at the seismograms. The seismic action of the air shock wave is most pronounced at Z-components, and two air shock waves might be distinguished with confidence. The times of the first phase of the first (1) and second (2) seismic signals are represented at Fig. 3.23.

Amplitude of the soil oscillations from the first air shock wave is in 4-5 times greater than from the second. The oscillations are directed vertically downwards. The time of the increasing of the velocity to its maximum is in 3-10 times less than in first phase of the wavetrain.

The experimental values of the maximum mass velocities V_z due to the air shock wave are shown at Fig. 3.24. The solid line

below the experimental data presents the dependence, calculated from known pressure and physico-mechanical characteristics of the nearsurface soil layer.

Table 3.5 gives a comparision of the soil oscillations

Table 3.5. Comparision of the velocities of soil oscillations.

Distance, m	Velocity of the soil oscillations, mm/s		
	V_{Pz}	V_{Rz}	V_z
1000	6.60	-	47.5
2000	0.54	3.5	3.0

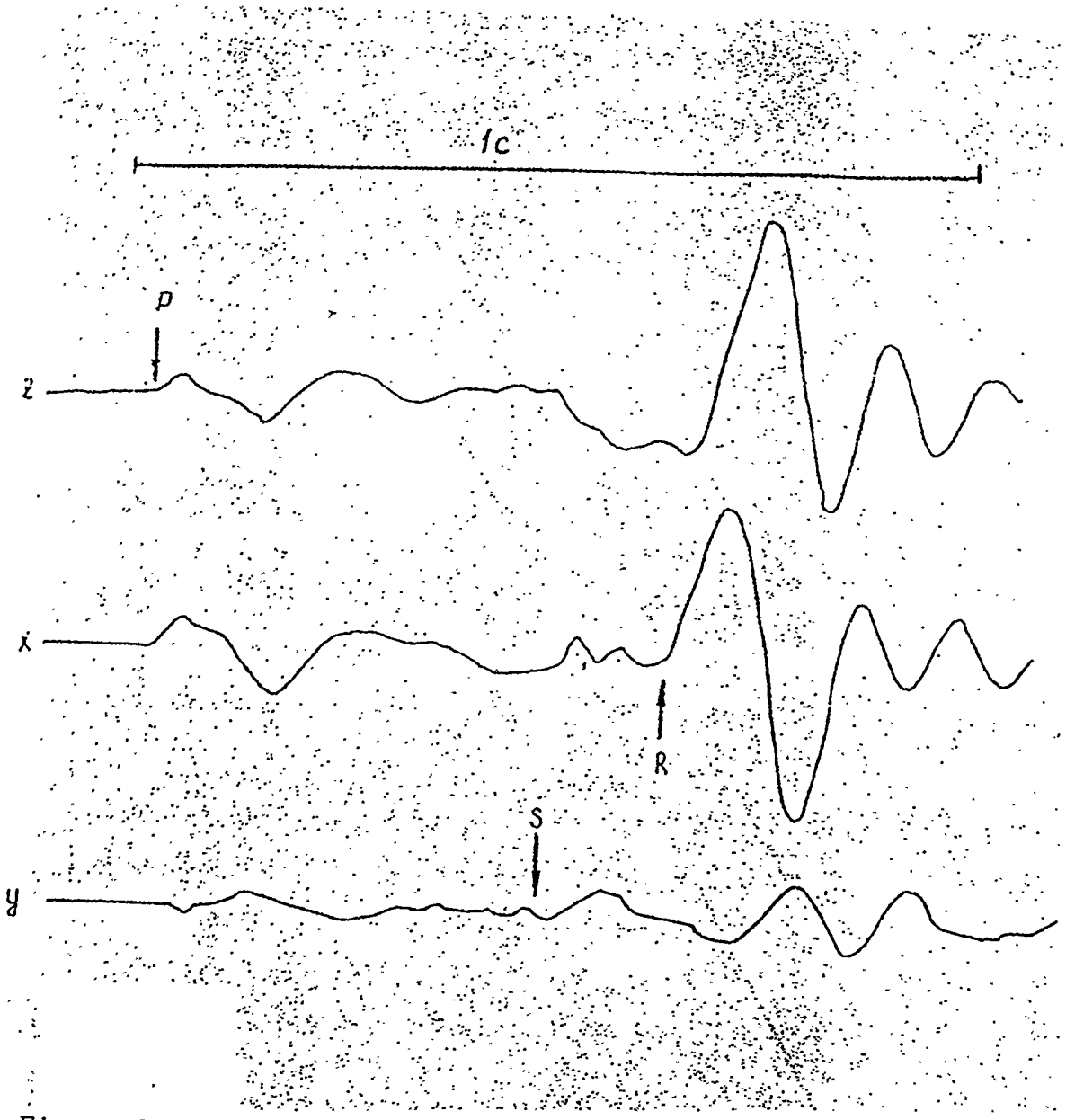

Figure 3.19. Record from the seismometer SM-3 at a distance of 2900 m.

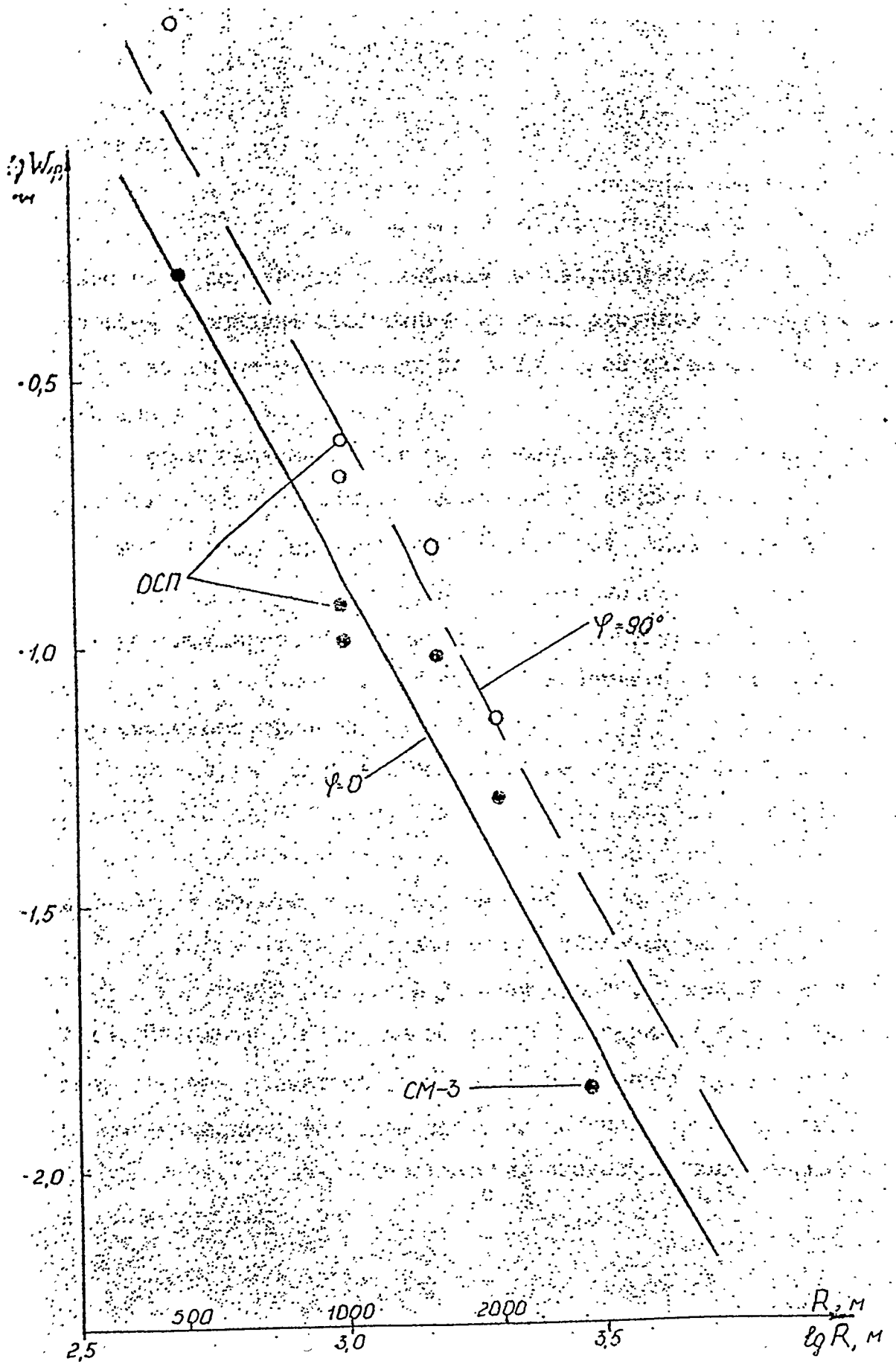

Figure 3.20. Displacements in P-wave along the different azimuth.

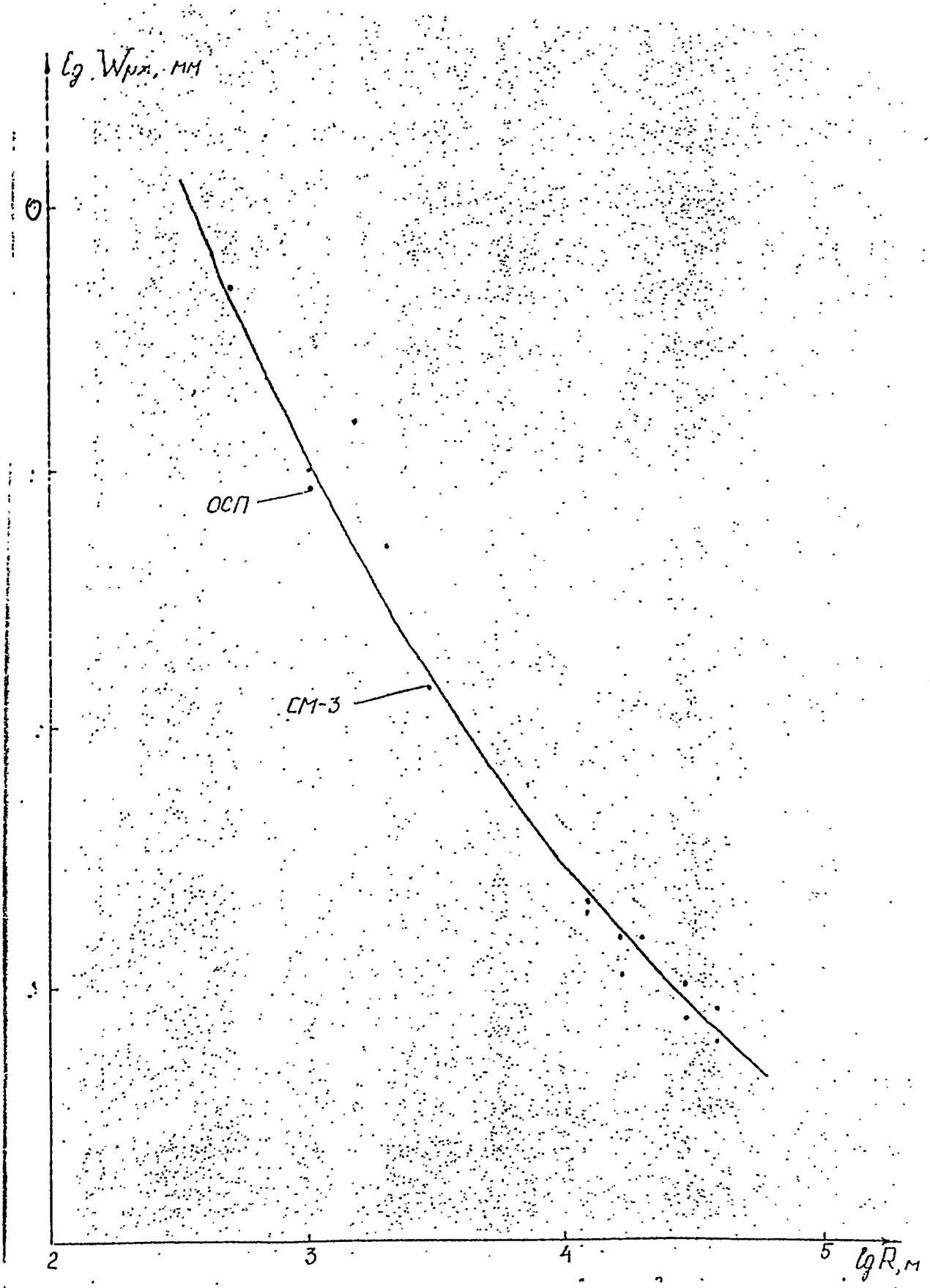

Figure 3.21. Radial displacements in P-wave.

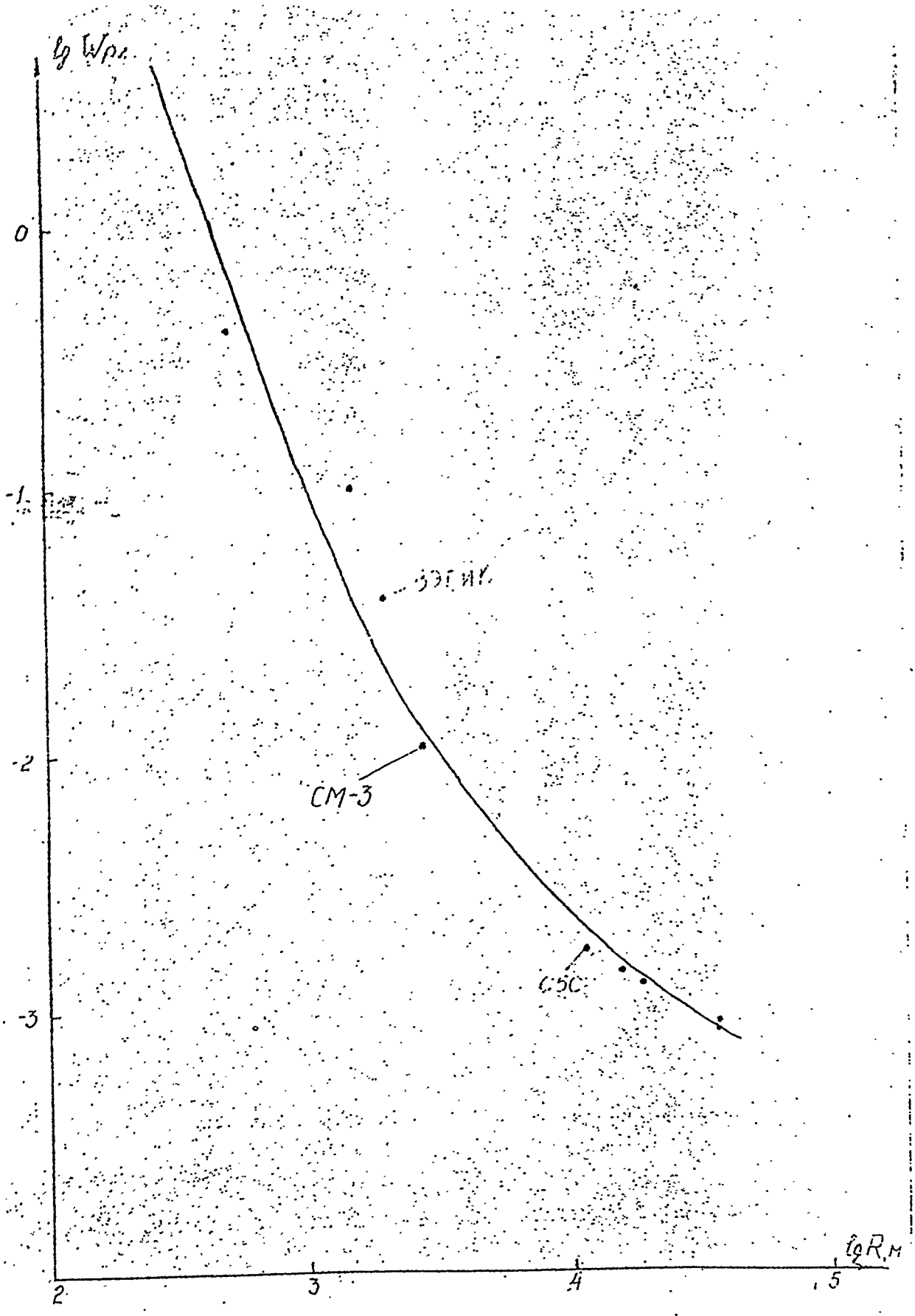

Figure 3.22. Vertical displacements in P-wave.

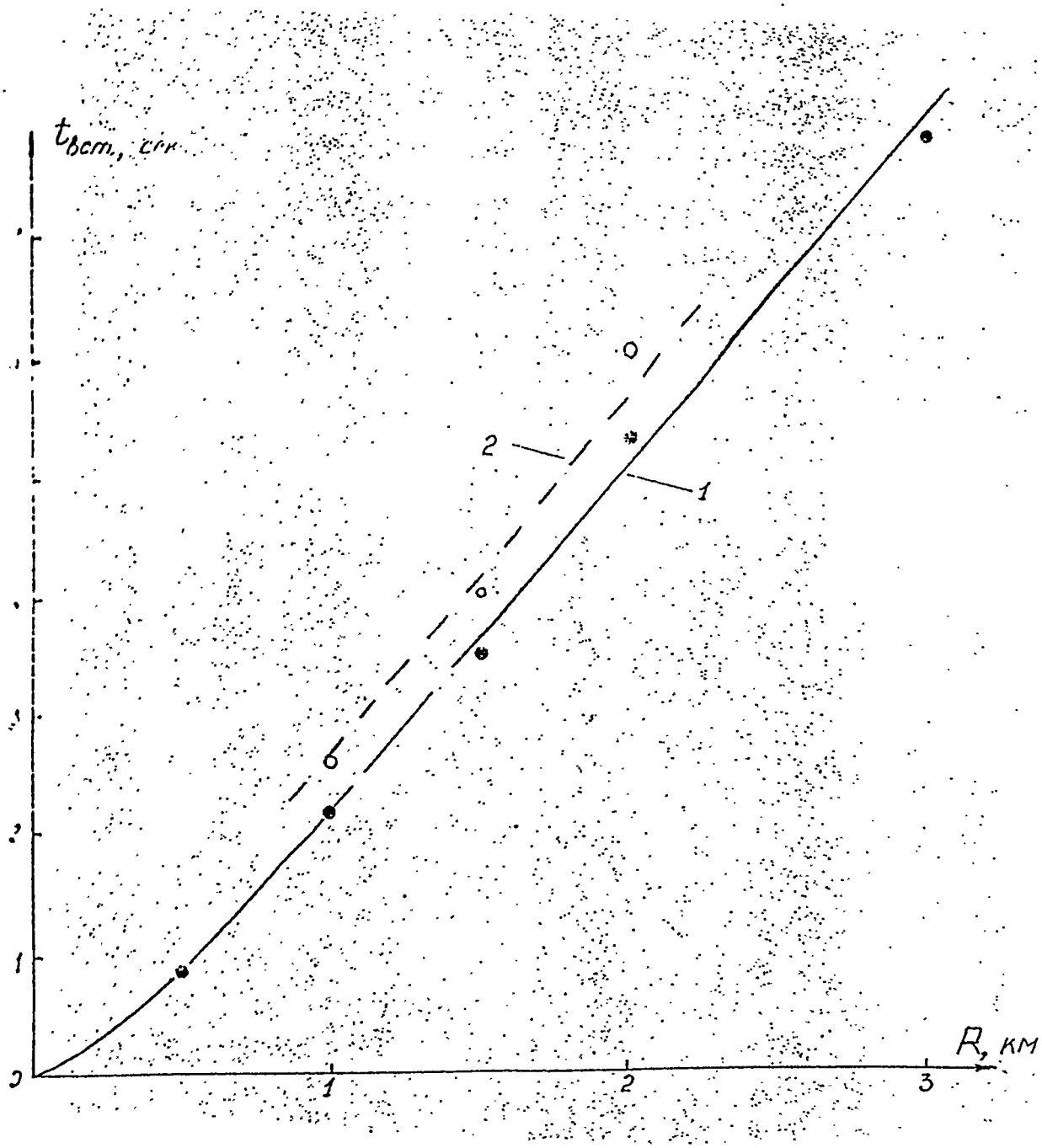

Figure 3.23. Hodograph of the seismic wave from the action of air shock wave.

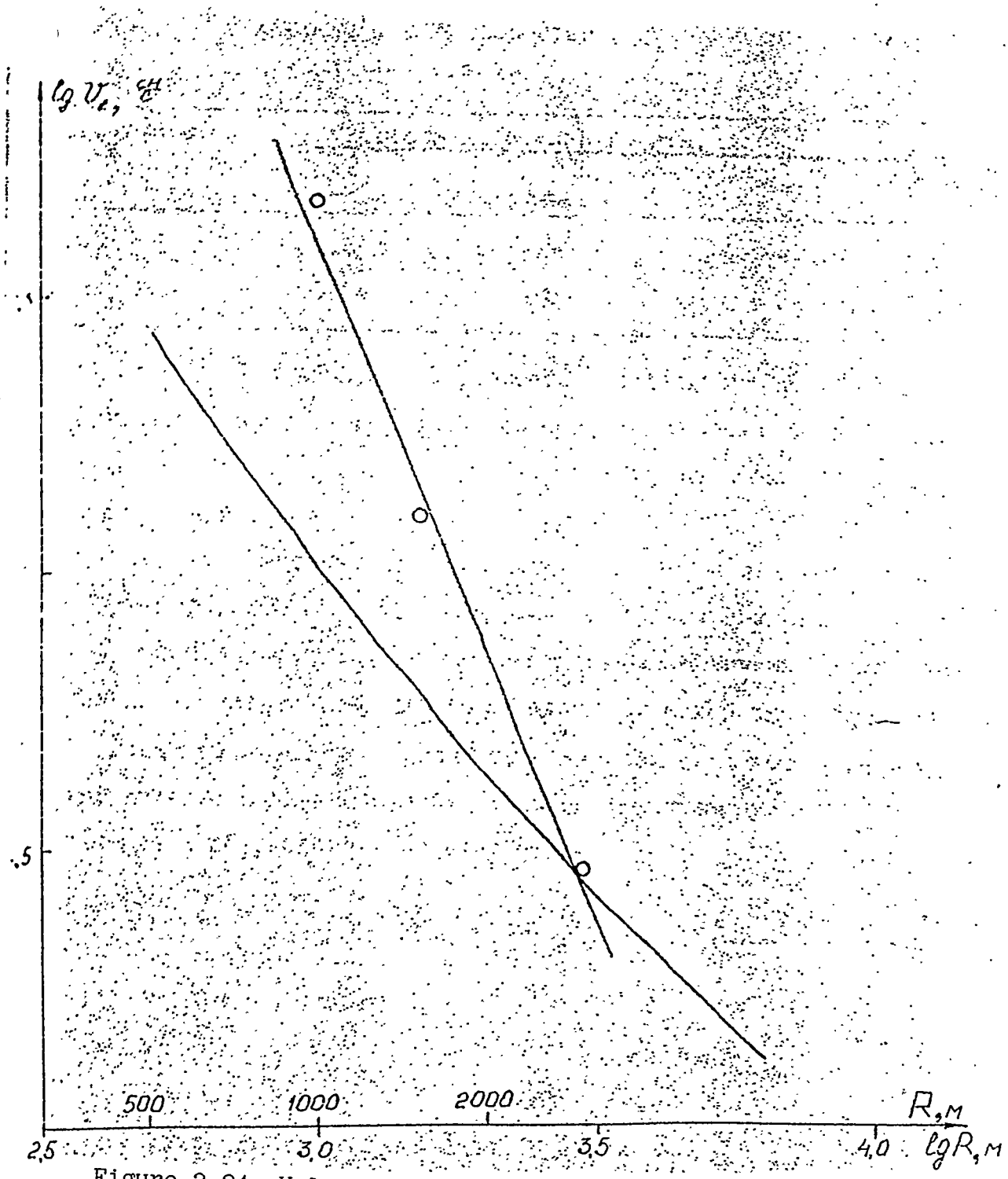

Figure 3.24. Velocity of the soil displacement bacause of air shock wave action.

velocities for the different wave types.

As shown in Table 3.5 the velocity of the vertical oscillations due to air shock wave is considerably greater than the velocity in the first phase and roughly equal to the oscillation velocity in the surface wave.

It should be noted that at the distance of 12 km the oscillations due to weak air shock wave might be confidently distinguished, but it is impossible to give a quantitative estimation of the redundant pressure because of the small amplitude of this records.

3.6.1. Influence of the crackness of rock massif on the epicentral wave parameters.

The graph at Fig. 3.25, gives an opportunity to consider the peculiarities of the epicentral wave spreading after the explosion. As it was noted, the multiplication of the wave amplitude by the distance describes spherical discrepancy in the near front area for the elastic spherical wave well enough.

As regards the experiments with contact or near-surface explosions, it was repeatedly noted that near the vertical axis in the elastic medium the dependence of the maximum velocity on the distance is similar to the analogous dependence for a camouflet explosion.

For the spherical wave it is possible to write the well-known binomial expression, which in the current conventional signs will be the follow:

$$V = \frac{\Phi'(\tau)}{R \times c} + \frac{\Phi(\tau)}{R^2}, \quad \tau = t - R/c \qquad (3.1)$$

where Φ - the potential of the displacement velocities.

If the value of $V(t)$ at the distance R is known, the potential Φ is defined as:

$$\Phi = e^x \times \int_0^x e^{-x} \times (\nu \times R^2)\, dx \qquad (3.2)$$

with $x = \tau \times c/R$. Accordingly, from the equations (3.1) and (3.2) we have the next expression for Φ':

$$\Phi' = (\nu \times R \times c) - \Phi \times c/R = \nu \times R_c - e^{-x} \int_0^x e^x\, (\nu \times R_c)\, dx$$

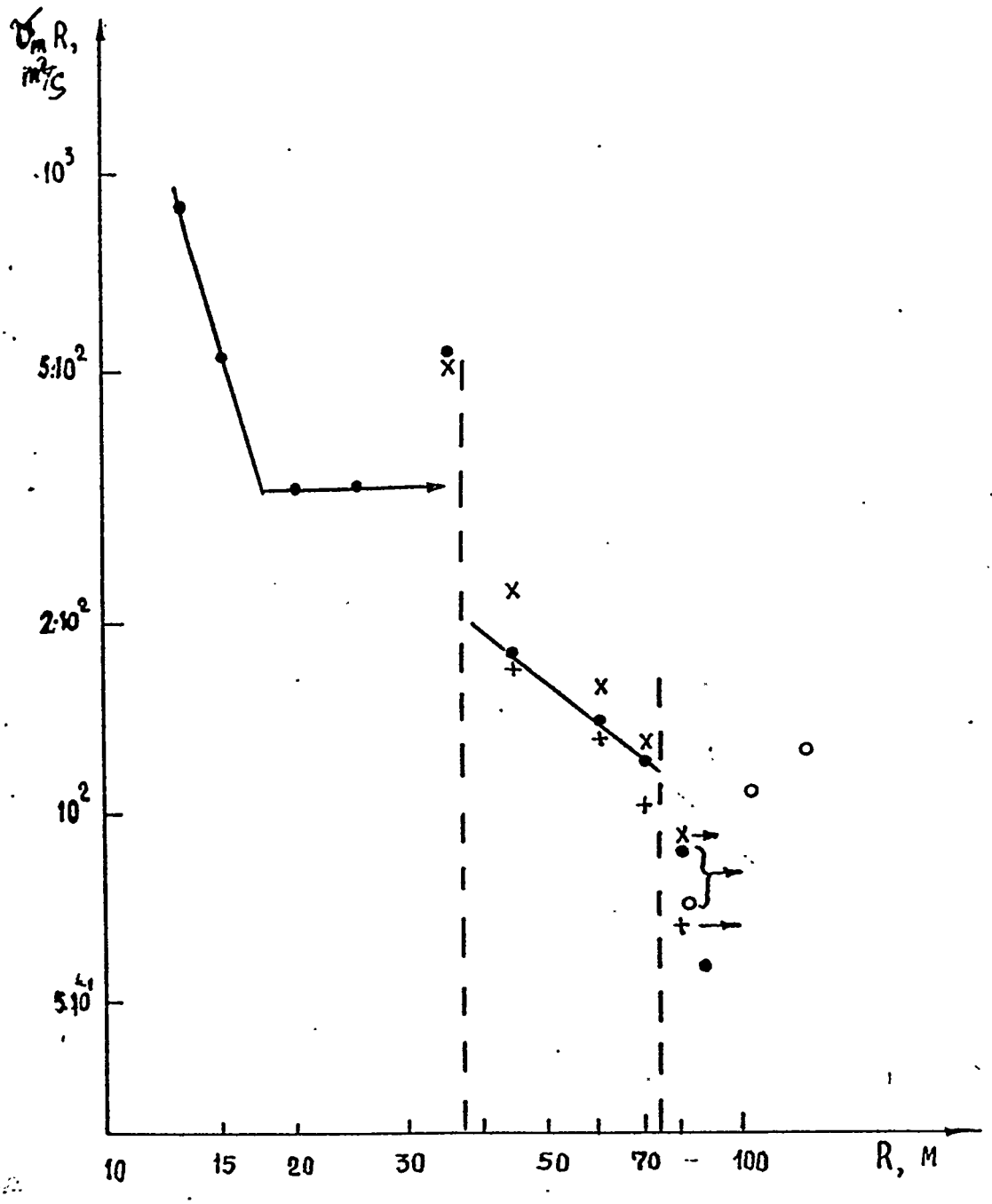
$\sigma_m R$, m^2/s
10^3
$5 \cdot 10^2$
$2 \cdot 10^2$
10^2
$5 \cdot 10^1$
10
15
20
30
50
70
100
R, м

Figure 3.25.

If $x \ll 1$, we have the follow estimation:

$$e^{-x} \int_0^x e^x \ (\nu \times R_c) \ dx \sim \nu \times R_c \times x,$$

i.e. $\Phi' = \nu \times R$ and $\nu = \Phi'/R$.

When the time of the velocity increasing to the maximum value are $t_n \sim 1 \div 2$ ms at the distances of R = 60 m and with c = 6 km/s, it is possible to ignore the contribution of the second term of the equation (3.1) because $x = t_n \times c/R = 0.1 - 0.2$. So, for the typical times of the velocity increasing in this experiment the correction of the ν_m value is negligible and in the first approximation the next ratio must be true for the elastic wave:

$$\nu_m = 1/R, \text{ i.e. } \nu_m \times R = \text{const}$$

At Fig. 3.25 it is possible to see a several characteristic areas. Firstly, there is an evident decrease of the $\nu_m \times R$ with the distance at the area of 20 m. This decreasing might be connected with the non-elastic spreading of the wave in the weathered zone. Further, it is possible to mark out the area of 20 m < R < 35 m, when the value of $\nu_m \times R$ doesn't change with the distance.

At the zone of 35 m < R < 70 m, which is marked by the vertical dashed lines at Fig. 3.25, the value of $\nu_m \times R$ changes slightly, by when R > 80 m there is observed sudden some change of this value and then this multiplication is nearly constant or, sometimes, it increases (as for the data from the well G-1, marked by the light circles at the Fig. 3.25). It is typical, that when R = 35 m the value of $\nu_m \times R$ increases in 1.5 times.

This dependence at Fig. 3.25 can be explained from the viewpoint of the model of the discrete disturbances proposed here. Non-eroded massif of the solid rocks begins from the depth of about 20 m and after 15 - 17 m the incident wave meets the first large subhorizontal crack and is reflected from it. This reflection gives the sudden change of the $\nu_m \times R$ value, but beyond the cracks net this value increases in 1.5 times. Further, the wave passes through the crack net, and at the depth of about 75 m, where this net is closed, the value of $\nu_m \times R$ suddenly decreases again.

From the massif description the subhorizontal cracks (with the angle to the horizont of about 20°) with the distance among them of about 10 m might be occurred at these depths. So, in the distances range from 35 to 75 m it's should be expected the occurrence of three or four cracks, i.e. the system of three-four blocks (l = 10÷12 m). As we can see from Fig. 3.25

the value of $\nu_m \times R$ decreases after the passing through this system in 4-5 times, in comparision with the initial value.

The parameters of the cracks net and possible law of the wave decreasing with the distance might be obtained from the results of the previous calculations. The one-dimensional scheme for the flat wave might be immediately used for the estimation, since the wave discrepancy is taken into consideration in the ratio $\nu_m \times R$ for a spherical wave. Furthermore, the relations between the normal stresses and wave velocity for a spherical and flat wave are the same.

Let's estimate the system parameter a from the hodograph of the wave arrival t_0 and wave maximum t_m shown at Fig. 3.26. From the hodograph we can receive the next parameters: C_0 = 5.3 km/s and C_m = 4.2 km/s. Since C = 6 km/s, the value of a is equal 1. With this a it is possible to use the results of the previous experiment and calculations immediately. The Fig. 3.25 presents two variants: the oblique crosses represent the behavior of the amplitude variation ($\nu_m \times R$) in the areas of the detectors displacement (45, 60, 70, and 80 m) in the scheme, from which t_0 = 4, l = 10 m, and the cracks are situated at depth of 37, 47, 57, 67, and 77 meters.

The straight crosses represent the results of the calculation shown at Fig. 3.25: initial impulse is $\nu_0 = e^{-x}$, l = 12 m, and the cracks are situated at depth of 37, 49, 61, and 73 meters. In the both cases the horizontal level of $\nu_m \times R$ at the zone of $10 < R < 35$ was considered as initial. As we can see the results of the calculation are in a good agreement with the experimental data, that allows to estimate the transferred impulse and mean character is the time for the cracks θ. So, if l = 10÷12 m and a = 1 m, we can write:

$$\theta = \frac{l \cdot a}{2 \cdot C} \sim 1 \text{ ms}, \quad \bar{\tau}_0 = \tau_0 / \theta = 4, \quad \tau_0 = 4 \text{ ms}$$

Let's estimate the effective thickness of the crack with known θ. Since $\gamma = 10^2$ and l = 10 m we obtain $l_T \sim 10$ cm. So, the characteristic time θ for the cracks in the non-eroded part of the massif is about of 1 ms. Let's compare this value with θ for a greater cracks. For cracks with $l_T \sim 1$ m θ is equal to 10 ms and for Fergano-Tallas fault with $l_T \sim 100$ m θ is about 100 ms.

It is interesting to note, that the increasing of the θ value is connected with the block size, i.e. with the distance between the cracks and faults. The block scale in the experiment was equal to 10 m, the large cracks with θ = 10 ms usually are situated at the distances of about a few hundreds

4-20-3р

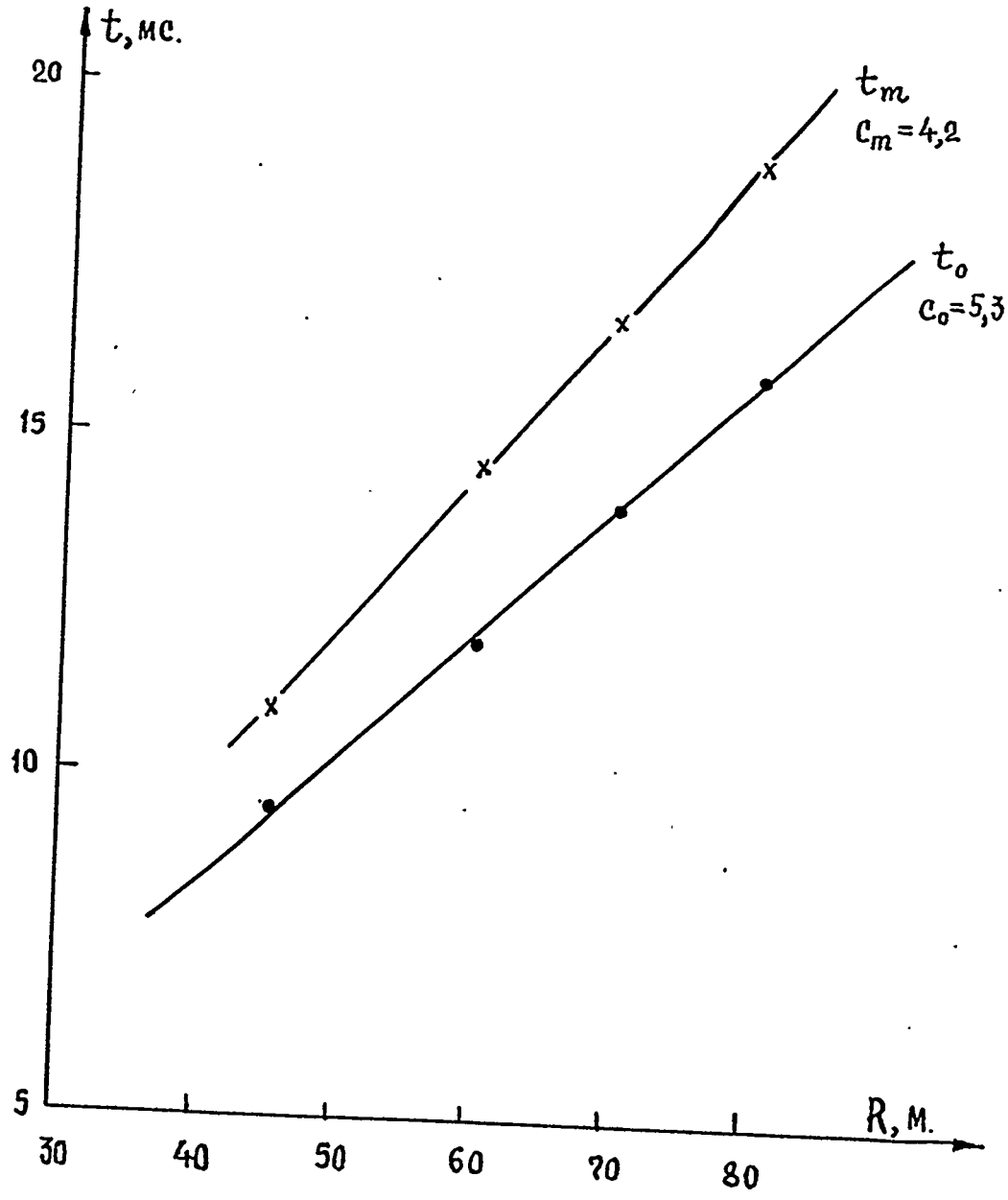

Figure 3.26. Hodograph of the wave arrival t_0 and wave maximum t_m.

meters, but the distances between the faults are tens and hundreds kilometers.

It is possible to estimate the variation of the positive phase duration τ_1 with respect to the distance. As τ_0 = 4 ms it is easy to obtain that in the experiment at a distance of 45 m τ_1 must be equal to 8 ms, and at a distance of 80 m it increases to 10 - 12 ms. Now it should be emphasized that the using of the simple model of the flat wave at the end of the positive phase $V(t)$ isn't substantiated, because with the time the question of the wave geometry and of the reflection peculiarities has greater and greater importance. So, in this work we will confined oneself only to above estimation, but we note that the addition of the second term in the equation (3.1) will lead to the increasing of the positive phase duration.

3.7 Deformation of the rock massif

To measure the deformations in some points of the massif semi-conducting detectors of the deformation (DDP) were installed in the gallery. This detector is a cylinder from duraluminium with 25 mm in diameter. At its butt-end two semiconducting tensoresisters KTE-7A were stuck in two perpendicular directions.

The detector was fastened in the bore-hole with the diameter of 37 mm by the melting sodium sulphate. The accurate definition of the detector taring by the creation of the known stress-deformable state by means of the stimulation of the elastic waves by the impact of the steel firing-pin and the gallery walls was realized immediately in the place of the detector installation.

The process was registered by light-ray oscillographs N-117 and N-119 with different tape velocities.

The residual deformations were registered during a hour after the explosion.

Three two-component deformometers were installed in the gallery walls. Two of them were placed at 20 m and the third - at 10 m from the epicentre.

The registered oscillograms of the deformation in the wave are represented at Fig. 3.27, and the residual deformations are shown at Fig. 3.28.

The data analysis shows that the values and epures of the measured deformations in the compression wave are in a good

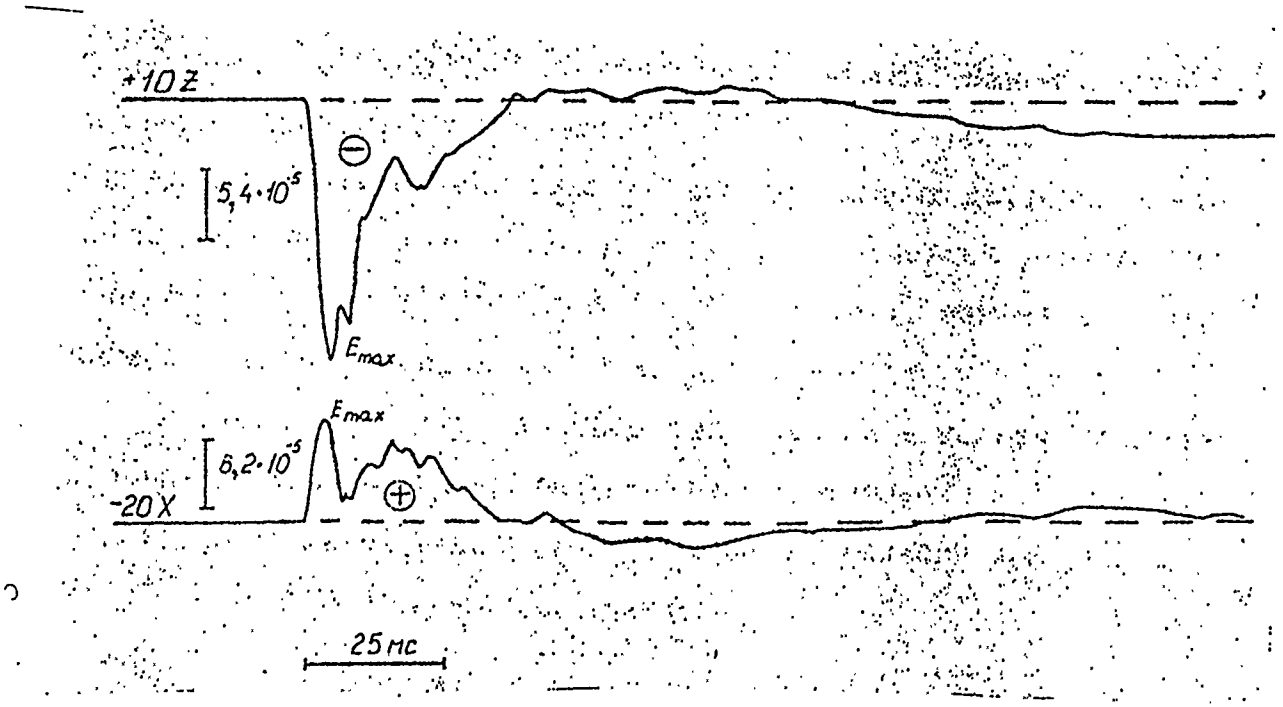

Figure 3.27. Records of the deformations in the compression wave.

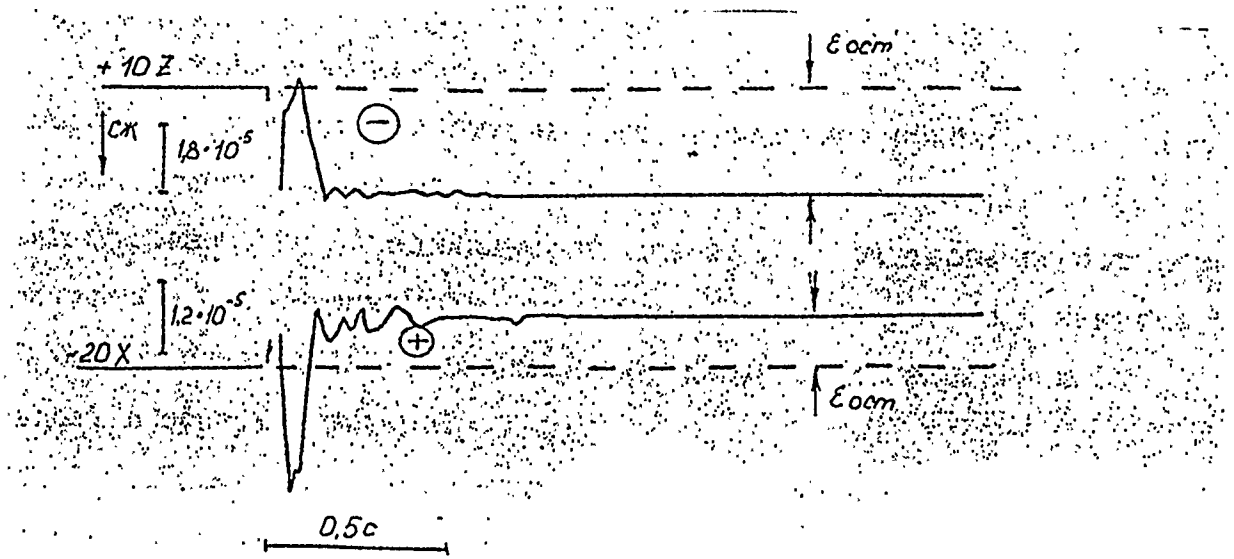

Figure 3.28. Records of the residual deformations.

agreement with the results of the measurements of the appropriate parameters of the velocities and accelerations by means of GIS and EA detectors.

Value of the maximum deformation in Z-component of the wave is $E_z = -1.8\times10^{-4}$ and in X-component - $E_x = 8\times10^{-5}$ relative units (the sign "-" corresponds to the compression). The maximum values of the residual deformations are $E_z = -3\times10^{-5}$ and $E_x = 8\times10^{-6}$ relative units. The typical time, during which the residual deformation becomes the constant, is about 0.3÷0.5 s. In the precision limits of the measurements ($\sim 10^{-6}$ relative units) no variations in the values of the residual deformation were observed in the further registration.

This method was used in the field conditions at the first time and showed a good results as concerns the ratio signal-to-noise, and stability of zero point in the range of the measured values of deformation ($2\times10^{-6} \div 10^{-3}$ relative units).

3.7.1 Residual slopes.

a) Residual slopes in the gallery.

To measure the slopes in the gallery the system of the loading sites for the optical goniometer-quadrant KO-10 was installed. This device allows to measure the slopes with the accuracy of 5÷10''. There were placed 15 loading sites: ten of them were located from the end to the turn of the gallery and five - from the turn to the hermodoor. The angles of the sites slopes were measured into two perpendicular directions - along and across the gallery.

The comparison of the sites slopes before and after the explosion detects the residual angular declination with the same sign along all length of the gallery. The normals to the loading sites declined out of the explosion epicentre with anticlockwise direction in plane.

The declination values are equal:
about 10' in the epicentre area (up to 30 m),
1' in the region of 80 - 100 m,
and 10-30'' in the region of 120-300 m.
The results of these measurements are shown in Table 3.6.

b) Residual deformations on the surface.

To measure the angular displacements on the mountain surface the system of the bench-marks installed on the fault sides was used. As bench-marks we used metallic tubes with 100

Table 3.6. The results of the slope measurements in the gallery.

Number of the loadings sites	Distance from the epicentre	Disposition	Before experiment ° ' ''	After experiment ° ' ''	Slopes value ' ''
19 00°	-20	gallery end	351 45 00	351 46 20	+ 1 20
90°			358 17 40	358 08 30	+ 9 20
18 -"-	0		3 12 40	distructed	
			353 03 45		
17 -"-	5		359 41 00	359 55 40	-14 10
			359 36 30	359 38 50	- 2 20
16 -"-	10	behind R18	8 16 00	8 28 25	-12 25
		from EC	2 58 00	3 12 15	-14 15
15 -"-	31	behind R7	3 14 30	3 24 50	-10 20
		- " -	7 19 50	7 28 50	- 9 00
13 -"-	80	before R9	3 40 20	3 41 10	- 0 50
			359 09 10	359 08 50	+ 0 20
11 -"-	100	before R16	359 52 00	359 52 45	- 0 45
		at the left side	354 39 20	354 40 35	- 1 15
9 -"-	120		5 22 20	5 22 35	- 0 15
			359 54 30	359 54 50	- 0 20
8 -"-	127	behind R12	0 54 40	0 54 50	- 0 10
			359 52 10	359 52 10	0
7 -"-	137	before the turn	357 48 48	357 48 30	+ 0 18
			348 19 30	348 19 00	+ 0 30
6 -"-	155	after the turn	358 44 20	358 44 40	- 0 20
			357 06 10	357 06 00	+ 0 10
5 -"-	190	behind R10	0 56 25	0 56 30	- 0 05
			353 29 45	353 30 00	- 0 15
3 -"-	240	behind R8	357 07 10	357 06 55	+ 0 15
			0 16 00	0 16 30	- 0 30
2 -"-	255	after R7	357 20 40	357 20 50	- 0 10
		before R6	357 52 30	357 52 25	+ 0 5
0 -"-	300	near hermodoor	356 25 50	356 26 20	- 0 30
			357 37 00	357 37 30	- 0 30

mm in diameter located at 2 ÷ 4 m in depth. They were placed in the one direction at distances of 50 ÷ 300 m in both sides from the charge centre. The sites with the angles of the slopes, measured by the quadrant K0-10, were installed on these bench-marks.

The reliable results were obtained only from 5 of 11 bench-marks, because the other were covered or damaged by the stone scattering from the crater. From the results of the measurements it was founded, that the bench-marks located at

distances of 80 ÷ 100 m from the charge centre were inclined to the explosion at an angle of 1 ÷ 5'. The bench-mark located at 230 ÷ 280 m were inclined at 30''÷ 1' to the explosion.

The destruction of the mountain slopes with the creation of the landslides and rock avalanches due to the explosion didn't take place around the crater. The main mass of the rock pile was located on the relatively gentle part of the top, where the slope of the surface reached 5-10°. There were not observed any creations of the talus too. It is possible to note only the rolling down of some stones at the scattering border in the direction of the more steep northern slope of the mountain. The mass of this stone fall was negligible.

3.7.2 Measurements of the linear displacements in the gallery by means of the tape deformographs.

To measure the deformations in the gallery at the geological faults the tape resistive deformographs with the base of 4 ÷ 10 m were used. The accuracy of the measurements for these deformographs is 10^{-5}. Five deformographs covered the fault at distances of 31, 52, 80, 100, and 107 meters from the epicentre.

The records of the signals from all deformographs were obtained as a result of the experiment. All detectors registered the passing of the epicentral wave. The greatest residual displacement of about 0.7 m were recorded by means of the deformograph N3 installed on the fault N17 (80 m). This displacement corresponds to the fault compression on the base of -7.15 m and the deformation of about 10^{-4}.

Other detectors registered a small displacements with value of 0.1 mm.

0.5 sec after the passing of the epicentral wave there were observed the falls of some stones on the tapes of the deformographs N2 and N4. After that, the detectors turned into the initial position. All information about the deformographs location and the results of these observations are presented in the Table 3.7.

The oscillogram of the signal from the deformograph records are shown at the Fig. 3.29.

More detail treatment and analysis of the experimental data of the displacements in the gallery and on the surface will be presented in the concluding account.

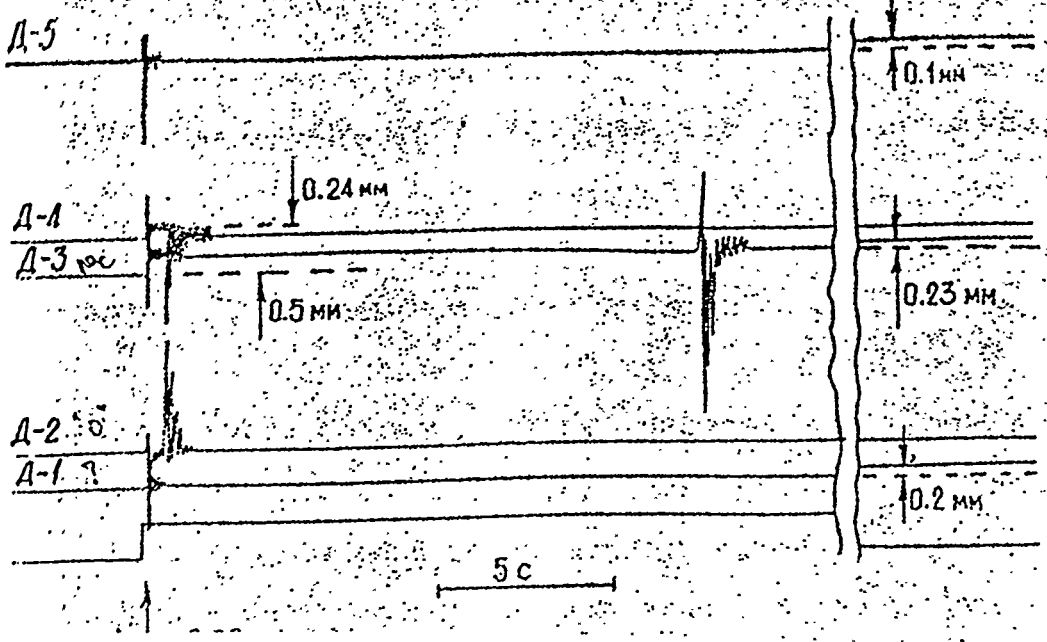

Figure 3.29. Records from the tape deformograph.

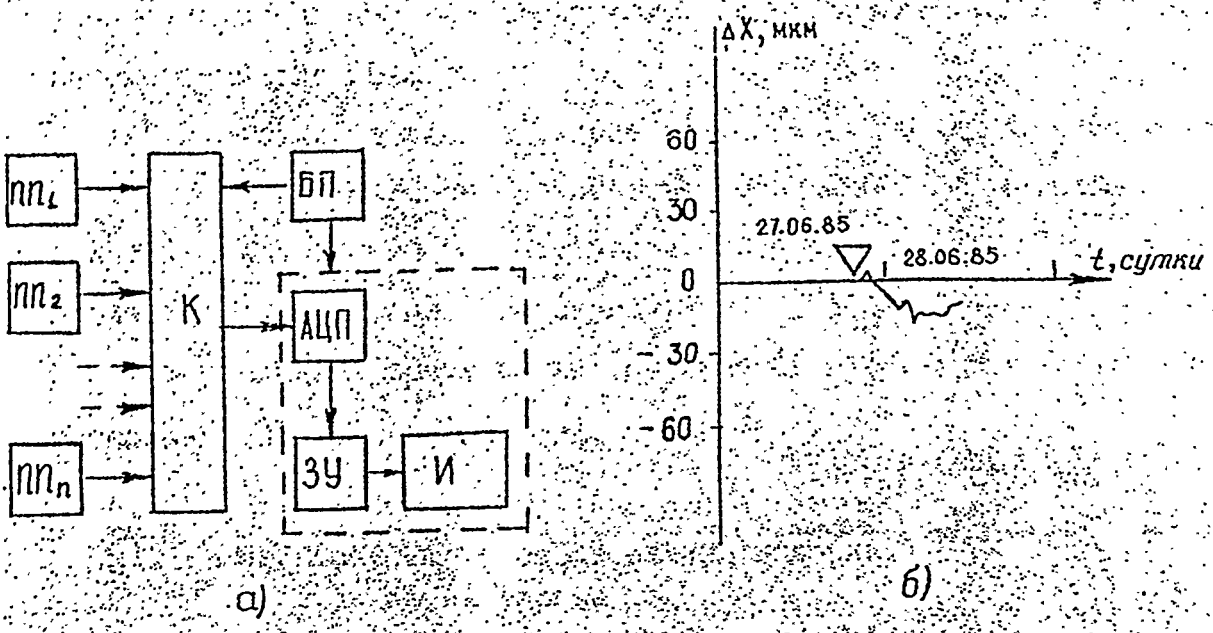

Figure 3.30. Block-scheme (a) and record (b) of the string deformograph.

Table 3.7. The results of the linear displacement measurements.

Number	Detector number	Disposition at crackness zone	Deformo-graph base m	Distance from epi-centre, m	Linear displace-ment, mm
1	D_1	R7	6.9	31	-0.2
2	D_2	crackness zone	8.6	52	0
3	D_3	R17	7.15	80	+0.73
4	D_4	R16	3.8	107	+0.24
5	D_5	R10	1.58	100	+0.1

3.7.3. Measurement of the deformation in the gallery by means of the string deformometrs with the digital recorder.

To measure the residual deformations the string deformograph was used too. The registration of the detector reading was realized by means of the multichannel digital recorder with the electronic digital memory. The block-scheme of this recorder is represented at Fig. 3.30, where PT - is the primary transformers, C - commutator, and I - the scheme of the indication.

The time interval between the registration was equal to 1 hour. The registration of the information was realized by means of the indication plate, where the reading number and its value were indicated.

The recorder was placed in the gallery at a distance of 80 m from the epicentre. The results of the measurement are shown at Fig. 3.30, the detector base was 5 m. After the moment of the explosion, marked at Fig. 3.30, the detector readings corresponded to the relative displacement of the bench-marks at 18 mkm, that correspond to the deformations of about 3.5×10^{-6}. As the system allows to measure the deformations of 10^{-5} and greater with a good accuracy, the registered deformation is commensurable with the noise level of the device.

3.7.4. The seismic emission from the rock massif.

The registration of the seismic emission after the explosion was realized by means of three-component seismic station, consisted of seismometers SM-3, which are located at a distance of 2800 meters from the explosion, with the amplifier PPU-M and registered oscillograph OSP-2M with the galvanometers GB-SH-5S.

The registration was made in the frequency band of 0.5 ÷ 10 Hz. In the time interval to 32 sec from the explosion the amplification was equal to 35000, and in the time interval from 32 sec to 27 min 50 sec after the explosion it was 350000. The cassette was changed from 210 to 320 sec.

There were no appreciable signals of the seismic emission in this time interval.

3.7.5. Results of the gallery investigations after the explosion.

There were the falls of some stones from the roof and walls of the gallery at distances up to 70 m from the epicentre. The mass velocities in the epicentral wave below the explosion centre in the massif at the gallery level were equal to 0.4 m/s. The intensive rock fall was observed in the range of ±20 m from the epicentral point (Fig. 3.31).

The total volume of the fall was about 30 m^3. The form and sizes of the rock fragments (with volume smaller 0.3 m^3) were conditioned by the developed chaotic system of the cracks in the massif heart.

The safety of the cement guards, located on the all tectonic cracks, uncovered by the gallery, and the comparision of the photo materials of the left side of the excavation before and after the explosion allow to conclude that there are not visible signs of the displacements on the gallery level.

3.7.6. The hydrogeological observation.

When we observed the underground water regime, the maximum growth of the level (+25 cm) was registered in the well N°4017, located at the distance of 310 m in the southern direction from the explosion centre. In the other wells at the distances up to 2.5 km it was observed the growth of 5-10 cm with the accuracy of the measurement by hand means of ±5 cm.

3.7.7 Residual angular and linear displacements and deformations in the gallery and on the massif surface.

To reveal the linear and angular displacements the investigations along the gallery and on the massif surface were realized.

Two groups of the measurements were realized in the experiment:

- the measurement of the angular residual displacements in

the gallery and on the surface, and
- the measurements of the linear residual deformations in the gallery.

To study the angular displacement two types of inclinometers were used:
- the optical inclinometers KO-10KO-10 were used to measure the displacements before and after the explosion, and
- the electrolytic inclinometer was used to measure the displacements during the explosion.

a) Measurement of the slopes by means of the optical inclinometer in the gallery.

To measure the residual slopes in the gallery the optical quadrants KO-10 were used. The system of the measuring sites was installed in the gallery taking into account due regard for the geological structure of this massif.

Fifteen sites were installed in the gallery in the experiment. The location of these sites are shown at the scheme at the Fig. 3.33. The sites were placed on the walls of the gallery. To determine the recurrence of the measurement results and to control the work of the inclinometer with the site the estimation of the measurement accuracy was made in the real conditions of the work.

Some site was chosen as a control (later it was used as a standard), and the reading stability was determined by three reiterations of the measuring method.

The results of the three-days measurements are shown in Table 3.8. The most likely value of the measurements has been determined by three methods, in each of them the average value from three readings was used. The mean square error of the one measurement was:

$\bar{m}_1 = \pm 10.03''$; $\bar{m}_2 = \pm 5.3''$; $\bar{m}_3 = \pm 8.5''$.

The total mean square error was:

$M_1 = \pm 5.8''$; $M_2 = \pm 2.9$; $M_3 = \pm 4.9''$;

The analysis of the results of the control measurements allows to conclude that the recurrence of the measurements results are rather stable with the error no greater than the device accuracy.

As a result of the measurements of the sites positions before and after the experiment the angular residual slopes were determined along the gallery as well as across it.

Table 3.8. Results of the observations of the of the inclinometer measurements recurrence.

	24.06.85			25.06.85			26.06.85		
	α ° ′ ″	$\delta = \alpha - \alpha_{av}$	δ^2	α ° ′ ″	$\delta = \alpha - \alpha_{av}$	δ^2	α ° ′ ″	$\delta = \alpha - \alpha_{av}$	δ^2
1	6 39 34	-8.6	74	6 40 00	-5.0	25	6 40 08	+01	1
2	6 39 54	+11.4	130	6 40 10	+5.0	25	6 40 15	+8	64
3	6 39 40	-2.16	4.8	6 40 05	0.00	0	6 39 58	-9	81
α_{av}	6 39 42.6			6 40 05			6 40 07		
$\Sigma\delta^2$			208.8			50			146
m			±10.03			±5			±8.5
M			±5.8			±2.9			±4.9

where $\alpha_{av} = \frac{\alpha_1 + \alpha_2 + \alpha_3}{3}$ $m = \pm \sqrt{\frac{\Sigma\delta^2}{n-1}}$, and $M = \pm \frac{m}{\sqrt{n}}$

The Table 3.9 presents the results of the measurement, and the Fig. 3.32 presents the graph of the residual slopes after the experiment. After the experiment the values of the slopes were equal to:

- 10 ÷ 14' along the gallery and 9 ÷ 14' across it at distances of +5, +10, and +30 m in the epicentral region;
- 0'45'' ÷ 0'50'' along the gallery and 0'20'' ÷ 1'15'' across it at distances of +80 and +100 m;
- at distances of 120 ÷ 300 m the slopes were in the range of 10'' ÷ 30'', but six measurements give the values smaller 10'', that is in the range of measurements accuracy;

The measurements on the same sites were made an year later. As it is shown in Table 3.9 (colomn 7) the values of the angles are the same in the near-mouth zone and up to the level of 127 m. At a distances of 10, 30, 100 and 120 m there are some deflections from the initial results at the values of 1'÷2'30''.

b) Measurement of the slopes by means of the electrolytic inclinometer.

To decrease the time interval during the measurements after the explosion and to increase the accuracy of the measurements

Table 3.9. The results of the measurements of the slopes in the gallery after the experiment.

Along 0° Across 90°	Distance from the epicentre m	N	Before the experiment, α_1 °	After the experiment, α_2 °	$\delta=\alpha_1-\alpha_2$, ,,	An year later α_3 , ,,	After 8 tons.	$\delta_2=\alpha_2-\alpha_3$	$\delta_2=\alpha_2-\alpha_3$
1	2	3	4	5	6	7	8	9	10
00 90	-20	19	351 45 00 358 17 40	351 46 20 358 08 30	-01 20 +09 10	42 15 08 10	42 10 08 05		00 05 00 05
00 90	+5	17	359 41 00 359 36 30	359 55 40 359 38 50	-14 10 -02 20	54 40 37 25		+01 00 +01 25	
00 90	+10	16	8 16 00 2 58 00	8 28 25 3 12 15	-12 25 -14 15	26 50 13 10		+01 25 -00 55	
00 90	+31	15	3 14 30 7 19 50	24 50 28 50	-10 20 -9 00	23 10 26 20		+01 40 +02 30	
00 90	+80	13	3 40 20 359 09 10	41 10 08 50	-0 50 +0 20	39 50 07 20	39 50 07 10	-01 20 +01 30	00 00 00 10
00 90	+100	11	359 52 00 354 39 20	52 45 40 35	-0 45 -0 15	52 50 38 30	52 00 38 20	-00 05 +02 05	00 50 00 10
00 90	+120	9	5 22 20 359 54 30	22 35 54 50	-0 15 -0 20	21 40 26 30	21 35 26 20	+00 55 -01 40	00 05 00 10
00 90	+127	8	0 54 40 359 52 10	54 40 52 10	0 00 0 00	53 20 51 10	53 45 50 00	+01 30 +01 00	-00 25 01 10

00 90	+137	7	357 48 48 348 19 30	48 30 19 00	+0 18 +0 30	47 10 17 40	47 35 17 40	+01 20 +01 20	-00 25 00 00
00 90	+155	6	358 44 20 357 06 10	44 40 06 00	-0 20 +0 10	43 45 04 35	43 50 04 40	+00 55 +01 25	-00 09 -00 05
00 90	+190	5	0 56 25 353 29 45	56 30 30 00	-0 05 -0 15	57 30 25 50		-01 00	
00 90	+240	3	357 07 10 0 16 00	06 55 16 30	+0 15 +0 30				
00 90	+255	2	357 20 40 357 52 30	20 50 52 25	-0 10 +0 05	19 55 57 30			
00 90	+300	0	356 25 50 357 37 00	26 20 37 30	-0 30 -0 30	25 10 36 50			

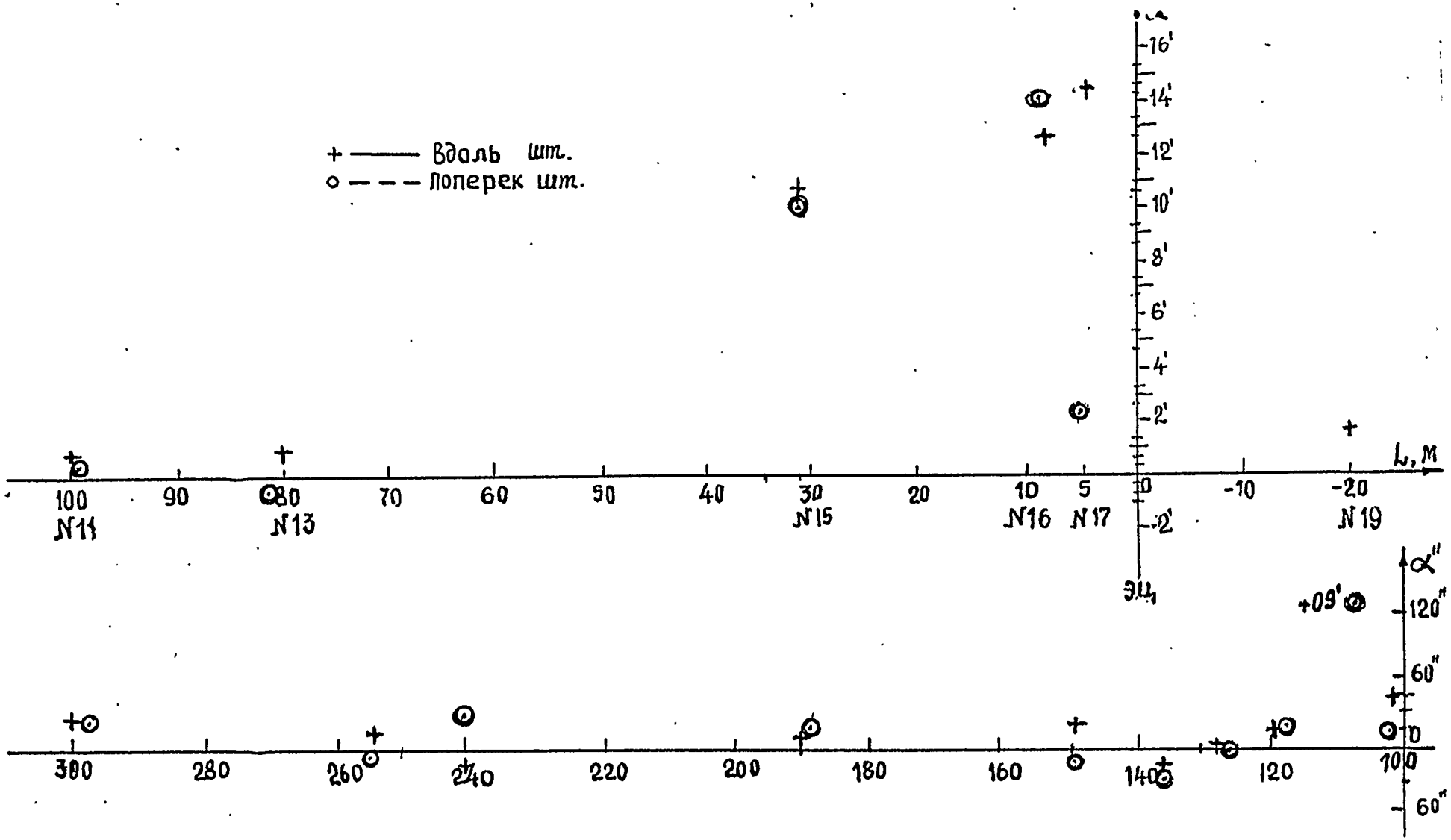

Figure 3.32. Graphs of the residual slopes after the experiment
+ - along the gallery
o - across the gallery

the inclinometer IMUS-1 was constructed on the base of the use of the electrolytic level. The record of the signal received during the action are shown at Fig. 3.31. The maximum signals was about ~ 3'. The time of the inclinometer shooting is equal to 1 ÷ 2 s. After the device shooting the residual slope is equal to 10'', that is in the range of the device accuracy.

The work with the electrolytic inclinometer showed the perspective of its using in study of the slopes in the rock massif due to the action of the seismoexplosive wave.

c) Residual slopes on the massif surface.

To measure the angular displacements on the massif surface the system of the bench-mark was installed on the borders of the geological faults. These sites were placed in the one direction at a distances of 80 ÷ 300 m in both sides from the centre. The slopes of the sites were measured by the quadrant RJ-10. The reliable results were obtained from 5 ÷ 7 of 11 bench-marks. Other bench-marks were covered or damaged by the stone scattering from the crater.

From the measurements it was founded, that the bench-marks had the slopes with different signs in range from 1' 45'' to 45' 50''. Table 3.10 represents the data of the sites location and results of the measurements. It is possible to note, that the large slopes at distances of 80 ÷ 100 m might be connected with the borders of the concentric faults around the central part of the massif, situated at these distances.

d) The residual linear displacements

The residual linear displacements were observed along the borders of the steep falling faults by means of the special bench-marks, installed in the gallery, and measurements of the end part of the gallery by the light range-finder. The vertical displacements were measured by the leveling along all gallery length.

To measure the displacements in the gallery the character areas with the geological faults at a distances of 31, 52, 80, 100, and 107 m were chosen. The deformographs DMP-R with the bases of 8.6, 7.15, 6.9, 3.8, and 1.58 m were used in these measurements. The height of the apparatus was 1.5 ÷ 2 m from the soil level in the gallery. The registration of the signals was realized by means of the oscillograph N-117, installed in the equipment construction. The calibration of the deformographs was made before the measurements by the change of its base at some fixed linear value.

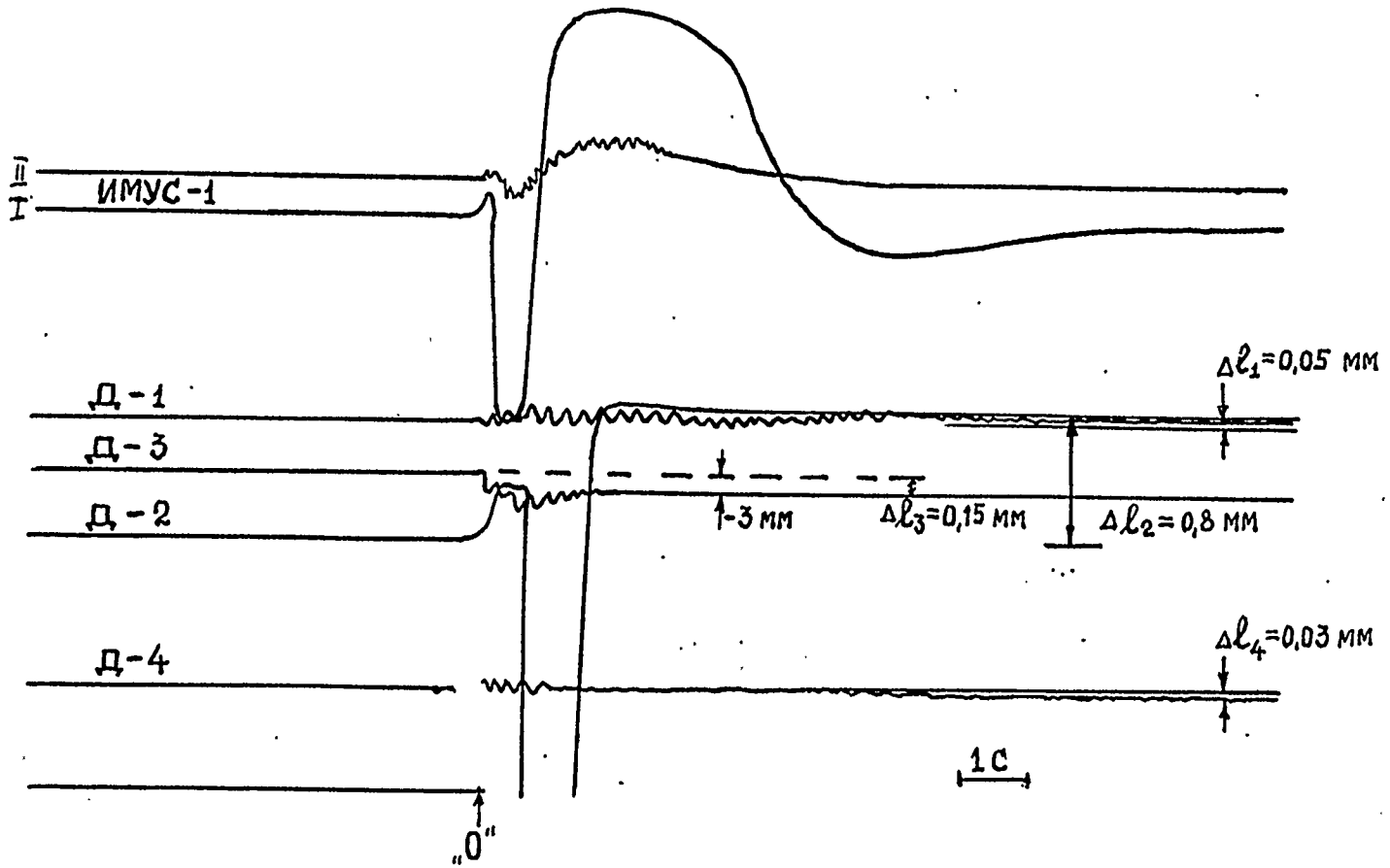

Figure 3.33. Records from the tape deformographs and inclinometer IMUS-1.

Table 3.10. Slopes of the measuring sites on the massif surface.

Number of the site	Number of the bench-mark	Azimuth from the explosion centre, °	Distance from the centre to the bench-mark m	Residual slopes after the experiment	Slopes directions
1	6	0	55		to centre
2	7	0	80	-00°01'50"	from centre
3	8	0	85		to centre
4	9	0	160		from centre
5	10	0	230	+00°16'10"	to centre
6	1	180	140	-00°45'50"	from centre
7	II-a	180	200		to centre
8	II-b	180	220	+00°00'30"	to centre
9	III	180	280	+00°01'30"	to centre

The records of the signals from all five deformographs were received after the experiment. All detectors fixed the passing of the wave. The deformograph N3, installed on the fault N17 (80 m), registered the greatest residual displacement with value ~ 0.7 mm on the base of 7.15 m, that corresponds to the deformation of about 10^{-4}.

Other detector fixed a small displacements of about 0.1 mm. 0.5 sec after the passing of the epicentral wave, there were observed the falls of some stones on the tapes of the deformographs N2 and N4. After that the detectors turned into the initial state.

The information about the deformographs location and the results of the observations are presented in Table 3.11. The signals oscillograms are shown at Fig. 3.34. The accuracy of the linear measurements for all device was equal to $\Delta l = \pm 0.1$ mm. For the base of 10 m it gives the relative error of $\pm 10^{-5}$. Since during the measurements the temperature in the gallery changed not greater than 0.5°C, it is possible to think that this measuring accuracy was realized completely.

All deformographs were installed across the steeply falling faults. The analysis of the tape deformographs readings allows to conclude that the value of the displacements, to a greater degree, depends on the character of the disturbances zone rather than the distances from the explosion epicentre.

So, the deformographs D-2 and D-3, installed in zones of the more greater disturbances, detected the largest relative displacements in comparison with the displacements, registered

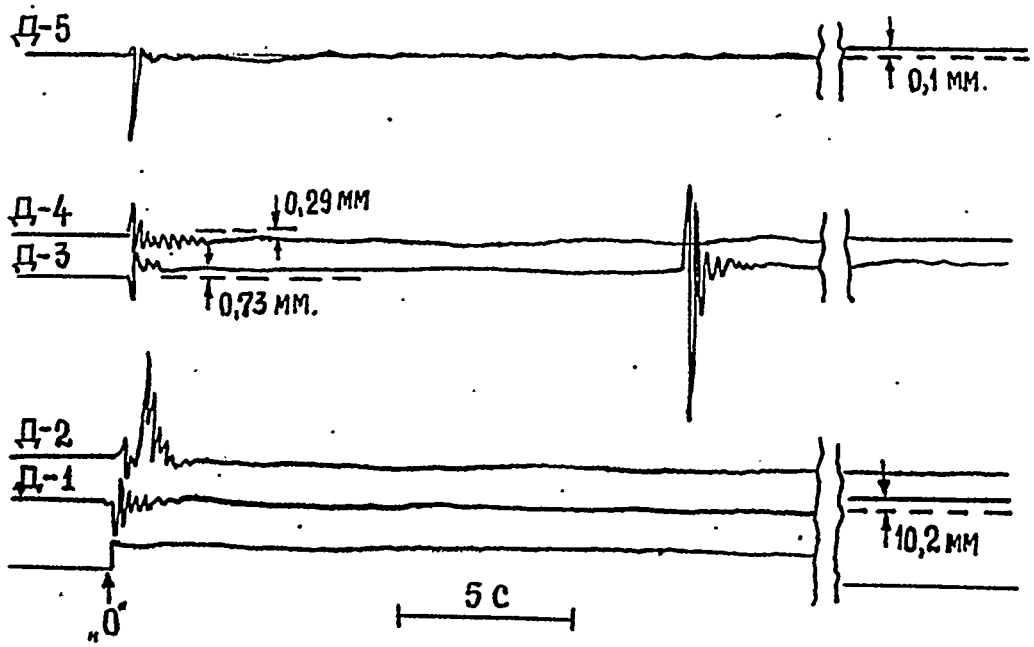

Figure 3.34. Signal oscillograms.

Table 3.11. The results of the measurements of the linear displacements on the fixed bases.

Number	Detector number	Fault number	Distance from the epicentre m	Detector base, m	Linear displacement mm	Deformation $\Delta l/l$	Displacement description
1	D-1 (101)	F-7	31	6.9	-0.2	-2.9×10^{-5}	compression
2	D-2 (103)	-	52	8.6	0.0	0.0	-
3	D-3 (105)	F-17	80	7.15	+0.73	1.1×10^{-4}	tension
4	D-4 (106)	F-16	107	3.8	+0.24	1.63×10^{-5}	tension
5	D-5	F-10	120	1.58	+0.1	0.63×10^{-4}	tension

by the deformograph D-1, which was the nearest to the central zone, but installed on the area of the disturbances with smaller width.

The angle of the wave-front incidence to the fault plane plays a noticeable part too. The tracks of the animation were observed on the flat falling fault at a level of 60 m, where the relative displacements evidently were greater than the displacements, detected on the steep falling faults.

e) Vertical residual displacements

The measurements of the residual vertical displacements were made into the gallery too. The control of the vertical displacements was realized by means of the goniometrical levelling of the metal bench-marks, fastened on the roof along the gallery axis and measuring sites, installed on the both sides of the gallery at a level of about 1.5 m from the soil.

High-altitude notes of the bench-marks and measuring sites were obtained from the closed levelling motion of the class III from the results of two independent measurements before and after the experiment. The error of the definition of the bench-marks levels was not greater than the maximum of the permissible error of the measurements for this accuracy class, received from the next formula:

$$\delta_n = \pm \sqrt{L(km)} = \pm 10\times0.64 \text{ mm} = 0.64 \text{ mm}$$

The measurement error at each station was not greater than ± 0.65 mm.

The results of the measurements of the bench-marks on the roof are presented in Table 3.12 and the measurements on the sites are presented in Table 3.13. The location of the measuring sites in the gallery is shown at the scheme at the Fig. 3.35.

Table 3.12 The results of the observations of the vertical displacements on the gallery roof.

Number	Distance along the gallery, m	Displacement after the experiment, mm	Total displace-ment, mm	Comments
1	450	+1	–	Gallery mouth
2	400	0	–	
3	350	+4	+4	
4	300	+2	+1	hermowall
5	240	+8	+9	
6	200	+6	+8	
7	155	+2	+5	gallery turn
8	150	–	–	
9	100	+5	+9	
10	50	–	–	
11	0	–	–	epicentre

f) The residual soil deformations under the explosion centre.

To receive the information about the stability of the vertical rock excavation with filler under the high dynamic loading the well G-2 under the explosion centre was made monolithic by the special filler. Marked metal rings were installed at 35 levels from a depth of 5.63 m with step of 25 cm. Above the indicating rings, at the depth range from 2.63 m to 5.63 m, 12 blocks with height of 25 cm were fixed in the well G-2. Each block had an loading details into it, which were used as a depth indicators.

After the explosion the installed details from the initial levels from 2.63 to 5.63 m were founded at the crater bottom at the section of 1 meter in length, i.e. the part of the well with length of 3 m was compressed more than into tree times.

The loading details were uncovered up to level N12, which was transferred from the depth of 8.4 m to the depth of 9 m.

Table 3.13. The results of the observations of the vertical displacements on the gallery walls.

Number	Bench-mark number	Distance from the epicentre to the bench-mark, m	Vertical displace-ment after the expe-riment, mm	Total displa-cement, mm	Comments
1	0	300	+1	+4	
2	2	255	0	+2	
3	3	210	-2	+3	
4	5	190	+1	+3	
5	6	155	+1	+5	gallery turn
6	7	137	+2	+8	
7	8	127	+2	+10	
8	IX	120	-	-	
9	9	115	+2	+10	
10	11	100	-6	+1.5	
11	XI	100	-	-	
12	XXXI	85	-	-	
13	XXX	80	-	-	
14	13	80	-1	+5	
15	XXVIII	65	-	-	
16	XXIX	65	-	-	
17	XXVI	55	-	-	
18	XXVII	55	-	-	
19	XV	35	-	-	
20	XXV	31	-	-	
21	XXIV	25	-	-	
22	16	10	+2	+11	
23	17	2	+2	-	centre of
24	18	-2	+9	+16	the well
25	XXIII	-5	-	-	
26	XXII	-13	-	-	
27	XXI	-15	-	-	
28	XX	-20	-	-	gallery end
29	19	-20	+3	+12	gallery end
30	I	5	-	-	N-1
31	II	10	-	-	near N-1

These data might be compared with the simple model of the crater creation, known in U.S.A. as a Z-model. In this model the displacements under the explosion centre are described by the follow formula:

$$Z_1 = (h^{n+1} + Z_0^{n+1})^{1/(n+1)} \qquad (3.3)$$

where Z_0 and Z_1 - the initial and the ultimate depth of the observed particle of the soil, correspondingly, and h is the

crater depth.

If the crater depth is h = 8 m, than from (3.3) with n = 3, that is the most likely value, a particle from the level of 2.63 m must be transferred to the level of 8.02 m, from the level of 5.63 m - to the level of 8.45 m and a particle from the level of 8.4 m must be transferred to the level of 9.7 m. So, from this model, the total vertical dimension of the upper column of the soil must be reduced from 3 m to 0.5 m, i.e. approximately into six times.

After the experiment the loading details from the upper column were transferred roughly at 1.5 m from the centre and were founded on the subhorizontal part of the bottom with 1 m in length. So, we can observe the qualitative agreement of these results and model estimation: the soil under the explosion centre is not threw out, but it is pressed in the down vertical direction, its initial thickness is reduced in a few times because of the non-elastic deformations.

The observed column shortening from the level of 2.6 m to the level of 5.2 m into tree times is the minimum estimation of the vertical compression, since the ultimate height of the column is estimated by the horizontal location of the loading details.

The registered displacement of the loading detail N12 at a distance of about 0.5 m (from the level of 8.38 m to 8.9 m) roughly in 3.5 times smaller than the estimation received from the formula (3.3) $\Delta Z \sim 1.3$ m. One of the causes of this discrepancy consists in the proximity of the model for such little displacements.

However, it is necessary to point out the possibility of the recurrent motion of the crater bottom. The fact, that this recurrent motion arises in the massif under the crater bottom, is observed on the oscillograms of the mass velocity under the explosion centre. Then the value of the recurrent motion of the crater bottom might be estimated as 0.8 m.

So, it is possible to conclude that the simple model of the crater creation (Z-model) might be used for a qualitative estimations of the soil deformations in the borders of the created crater.

4. MECHANICAL EFFECT OF THE UNDERGROUND NUCLEAR EXPLOSION, CARRIED OUT IN APRIL 15, 1984.

4.1 Experiment performance

The experiment in the gallery N° 190 was realized in April 15, 1984. The object was the complex of the underground constructions for the group test of two charges. The gallery length from the portal to the face was equal to 1290 m and azimuth of the expansion was 195°. The rock part of the object consisted of two linear located zero boxes (ZB) and half-annular excavations MSS, corresponding them (the method of the soil sphere).

Zero boxes had spherical forms. ZB-2 was located at a distance of 300 m from ZB-1. The charges powers were equal to 54.6±6 kt (ZB-1) and 3.16±0.5 kt (ZB-2), correspondingly. The depth by LMR (line of the minimum resistance) was equal to 277 m for the first charge and 187 m for the second. Granites with gas content of 0.5% by T=1000°C were the main rock type in the site of the charge location.

The stemming complex of the gallery included four sections:

- the first stemming part (PQ (piquet) 294-353 m) consisted of the concrete plug (PQ 294-297 m), the plug from the heavy concrete with density of 2.8 g/cm^3.(PQ 297-304 m), the concrete plug (PQ 304-307 m), the section of the detritus filler (PQ 307-350 m), and the concrete wedge (PQ 350-353 m);

- the second stemming part (PQ 440-452 m) consisted of the concrete wedge and the plug (PQ 440-445 m), the part of the separate concrete (PQ 445-447 m), and the concrete wedge (PQ 447-452 m);

- the third and the fourth stemming parts (hermowalls) were constructed as two concrete wedges, each of them with 3 m in length, and were located at PQ 620 m and PQ 750 m, correspondingly.

The light pipes with diameters of 168 and 351 mm were laid in the body of the first stemming part and further, from ZB-2 up to the portal. The radiation from ZB-1 wasn't took out on the pre-mouth area. The hermotunnels with diameter of 900 mm were laid through both hermowalls.

4.2 Geological characteristics of the massif

The gallery N° 190 was driven in the south-western part of the rock massif. Its length from the portal to the face was

equal to 1290 m.

The scheme of the tectonic faults location (the structure-geological cross section) is shown at Fig. 4.1.

The object was located under the north-eastern slope of the top with the absolute level of 946.0 m. The site has a structure-denudated low-mountainous relief, the absolute levels of the surface change from 620 to 916 m. The mountain slopes are indented by numerous hollows, usually connected with the tectonic breaches with angles of thalwegs up to 35°.

The southern slope is covered by the new-formed talus and the northern slope represents low, partially destroyed juts of the native granites. The northern and the southern parts are divided by faults with the north-western spreading. In the northern part the slopes are more gentle and hollows have a great depth of the cut (to 30 m). These hollows have a steep (to 60°) sides with uncovered granites. Taluses are placed on the base of these precipices.

The gallery portal is located at the point of the crossing of the hollows of sub-latitudinal and meridional directions. The acidic intrusive rocks of the Upper Paleozoic age (γPz_3), intruded by the dikes of the granite-porphyries ($\gamma\pi Pz_3$), were uncovered by the rock excavation. The intrusive formation are represented by the light grey granites with tins of red with massive average-granual structure. The gentle slopes are covered by the turf, sandy loam, rotten stones, and small detritus.

After the explosions at the nearest objects the biggest part of the surface is covered by new-formed taluses on the steep parts of the massif. The taluses are composed from large-stone material (the stone sizes are 7-10 m^3) and, sometimes, small-stone material. The large-stones border the taluses and lie in their base up to the hollows bottoms. The taluses are the result of the rock structures destructions.

The rock crackness in the gallery might be divided in three genetic types. The cracks of the primary separates are well observed in the granites, and the circular diagrams with calculation of the crack number in the structure-tectonic blocks were plotted on the base of them (Fig. 4.1).

The gallery uncovered 12 tectonic ruptures. The fault at PQ 775 m is the biggest of them, it is characterized by the thick zone of the influence of two dislocater and large length. The fault is the boundary between two structure-tectonic blocks of order II (STBP). The bedding elements of this fault is the next: the azimuth of the incidence is 200-210°, the angle of the incidence is 80° and the thickness is equal to 20-30 cm. It is

Figure 4.1.

Schematic engeneering and geological map of the object N°190

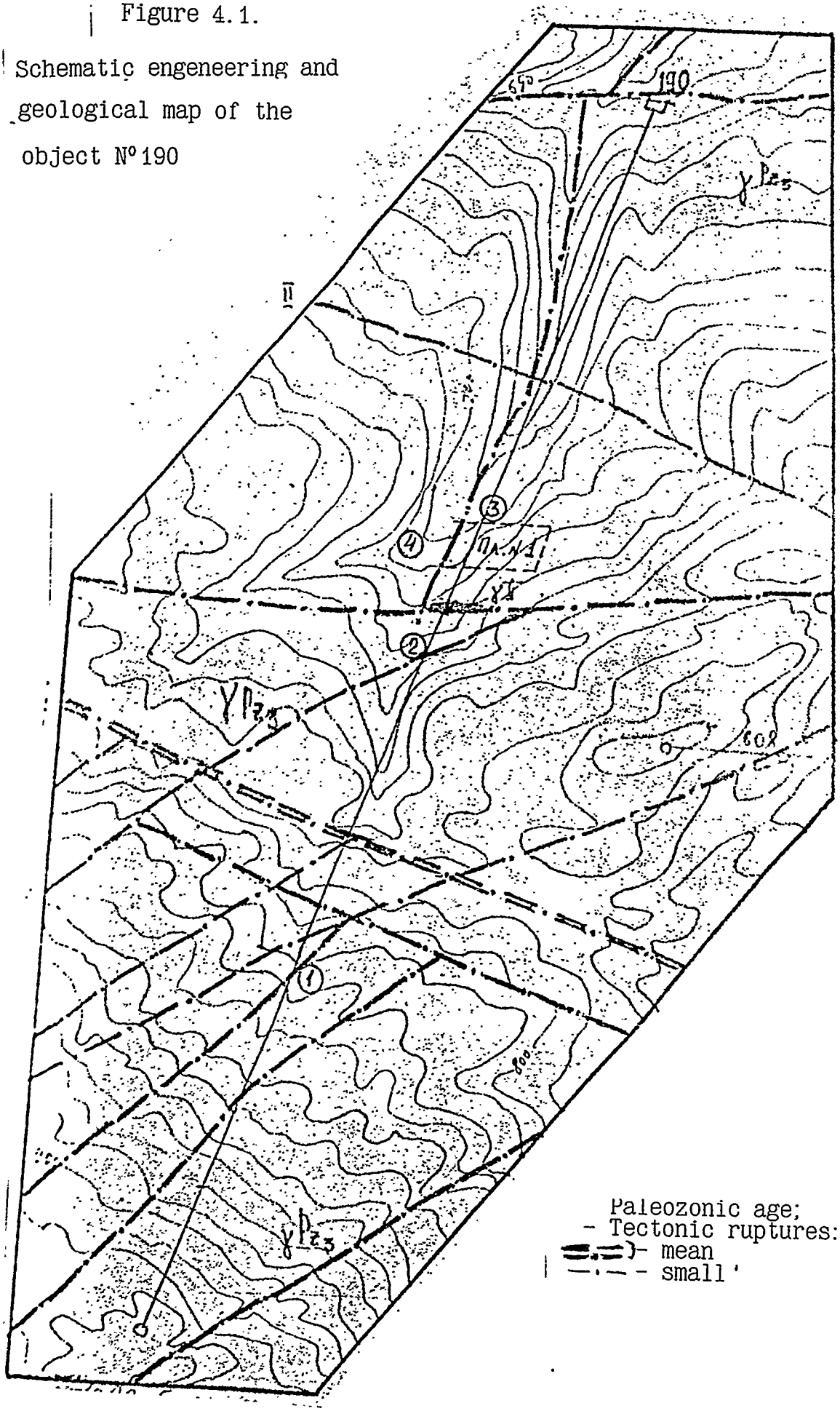

characterized by the intensive crackness of the enclosing rocks, wet clay gouge and dripping. Small tectonic cracks usually pass parallel to the tectonic faults.

The structure of the southern slope is more complex: there are not sub-latitudinal and gentle ruptures.

Zones of the dislocater, the influence of the small ruptures in the northern and southern blocks are identical, the spatial orientation of the cracks in the basic systems practically are the same.

The crackness modulus in the southern block is in 1.5 times greater than in the northern in the northern, but the coefficient of the porosity, connected with cracks, in the southern block is in 3 times less than this coefficient in the northern block.

The structure-tectonic blocks of order II are composed of the smaller blocks of order III. The number of the cracks of order III per one linear meter of the excavation changes from 1.35 to 3.2.

The form and sizes of the elementary blocks depend on the crackness. There are the checked fractures as the most frequent on the daily surface. In the range from 505 to 945.5 m along the gallery it is observed the horizontal bedding, because the cracks bed with the angles of incidence from 0 to 3°. The investigated fragment and instrument construction are located in this range. The cracks spatial positions in systems on the surface and at the gallery level are comparable (the observed deviations are only insignificant errors of the measurements by compass due to metal presence).

The physico-mechanical characteristics were determined during the experiment with 50 samples, 40 of which were investigated in two perpendicular directions.

The comparison of the parameters by the choice with help of Student's and Fisher's criteria shows that:

- physical and mechanical characteristics of the rock on the surface and in the gallery are practically identical;
- elastic characteristics of the eroded and invariable rocks are different on the base of Fisher's criterion and depend on the microcrackness (Student's criterion gives a significant difference for S-wave velocities in the noneroded rocks);
- there are some insignificant, but stable changes of the

average values of the properties, determined in perpendicular directions;

- crushing strength in the direction of the microcracks is less than in the perpendicular direction;

- the changes of P-wave and S-wave velocities are the same.

In the investigated fragment some zones of the low velocities were marked out on the base of the geophysical data. The first zone is connected with small tectonic rupture with north-western spreading, and the second zone is connected with quartz-sulphide lode (the lode thickness is about 3.0 m) crossing the excavation at an acute angle. The lode is composed of pyrites, chalcopyrites, sphalerites, and galena.

Besides thin quartz loads, there are dikes of the quartz porphyries in the interval of 530.5-533.5 m.

There are the wall wetting and weak dripping at some parts of the excavation, connected with tectonic ruptures and sections with high crackness.

4.3 The development of the external phenomena

The registration of the explosion action at the surface was realized at two optical stations. The first station, located at a distance of 1560 m from ZB, was equipped by two cine-cameras AKS-4m. The lenses of 85 mm in diameter were installed on these cameras, the filming velocity was about 40 stills per second. The camera switching on was made by automatic signal.

The second optical station was located at a distance of about 3 km. There was the cine-camera AKS-4m with the lenses of 125 mm in diameter and filming velocity of 30 stills per second at this station. The switching on of the camera was made by hands 5 seconds before the explosion. Besides using of these apparatus the slope surface was photographed before and after the explosion by cine-camera AFA-BAR.

The most intensive soil motion was observed in the upper part of the slope at a distance of ___ from the point of LMR IB (intermediate box) outlet to ZB epicentre. The treatment of stills allowed to plot the graph of the height of the dome lifting at ZB centre region with respect to the time. This dependence is shown at Fig. 4.2 by a solid line. The absence of the measurements in the time interval from 0.28 to 0.42 s is connected with the arrival of the wave to the optical station, and, so, with the epicentre image oversteps the limits of the still.

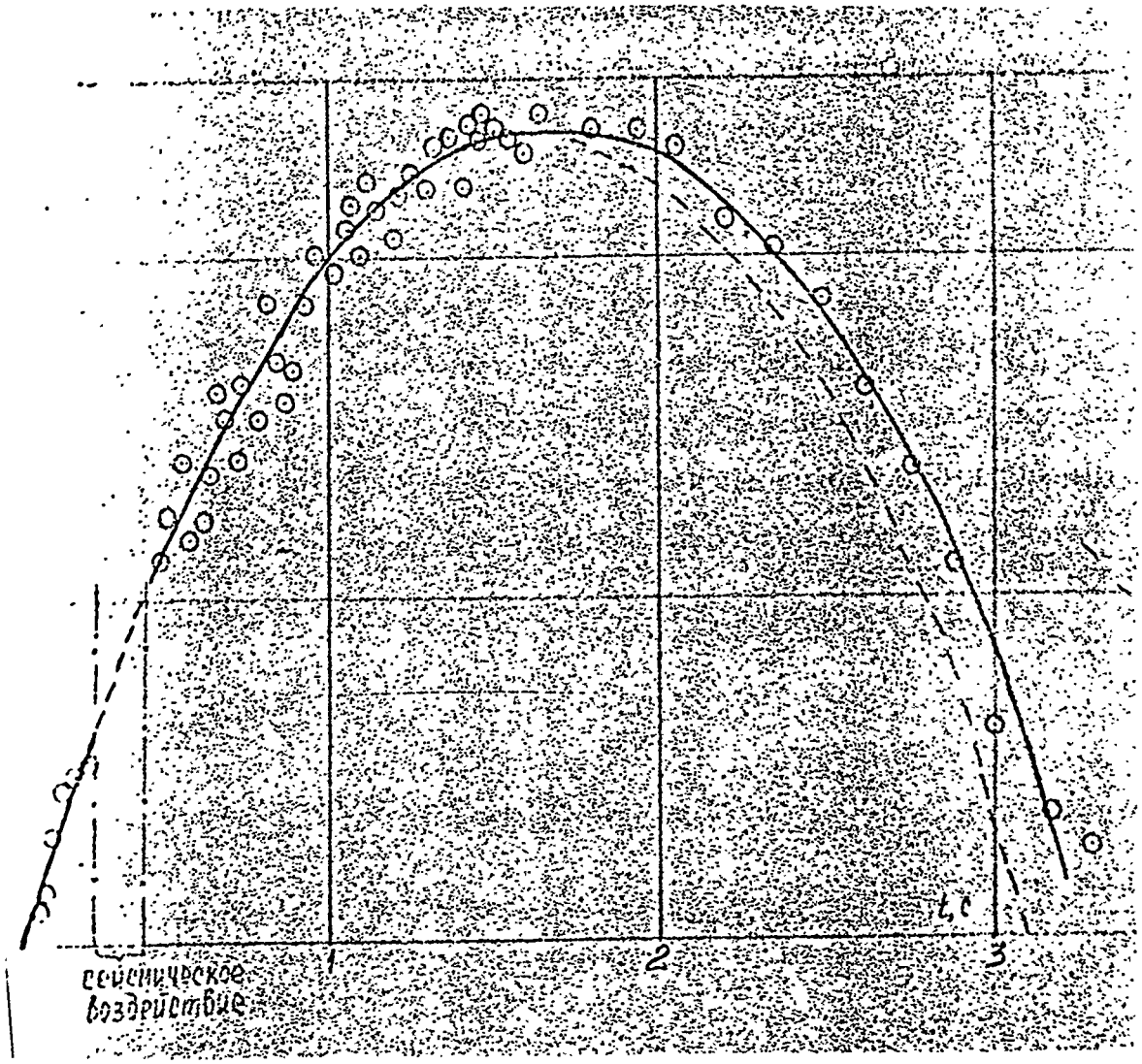

Figure 4.2. Dependence of the height of the dome lifting from the time seismic action.

From the figure we can see, that the dome lifted at the height of 11.5-12 m. To reach this lifting height the value of the splitting velocity must be equal to 15.5±0.2 m/s. For comparison, the following dependence is plotted at Fig. 4.2 by a dashed line, where v_0=15.2 m/c:

$$H = v_0 \times t - \frac{gt^2}{2} \qquad (4.1)$$

We can see that at the lifting stage the motion of the epicentral area coincides with the dependence (4.1), but at the fall stage the height decreases slower. It is explained by the fact, that at the fall stage motion of the dust rather than of the surface was registered at the stills. In any case the analysis of Fig. 4.2 gives an opportunity to confirm that the splitting velocity in ZB epicentre is equal to 15.2±0.2 m/s. This value is equal to 7.6±0.1 m/s at a distance of 300 m from ZB on condition that the mass velocity during the split is doubled.

4.4 Measurements of the stress wave parameters

4.4.1 Stress wave parameters in the gallery

The parameters of the stress wave during the experiment in the gallery N° 190 were measured by means of three types of the liquid velocity detectors (LVD) and their modified variant for measurements of large velocities (DLV), the induction velocity detector (IVD), and accelerometers with large attenuation (OSP-1, OSP-2). The great part of these devices was installed in the niches along left side of the gallery (from the portal to ZB) at the level of the excavation foot. Some devices were located in the lateral horizontal excavation at an angle of 80° to the gallery axis. This excavation is considered as an investigated fragment (IF).

Data registration was realized with help of the light-raying oscillographs N-119 (LVD and DLV), N-117 (OSP), and magnetic recorders NS-1135 (LVD).

In treatment of the records the times of the first arrival of the waves from the explosions to ZB and IB (t_h), the times of the increasing of the mass velocity from the arrival to maximum (t_n), the maximum velocities (u), and durations of the positive phases (τ_+) of the velocity of the massif motion were determined. These parameters are presented in Table 4.1. In the column "Comment" of this table the ciphers represent type and dislocation (the gallery or investigated fragment) of the detector:

Table 4.1. The stress wave parameters in the gallery

IB-wave						ZB-wave					
R m	comp.	t_b ms	t_n ms	U m/s	τ_+ ms	R m	t_b ms	t_n ms	U' m/s	τ_+' ms	Com-ment
30	x	19	-	74	-	-	-	-	-	-	1
50	x	23.4	0.9	30	-	-	-	-	-	-	1
	y	23.4	-	9.8	-	-	-	-	-	-	1
	z	23.4	1.3	4.8	-	-	-	-	-	-	1
70	x	27.3	1.3	4.2	-	-	-	-	-	-	2
	x	27.3	1.4	6	-	-	-	-	-	-	2
	x	28	0.9	12	-	-	-	-	-	-	1
140	y	42	-	0.8	-	440	-	-	-	-	3
155	x	43	6	3	43	455	90.5	13	1.5	50	3'
160	x	43	4.3	2.9	49	460	91.5	9.1	2.4	50	3'
170	x	45	2.9	2.2	49	470	-	-	-	-	3
	y	-	2.9	0.7	11	-	-	-	-	-	3
	z	-	2	0.9	9	-	93	5	0.6	82	3
170	x	45	2.3	1.9	42	470	88	9.1	1.4	-	4'
	y	-	-	1.2	-	-	-	-	0.1	-	4'
	z	-	-	0.6	-	-	-	-	2.3	-	4'
175	x	46.5	4.3	2.3	48	475	95	8	1.9	-	5
180	x	46.5	4.5	1.9	48	480	95	9	1.7	-	5
230	x	58	4	6	44	530	102	14	5.8	62	3
350	x	80.8	5	2.0	49	650	120	10	1.6	-	3
	y	-	-	0.5	-	-	-	-	1.7	-	3
400	x	88	9.2	0.8	35	700	134	18	1.3	50	3
	y	-	-	0.3	-	-	-	-	0.25	-	3
	z	-	-	0.1	-	-	-	-	0.7	-	3
	x	88	11	1.3	36	-	137	18	2.0	58	6
450	x	99	12	0.6	24	750	145	16	1.1	56	3
	y	-	-	0.2	-	-	-	-	0.3	-	3
	z	-	-	0.2	-	-	-	-	0.3	-	3
	x	99	10.5	1.1	36	-	145	17	1.6	50	6
	z	-	-	0.1	-	-	-	-	0.5	-	6

IB-wave						ZB-wave					
R m	comp.	t_b ms	t_n ms	U m/s	τ_+ ms	R m	t_b ms	t_n ms	U' m/s	τ_+' ms	Com-ment
490	x	-	11	0.4	40	790	-	15	0.8	90	3
	y	-	-	0.13	-	-	-	-	0.35	-	3
	z	-	-	0.14	-	-	-	-	0.56	-	3
	x	106	12.5	0.6	46	-	155	14.5	1.2	80	6
	z	-	-	0.28	-	-	-	-	0.8	-	6
600	x	130	12.5	0.3	40	900	180	16.5	0.62	80	3
	y	-	-	0.1	-	-	-	-	0.2	-	-
	z	-	-	0.2	-	-	-	-	0.6	-	-
700	x	142.5	20	0.26	45	1000	142.5	20	0.6	80	3
	y	-	-	-	-	-	-	-	-	-	-
	z	-	-	0.17	-	-	-	-	0.16	-	-
800	x	163.5	20	0.22	50	1100	217	20	0.5	80	-
	y	-	-	-	-	-	-	-	-	-	-
	z	-	-	0.05	-	-	-	-	0.17	-	-
IPA 1150	z	-	30	0.17	57	1450	-	30	0.4	-	7

1. the gallery, DLV;
2. the gallery, the detector MGDS;
3. the gallery, LVD;
3'. IF, LVD, the frontal side;
4. IF, LVD, at the foot, the frontal side;
4'. IF, LVD, at the foot, the back side;
5. IF, LVD, the back side;
6. the gallery, OSP;
7. IPA, the accelerometer B&K.

The distance between ZB and IB (300 m), the delay of the undermining time (15.3 ms), and the ratio of the charges powers influenced on the fact, that along the gallery ZB-wave arrival coincided with negative phase of IB-wave velocity. It resulted in the decrease of the maximum mass velocity in ZB-wave with respect to its parameters in the non-disturbed massif. The observed maximum velocity, without correction by its interference with negative phase of IB-wave, is presented in the column with ZB-wave velocity in Table 4.1.

Fig. 4.3 presents the hodograph of the first arrivals of ZB and IB- waves. The numbers correspond to the comments in Table 4.1. The hodograph slope for IB-wave arrival at distances

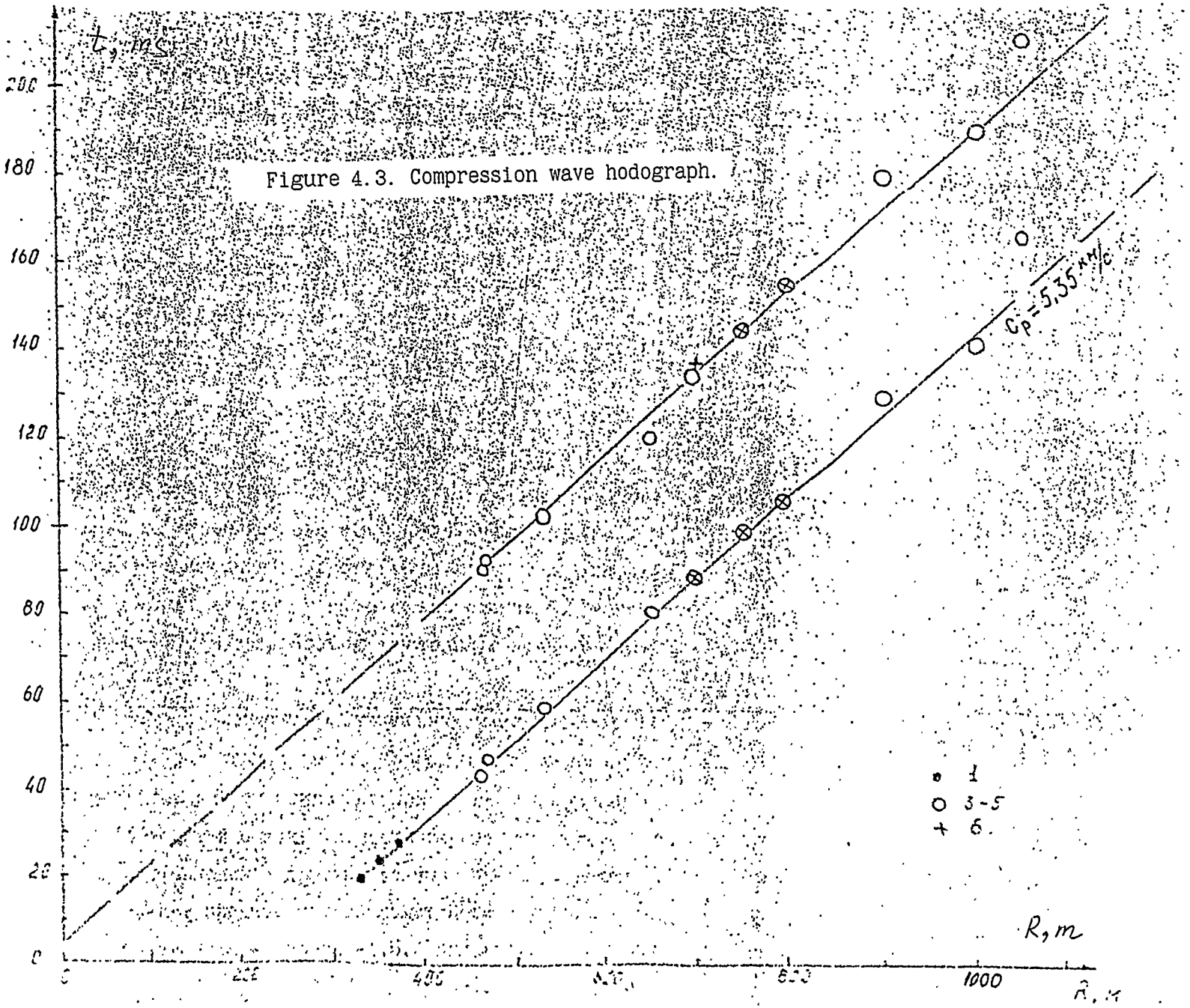

Figure 4.3. Compression wave hodograph.

from 300 to 1000 m corresponds to S-wave velocity of 5.35 km/s.

At the level of t=15.3 ms (because of the different time of the charges undermining) the hodograph of IB-wave is removed at 15 km from the explosion centre, that is in agreement with the empiric law of the displacement of the hodograph start point at the cavity radius (the calculated radius of the cavity was about 10 m).

The arrival of ZB-wave stands against a background of IB-wave epure not so distinct, so, at Fig.4.3 straight line for ZB-wave was plotted on the base of the data and have the same slope, as the slope for IB-wave. It is shown, that the projection of ZB-wave hodograph on zero distance passes above the explosion zero. It is the consequence of the fact, that ZB-wave, which rounded ZB-explosion epicentre and had the biggest path, comes to the gallery as wave, screened by IB-explosion centre. The redundant path of ZB-wave might be estimated as 30 m, that at a distance of 500-1000 m corresponds to the effective size of screen of about 100 m. This value is comparable with the dimension of the crackness zone after IB-explosion.

If we compare these experimental data with the results of the investigation of the action of seismo-explosive waves with screens of various form, the screen influence of IB-charge explosion on ZB-wave parameters at distances from IB, which are greater or equal to b_m, might be estimated if we'll change the zone of the non-elastic deformations after IB-explosion by the circular flat screen with radius of 0.4-0.68 b_m, located in IB-region, where b_m is the radius of the zone of the non-elastic deformations after IB-explosion.

The Fig.4.4 presents the relation between the time of the velocity increase to maximum and absolute distance, passed by the wave. The light circles correspond to IB-wave and dark circles represent ZB-wave data. Stright lines represent the next dependences:

$$t_{nIB} = \frac{R}{40} \qquad t_{nZB} = \frac{R}{50} \qquad (4.2)$$

where R is the distance, measured in meters.

The data scattering doesn't allow to do some definite conclusion of the dependence between the increase time and the distance, though there is some delay of the growth of the increase time for ZB-explosion at the distances greater 700 m, where it become constant with value of about 18-20 ms.

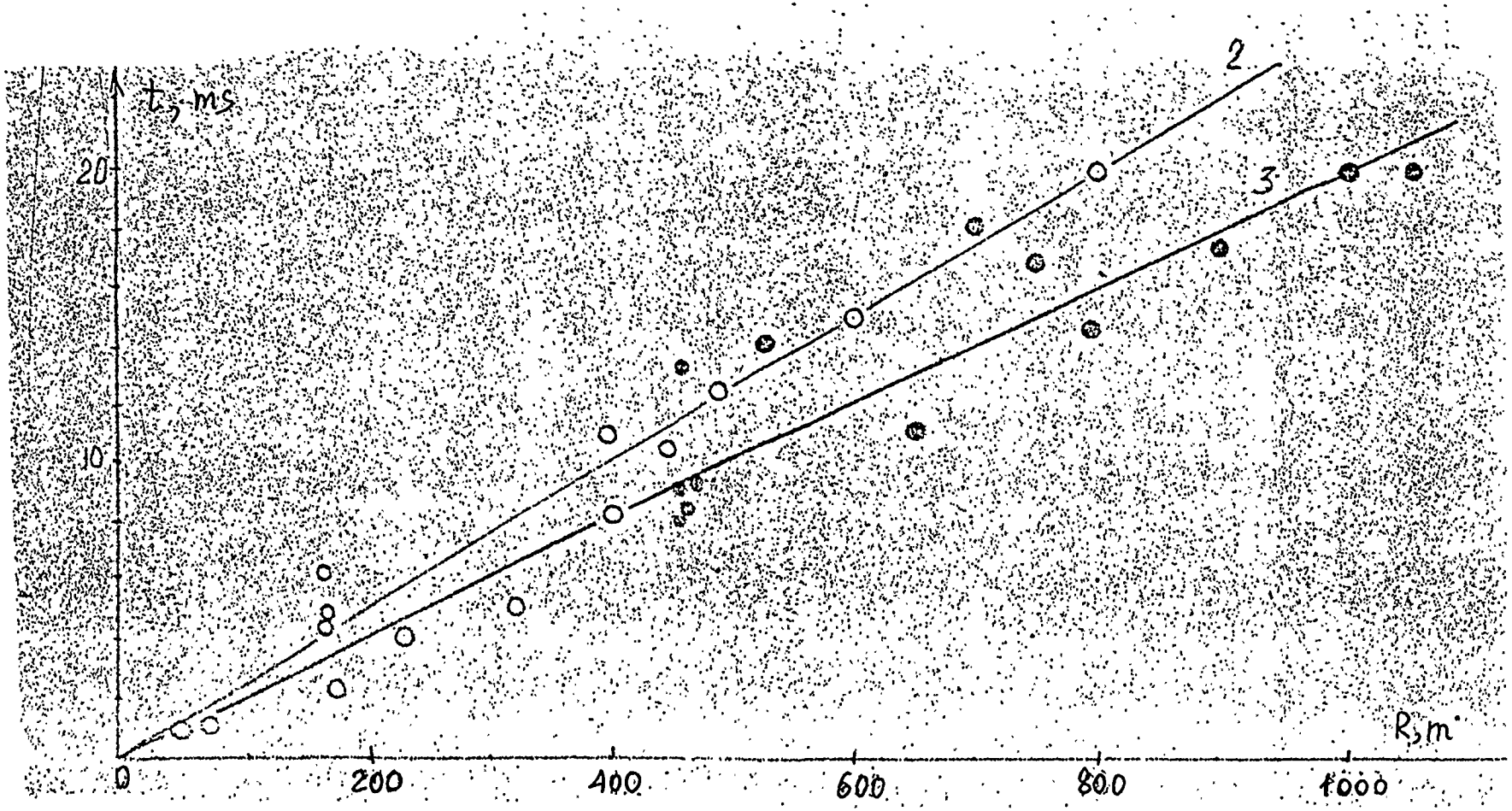

Figure 4.4. Dependence of the time of the velocity increase from the distance.

The Fig. 4.5 shows the dependence of the maximum mass velocities in the first wave on the distance to IB. The approximation of the main data mass by the attenuation law with exponent -1.65, that is typical for Degélen area, gives the explosion power estimation of about 1 kt. In comparison with other data this power seems understated, that allow to assume the greater value of the exponent in the attenuation law. It must be about -1.8. Straight line with this exponent of the attenuation is shown at Fig. 4.5 by a solid line. The dashed lines with numbers 1 and 2.5 represent the normative dependence of the velocity on the distance, calculated by the next formula:

$$U = 300 \left[\frac{R}{q^{1/3}} \right]^{-1.65} \qquad (4.3)$$

where q is the explosion trotyl equivalent, t.

Besides the data from Table 4.1., Fig. 4.5. represents the data, received by means of DDS and LVD detectors. We can see a great scattering of the data received for the IF (investigated fragment). The maximum velocities measured by means of different detectors along X-component vary from 2 to 5 m/s. Now it is difficult to explain the causes of this scattering.

As it was stated above, the maximum velocity in ZB-wave coincides with the negative phase of IB-wave velocity. Let's assume, that the duration of the negative phase of the velocity τ_- is twice as much than τ_+ and, therefore, the amplitude is a half of the maximum velocity in the positive phase, than it is possible to introduce the correction and to estimate the maximum velocity in ZB-wave in the non-disturbed massif by addition a half of IB-wave amplitude to ZB-wave amplitude. The values of the maximum in ZB-wave are shown at Fig. 4.6 by segments of straight lines. The lowest point of the segment corresponds to the measured values and the upper point represents the value corrected at an influence of the negative phase of IB-waves. The circles represent the data, received by means of LVD, and squares represent the OSP data. The value of the velocity, received from the data of filming of the rock crest motion in the area of ZB-explosion epicentre, is shown by a black square. Dashed straight line, plotted through the upper point with slope of -1.65, gives the power estimation of about 40 kt according to the formula (4.3). The slope of the solid line, plotted on the base of the GIS data and passed through the black square, is equal to -2.

The accelerometers with great attenuation (OSP) were installed at distances of 700 m (X-component), 750, and 790 m (X- and Z-components) from ZB. The detectors readings were handly digitized with step of 1 m and then they were integrated.

The integrated accelerogramms are shown at Fig 4.7., 4.8 .

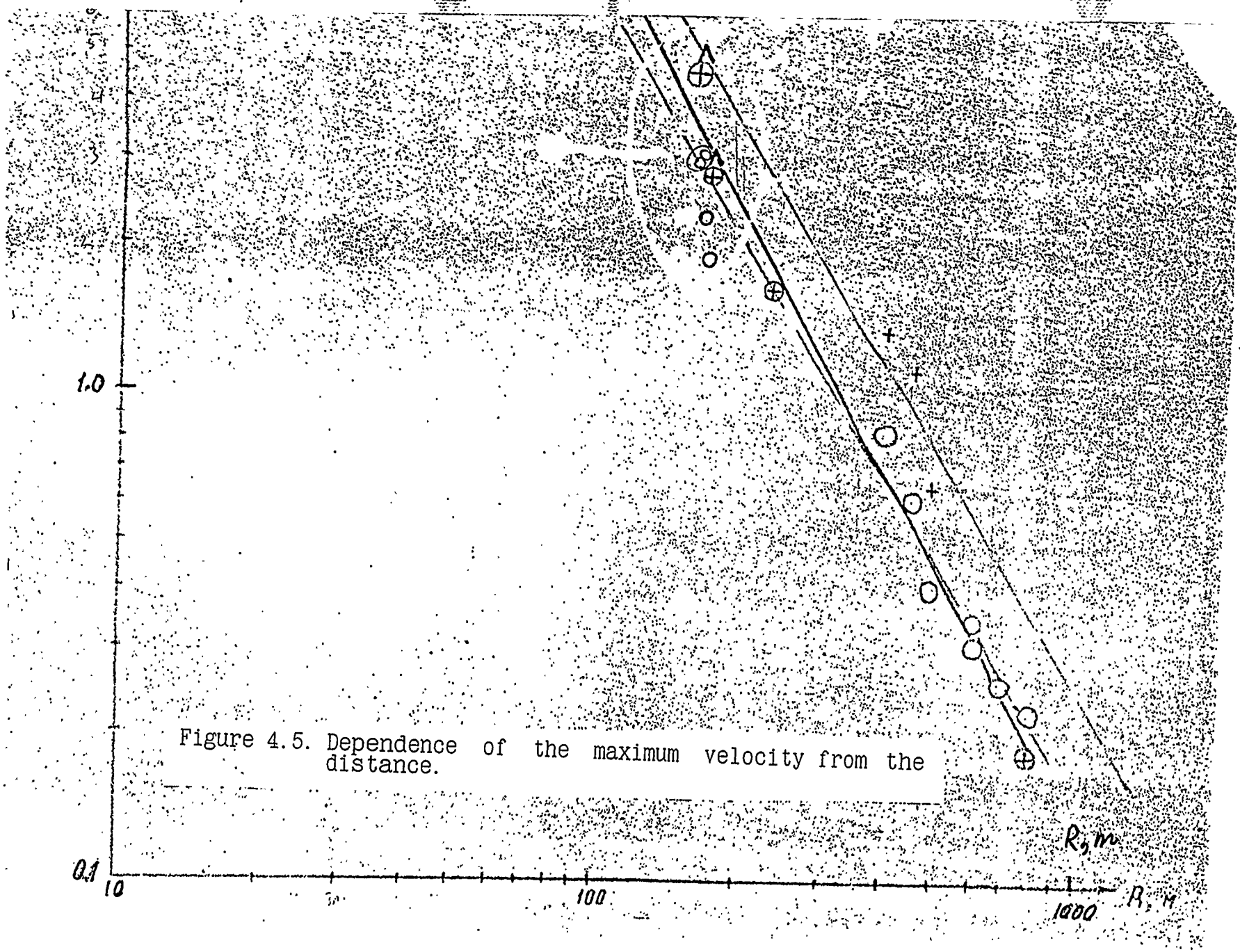

Figure 4.5. Dependence of the maximum velocity from the distance.

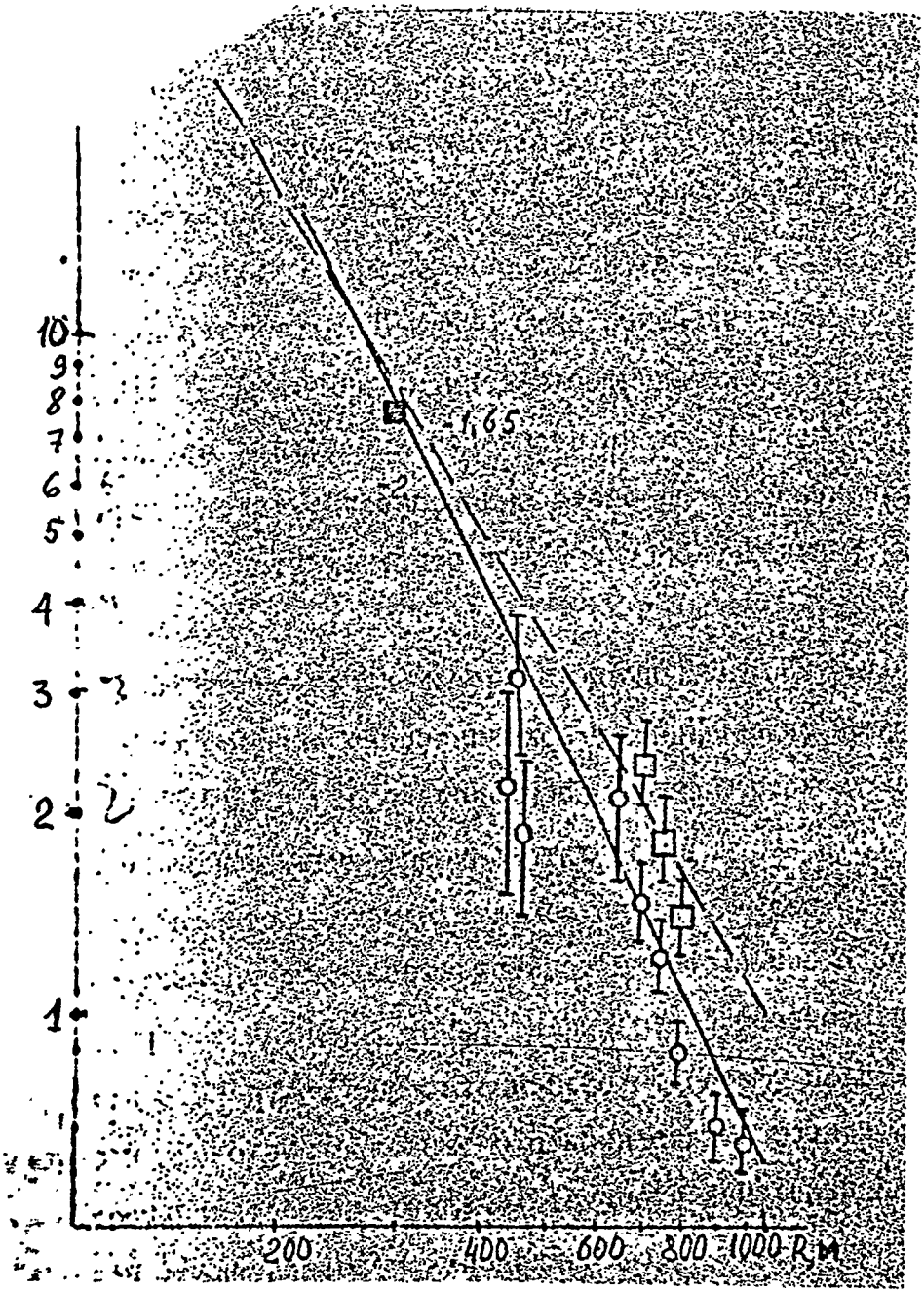

Figure 4.6. Dependence of the maximum velocity from the distance.

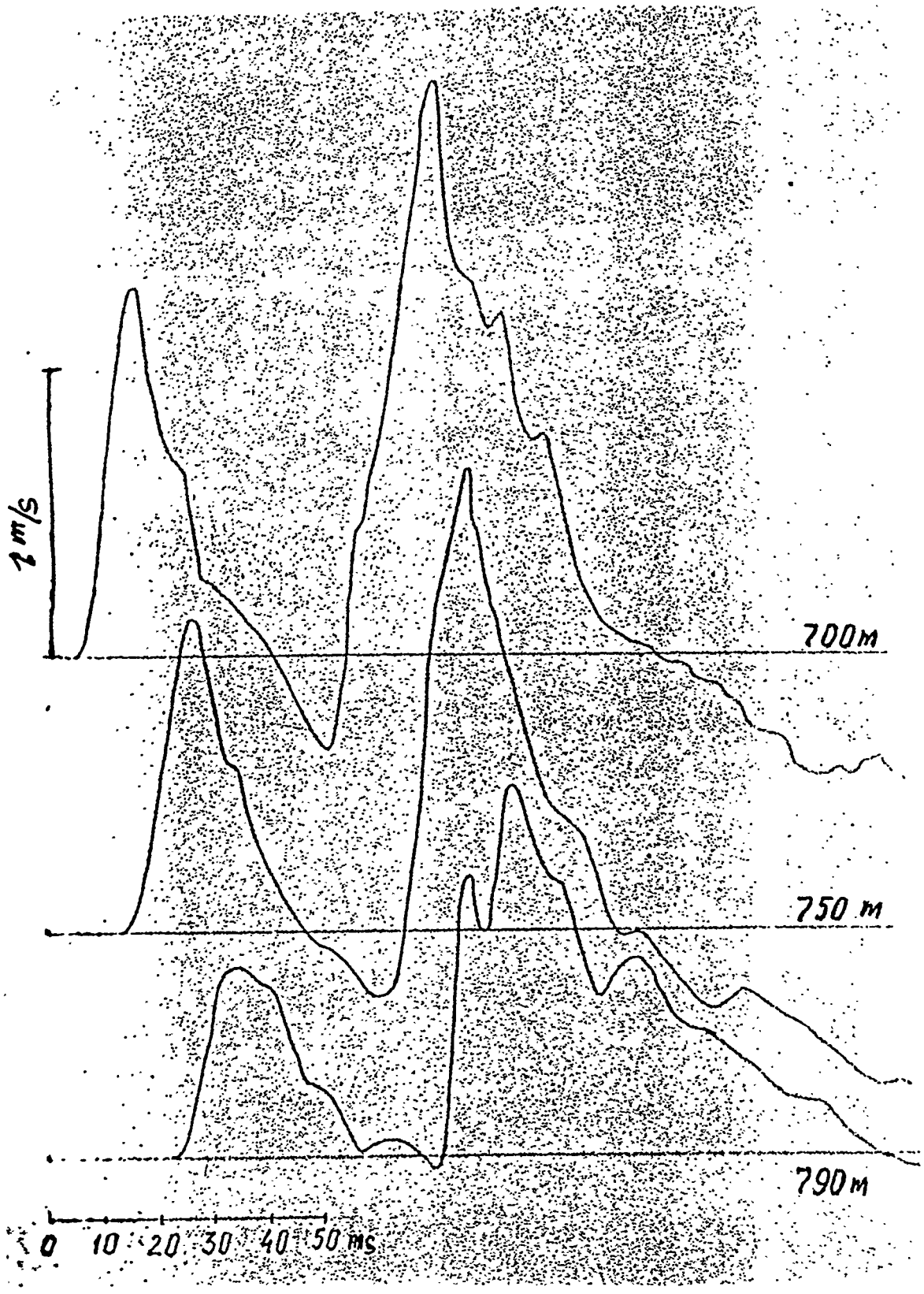

Figure 4.7. Velocity epures in the compression wave. (OSP detectors)

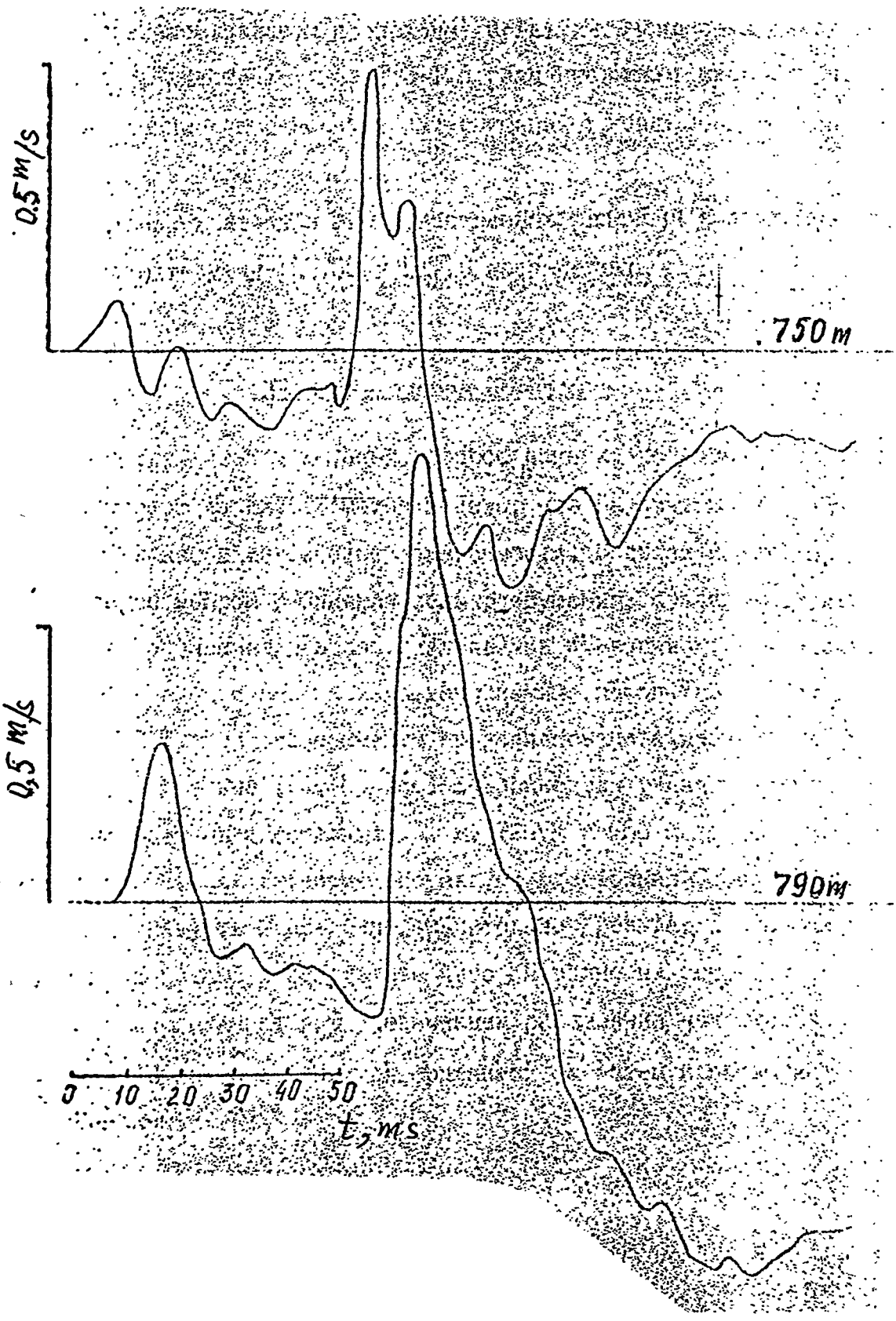

Figure 4.8. Velocity epures in the compression wave. (OSP detectors)

and in Table 4.1. The comparison of the velocity epures with data from LVD detectors, installed at the same points, showed their full identity as concerns the curves form and time parameters (t_b, t_n, and τ_+). But the velocity amplitudes were in 1.6±0.1 times greater than LVD data. The analogous systematic exceeding of the amplitudes with full equivalence of the velocity epures for OSP and LVD detectors was previously observed in the experiment at the gallery N° 215. Analysis the work principles for OSP and LVD detectors doesn't give the base for the explanation of this systematic discrepancy. It is possible to assume, that the cause of this discrepancy lies in the method of the detectors graduation, but this assumption demands additional metrological investigations.

OSP detectors were placed at points with some tectonic disturbances between them. The watered fault laid between PQ 700 and PQ 750 m, and zone of the greatly cracked rocks with 25 m in width was located between PQ 750 and PQ 790 m. The crackness zone along the gallery was covered by solid timbering. The wave arrival for these three pickets corresponds to P-wave velocity of 5 km/s, that, within the experiment accuracy, coincides with the mean velocity of 5.35 km/s, determined from IB-wave hodoraph. There were no differences between the wave velocities in the relatively solid rocks and in the crackness zone. Beyond the bounds of the crackness zone the epure form was changed: there IT was observed a sharp decrease of the maximum velocity in comparison with the typical attenuation law and an increase of the duration of IB-wave positive phase. These features were character to ZB-wave epure too.

The epures of the velocity vertical component at the piquets 750 and 790 m, received by the integration of FSP accelerogramms, are shown at Fig. 4.2. We can see, that in spite of the general similarity of the oscillations, the block motion beyond the bounds of the crackness zone has more intensive character - the maximum velocities at the piquet 790 m are in 1.3 - 1.5 times greater than the velocities at PQ 750 m. Amplitudes of the relative displacements of the crackness zone are equal to 1-2.5 sm at the base of 40 m.

On the base of the LVD detector data there were no significant differences between the motions in Y-component for PQ 750 and PQ 790 m.

4.4.2 Stress wave parameters along the surface

The stress wave parameters along the surface were measured by LVD and DLV detectors and recorded at the magnetic tape IS-1135. The scheme of the detectors location is shown at Fig. 4.2. and the results of the magnetogramms decoding are

represented in Table 4.2.

Table 4.2. Stress wave parameters along the surface

IB-wave						ZB-wave			
N	comp.	t_b ms	t_n ms	U m/s	τ_+ ms	t_b ms	t_n ms	U' m/s	τ_+' ms
1	x	76	20	3.5	-	-	-	-	-
	z	76	25	3.5	-	-	-	-	-
2	x	130	15	1.3	37	20	22	3.0	85
	y	-	-	-	-	-	280	0.5	340
	Z	130	12	0.5	55	200	18	0.6	72
3	z	145	30	0.26	55	206	25	0.51	80
4	x	127	12	0.15	-	200	15	0.35	155
	y	132	50	0.05	-	227	100	0.23	180
	z	120	10	0.3	50	200	10	0.5	65

The measuring points along the surface were placed before and behind the fault IV.

Due to the large cable length, unfavorable weather conditions, and velocities amplitudes in the stress wave, which are significantly less than the predicted values, the completely qualitative records, available for decoding, were received at points 2 and 4 and partially qualitative records were made at points 1 and 3.

Analysis of Table 4.2 allows to mark the next features:

- the amplitude of the horizontal component of the motion velocity sharply decreases behind the fault for IB-wave as well as for ZB-wave;

- the amplitude of the vertical component was constant within the experiment accuracy;

- the time of the velocity growth in the vertical component for ZB-wave behind the fault increased in 3 times;

- the increase time in X- and Z-components for ZB-wave along the surface was less than in the gallery, but the arrival time differences for ZB- and IB-waves were greater. To all appearance, it is explained by the screening splitting soil motion after IB-explosion (the

soil solidity was destroyed), so the "real" increase time for ZB-wave in X- and Z-components was at 15-20 ms greater than the observed values.

4.5 Measurements of the residual deformations

In study of the geomechanical process the much attention is devoted to the observations of the medium deformation, that gives an opportunity to control its state and, finally, to do some conclusions about the dynamic of these process development.

Side by side with the traditional geophysical problems the tasks, connected with man-made changes of the geological medium and, in particular, with explosion effects, appear more often. The explosion may initiate a number of the geophysical processes, which are weakly shown in the natural medium state, and, so, investigated insufficiently now.

The aim of the observations consists in the receipt of the information about these deformations and the study of their character.

The rock massif, where the gallery was drifted, is the zone, crossed by the faults of different types.

The changes of the massif tense state may provoke some deformation along the fault zone bounds.

To measure the deformation it is necessary to investigate the points of the displacements and to determine their quantitative characteristics.

The areas along the gallery near the faults IV, V, and VI, the sections of the ending wall of the investigated fragment, and the areas on the massif surface over the gallery at the fault outcrop were chosen for these observations.

To estimate the linear and angular displacements the next parameters were measured:

-linear displacements across the fault;
-vertical displacements along the gallery;
-vertical slopes along the gallery;
-vertical and horizontal displacements on the massif surface;
-the cross section of the cracks on the massif surface after a repeated action.

The devices location and the position of the control bench-marks in the gallery are shown at Fig. 4.9.

4.5.1 Measurement of the linear displacements in the region around the faults

To measure large deformations with values in the range of 0.5-190 mm the special projected apparatus was used. The scheme of this system and its location on the fault are shown at Fig. 4.10.

The deformograph base was attached by one of its end to the fault side and by the second - to the system of the resistive detector, installed on the other side of the fault. The detector was used for the transformation of the linear displacements to the electric signal. The deformograph scheme is shown at Fig. 4.11.

In this experiment we used the resistive detector, based on the scheme of the unbalanced bridge with follow condition of the equilibrium: $R_1 \times R_4 = R_2 \times R_3$. The tension of the output signal is determined by the dependence of $U_{signal} = \Delta R/R \times U$ in the regime of small values of $\Delta R/R$ ($R \to \infty$). This bridge scheme is practically free from the temperature effects influence and its sensitivity is in 4 times greater than for the one-arm scheme. The recording of the signals from the detector was realized by means of the light-ray oscillograph N-117 to the photographic paper. The graduation of all detectors and zero control were made before the measurements.

The data of the deformographs position and results of all measurements are represented in Table 4.3.

The information from the device, installed on the ending wall of IF, wasn't received due to the cable break after the gallery roof collapse. But the records of the residual deformations were received by means of the other deformographs. The displacements along the faults have the same signs. The fault sides have drawn nearer after the influence. Absolute values of the displacements are in the range of 4-75 mm. Analogous behavior was observed in the experiment N° 215. The differences between the absolute values of the displacements along the faults V and VI might be explained by the heterogeneities in their geophysical structure and tense state and by the different types of the devices installation. The deformograph an the fault VI covered only watered part of the fault with length of 4 m. The cross-section of whole fault was equal to 30 m. It is possible to note, that the absolute values of the horizontal displacements along the fault IV are similar to the vertical motion in the fault region. The results of these measurements are presented below.

Table 4.3. The results of the deformation measurements

N	Location	Deformograph base, B, mm	Cable number	Distance from ZB, m	Feeding voltage U_V, V	Calibration		Cable resistance signal/ feed Om	Calibration by oscillograph		Measured signal		Relative residual deformat $\Delta L/L$
						voltage U_V, V	displacement ΔL, mm		U_{sign} V	ray displacement mm	U_V, V	ΔL, mm	
1	Ending wall of IF	1920	2006	400	24.8	1	11.1	45/ 27	1	2.4	-	-	-
2	Fault IV	4321	2009	520	24.5	1	8	1160/ 1200	1	2.4	0.5	4÷8	$9.3\times10^{-}$
3	Fault V	2320	2010	680	23.5	1	10.25	1400/ 1330	1	1.83	3.3	41.5	$1.8\times10^{-}$
4	Crackness zone IV	25330	2011	765	24.9	1	10	1230/ 1050	1	2.95	2.4	24÷75	$9.5\times10^{-}$

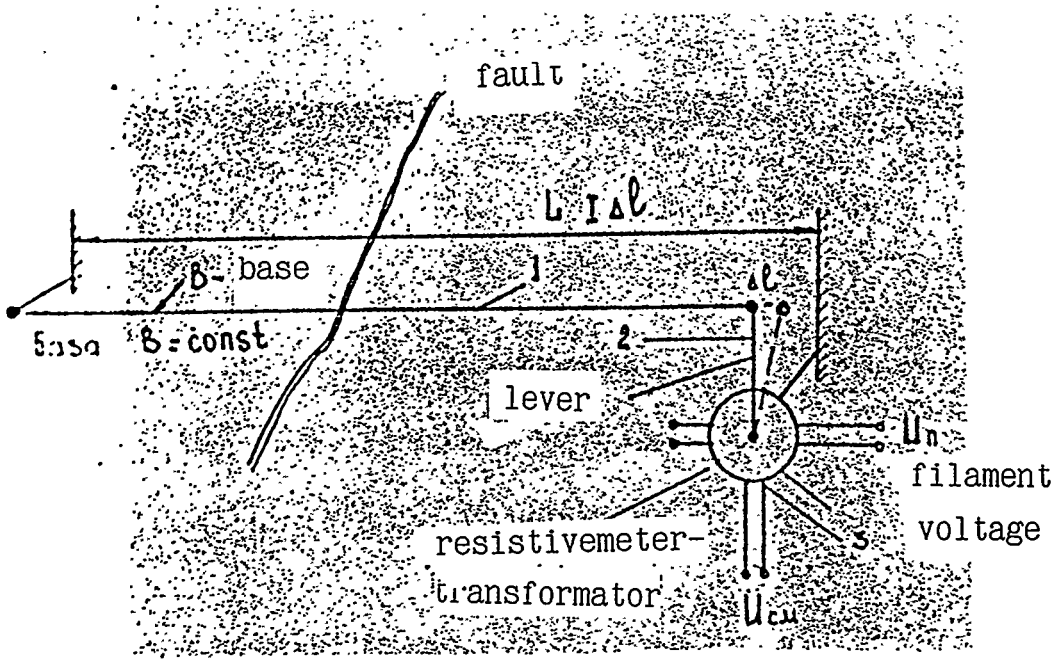

Figure 4.10. Scheme of the device installation.

1. Base
2. Lever
3. Detectors

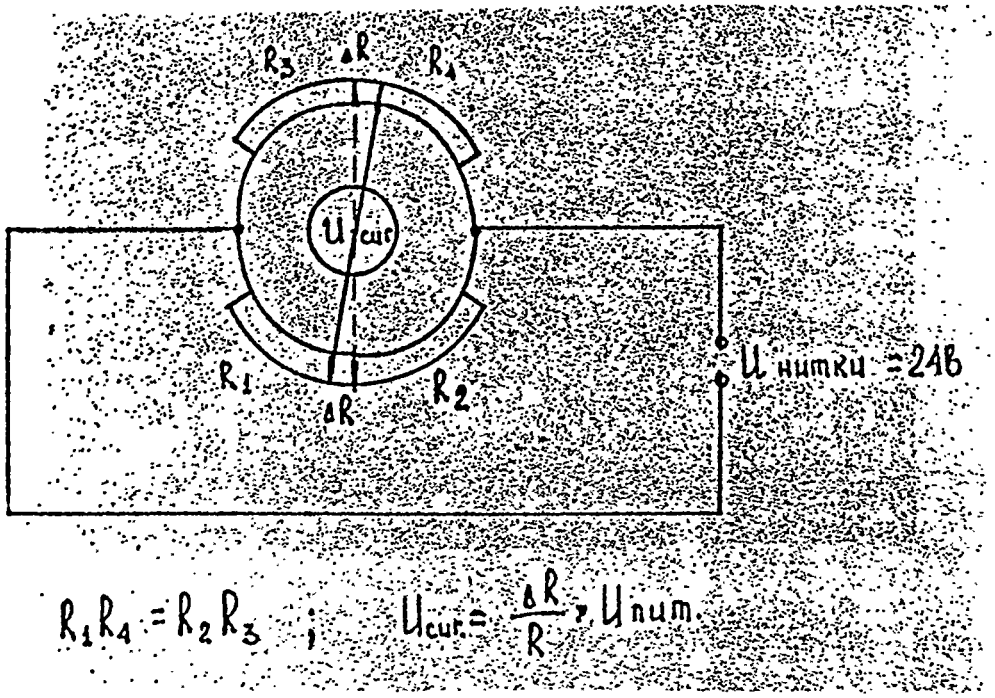

Figure 4.11. Scheme of the deformograph.

4.5.2 Measurements of the vertical displacements and slopes in the gallery

The leveling by means of 20 bench-marks, located on the upper roof of the gallery and 11 loading details in the gallery wall, was realized before the experiment to reveal the residual vertical displacements and vertical slopes along the gallery. The measurements of the vertical slopes was made by means of the loading details in two planes: along the gallery and on its cross-section.

After the explosion only bench-marks located up to PQ 800 m, and installed details located before PQ 700 m were available.

Table 4.4. The leveling results

Bench-marks					Installed details			
Distance from ZB, m	Location	Before explosion	After explosion	Measured displacement Δ, mm	Number & distance m	Before explosion	After explosion	Measured displacement Δ, mm
Portal		8758	8764	+6	Portal	-	-	-
1250	Between the faults I-II	8839	8830	-9	N11 (1200)	8422	8432	+10
1200	- " -	9233	9239	+6	N10 (1100)	8725	8731	+6
1150	- " -	9276	9272	-4	N9 (1015)	9007	9015	+8
1100	- " -	9606	9612	+6	N8 (900)	9523	9548	+25
1050	- " -	9906	9914	+8	N7 (780)	9950	9963	+13
1000	- " -	9806	9814	+8				
950	Between the faults II-IV	10118	10131	+13				
900	- " -	10780	10797	+17				
800	- " -	10660	10679	+19				

The leveling results are represented in Table 4.4, and the slopes measurements are in Table 4.5.

Table 4.5. Results of the slopes measurements

Installed detail number	Distance from ZB, m	Location	Before explosion	After explosion	Measured slopes
Portal	1290	-	-	-	-
11 00° 90°	1200	Between the faults I-II	356°57'58" 16°44'22"	356°58'12" 16°44'42"	+14" -40"
10 00° 90°	1100	- " -	8°04'26" 11°57'24"	8°04'42" 11°56'58"	+16" -26"
9 00° 90°	1015	- " -	6°22'18" 17°53'05"	6°22'30" 17°53'25"	+12" +20"
8 00°	900	Between the faults II-IV	2°48'20"	2°48'46"	+26"
7 00°	780	- " -	2°19'55"	2°20'06"	+11"
6 00° 90°	756	Between the faults IV-V	356°53'44"	357°02'23"	+08'39"
4 00° 90°	690	- " -	358°02'25" 10°36'18"	358°11'08" 10°39'50"	+08'43" +03'32"

The leveling on the base of bench-marks and loading details shows, that there is displacement in the vertical direction along the gallery to PQ 800 m. These results are analogous to each other. At the area between faults II-IV the displacements are in 1.5-2 times greater than in the near-mouth part, where the leveling results are close to the measurements accuracy. It is possible to assume that the block between the fault II-IV moves as a whole. The values of the vertical displacements in the gallery and on the surface over the fault II outcrop are similar.

The angular measurements were made on the base of the loading details along the gallery (0°) and in the perpendicular direction (90°). The optical quadrant Q0-10 with the device accuracy ±10'' was used in these measurements. The slopes of the

details, installed between the faults I and II, are the same within the measurements accuracy. The slopes of two loading details N6 and N4 with a distance of about 70 m between them, located between the crackness zone IV and the fault V were the similar and equal to 9''. It allows to conclude that there is an angular displacement of the whole block at this value. The sign "+" shows that the block part nearest to the crackness zone IV has been lifted.

As a conclusion we must noted the fact, that the boundaries of linear and angular displacements coincide with the position of the faults, typical for these displacements.

4.5.3. Measurement of the vertical and horizontal displacements on the massif surface at the region of the outcrop of the fault II

The measurements of the residual displacements by means of the bench-marks, located on the fault centre and its sites, were realized at the region of the outcrop of the fault II on the massif surface. The scheme of the bench-marks installation is shown at the Fig. 4.12. Each bench-mark was leveled before and after the explosion by the program of the third class leveling. The bench-marks N0, N1, and N2 were installed before the fault, the bench-marks N3, N4, and N5 - on the fault crest, and the bench-marks N6, N7, and N8 were installed beyond the fault. Furthermore, the leveling was realized through the bench-marks IX, X, XI, XII, and PQ-3 in the direction to the epicentre. The relative displacement, received as a result of the leveling, are represented in Table 4.6.

The greatest vertical motions were observed in the bench-marks, located on the fault crest. It might be explained by the increase of the fault activity after the explosion. The leveling along the valley in the direction of the epicentre gives monotonous growth of the vertical displacements.

The horizontal displacements were measured by means of these bench-marks in the directions, shown at Fig. 4.12. The error of the linear measurements was equal to ±5 m.

The results of the measurements are presented in Table 4.7.

As we can see from the Table, the bench-marks, installed on the surface at a distance of 1000 m from ZB and oriented in the direction of influence, brought together at a value of 50-100 m.

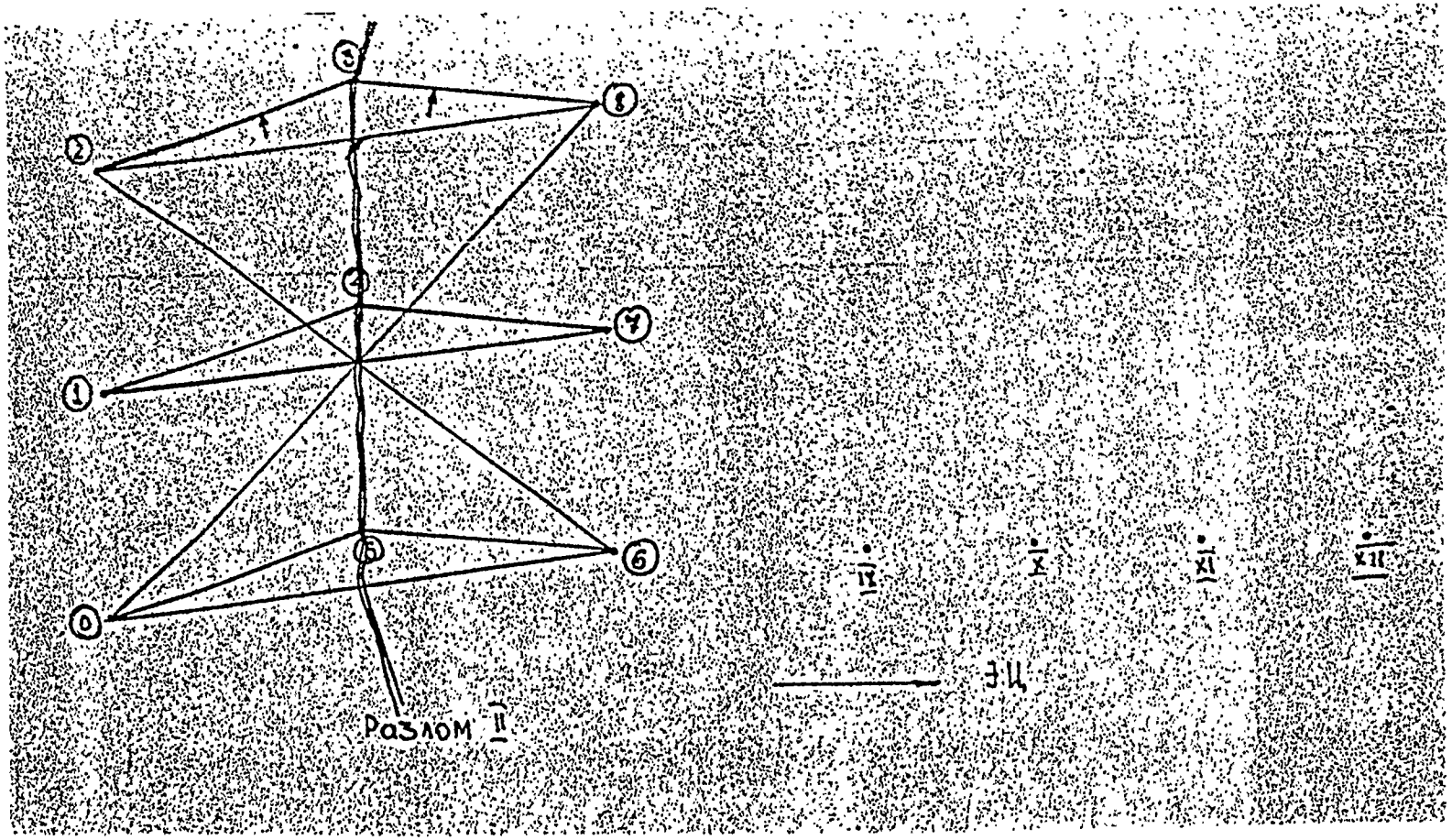

Figure 4.12. Scheme of the bench-marks position on the surface at the region of the fault II outcrop.

Table 4.6. Results of the measurements of the relative displacements

Bench-mark number	Relative displacement Δ, mm	Bench-mark location	Bench-mark number	Relative displacement Δ, mm	Bench-mark location
0	0	Before the fault	IX	+2	Leveling along the valley in the direction to the epicentre
1	+23	- " -	X	+11	
2	+14	- " -	XI	+11	
3	+75	Along the fault	XII	+18	
4	+79	- " -	PQ	+812	
5	+84	- " -			
6	+5	After the fault			
7	+8	- " -			
8	+13	- " -			

4.5.4. The observations of the man-made cracks on the massif surface

The dashed line at Fig. 4.2 marks the site N1 between the precipice over the valley and steep part of the slope. Before the explosion some cracks, formed after the previous explosion in the neighbour gallery, were discovered on that site. The character of these cracks origin is shown at Fig. 4.13. As a result of the full influence of the gravity and loading after the explosion, the zone of the tension stresses is formed on the slope surface over the precipice. These tension stresses result in formation of the joint set in the massif. The line of the bench-marks was installed on the site across the joint set. This line and part of the joint set are represented at Fig. 4.14. The distances between the bench-marks, the joint thickness near the bench-marks, and a distance from one side of the joints to the nearest bench-mark were measured before the explosion.

The site was investigated immediately after the explosion. There was no collapse of this slope section, except the fall of

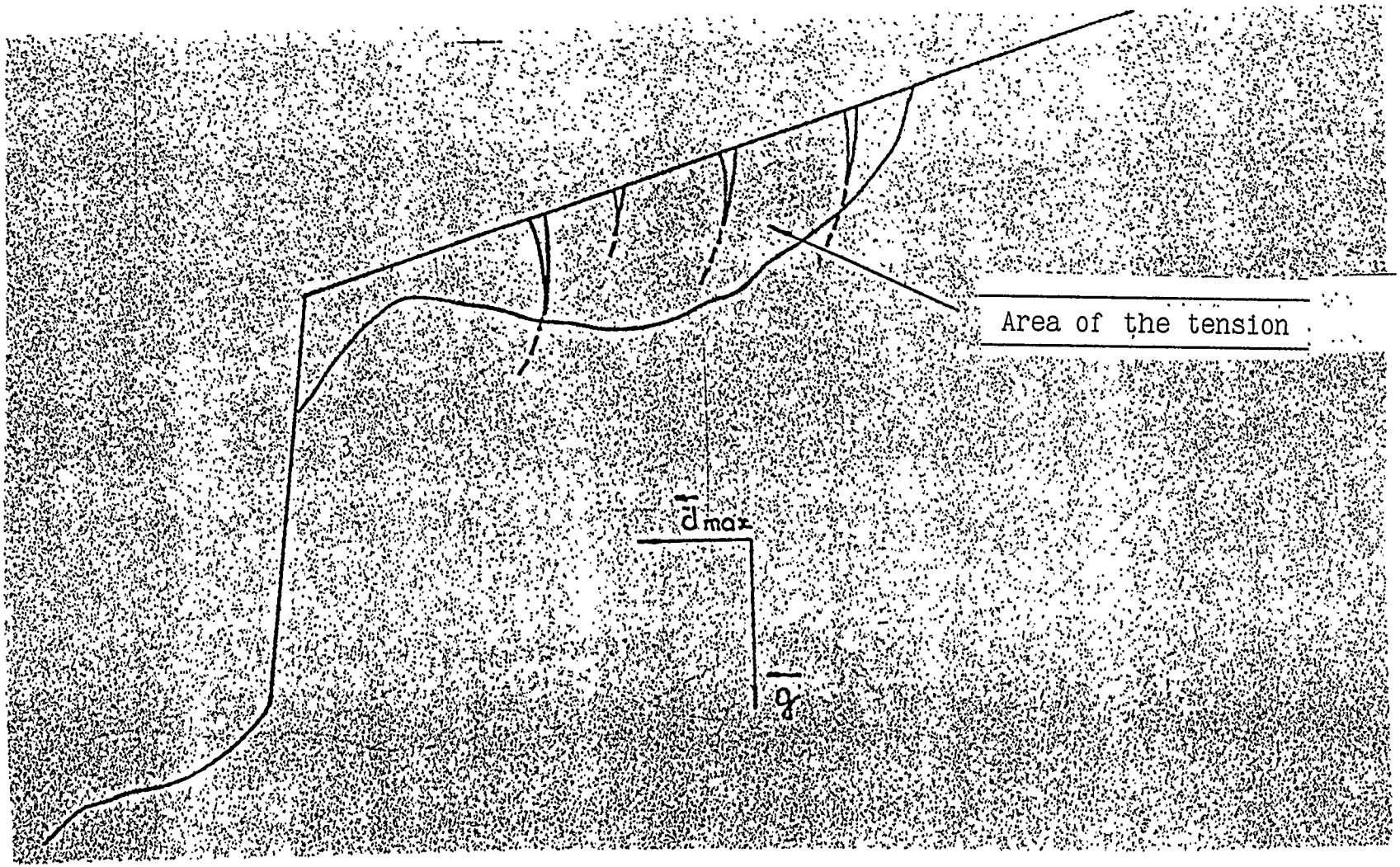

Figure 4.13. Scheme of the cracks formation.

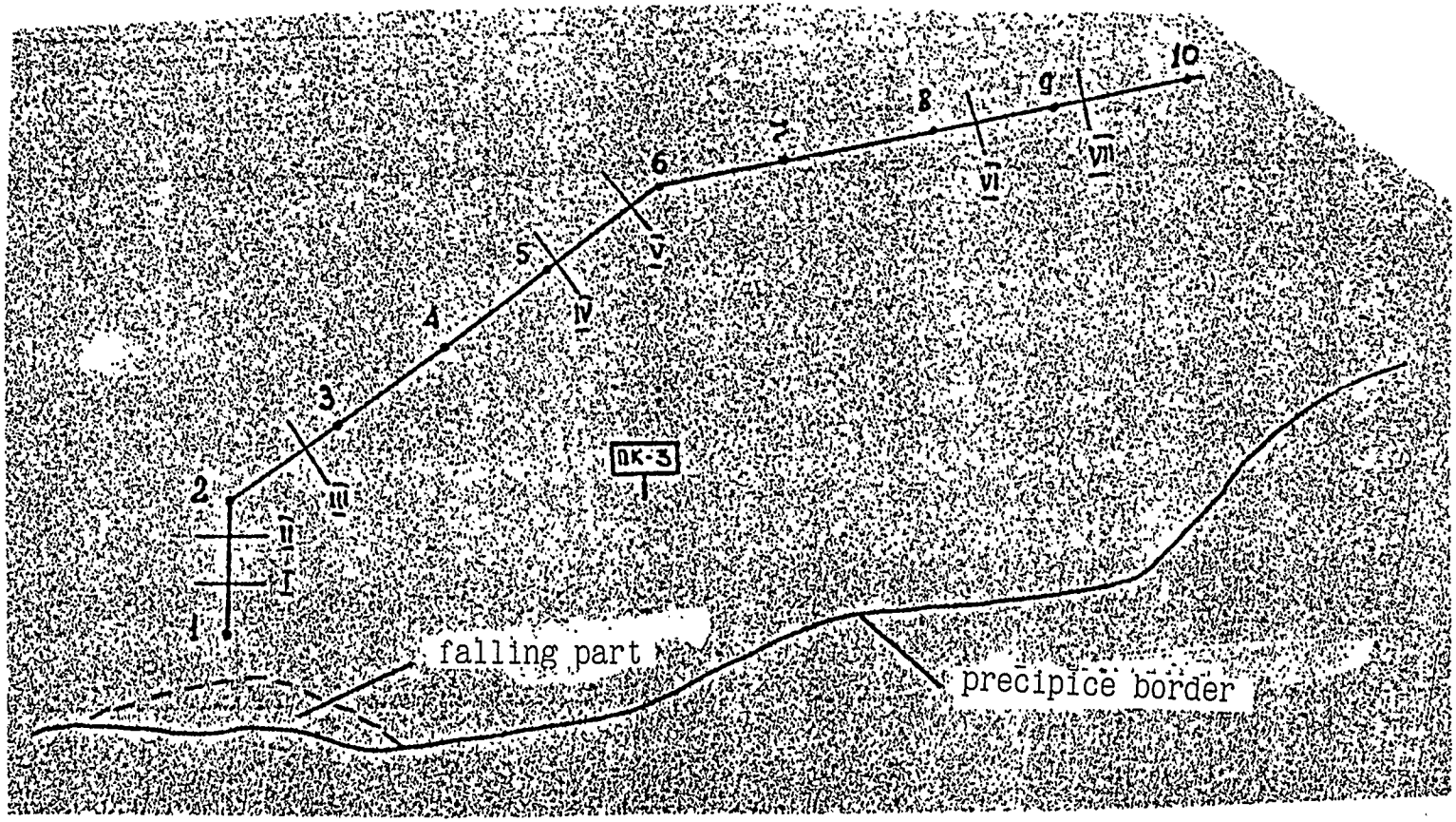

Figure 4.14. Scheme of the cracks and bench-marks position at the site 1.
•3 - bench-mark
III - cracks

Table 4.7. The results of the measurements of the relative displacements

N	Measurements direction	Distance before explosion, m	Distance after explosion, m	Displacement Δ, mm
1	0-8	27.310	27.195	115
2	0-5	11.255	11.180	75
3	0-6	24.610	24.495	125
4	1-4	13.450	13.370	80
5	1-7	22.580	-	-
6	2-6	45.980	45.870	110
7	2-3	20.600	20.540	60
8	2-8	28.550	28.465	85
9	3-8	8.185	8.150	35
10	4-7	9.195	9.165	30
11	5-6	13.585	13.585	25

the precipice edge at some points at a depth of 1-3 m. The distances between the bench-marks were measured again. The results of the measurements before and after the explosion are shown in Table 4.8.

We can see, that the site deformation comes to the increase of the crack thickness, and the deformation decrease sharply from the precipice to the site centre.

So, the influence activity as well as its orientation are significant for the slope collapse. In this case the presence of the joints didn't result in the collapse due to the weakness of the influence and its direction along the joints. But the repeated influence of the explosion in the massif, destroyed on the jointness, revealed to further decompression of its structure. This feature must be studied during the experiment with the explosion in the massif, destroyed by some previous explosions.

Table 4.8. The changes of the distances between the bench-marks

Bench-mark number	Distance before explosion d_1, m	Distance after explosion d_2, m	$\Delta d=d_1-d_2$, m	Cracks between bench-marks	Cracks characteristics before the explosion
1-2	4.92	5.67	0.75	I, II	width I - 0.25 m width II - 0.1 m
2-3	4.92	5.28	0.36	III	width III - 0.35-0.75m
3-4	4.90	4.90	0	-	
4-5	4.95	4.95	0	-	
5-6	4.97	5.01	0.4	IV, V	width IV - 0.3 m width V - 0.00 m
6-7	4.93	4.93	0	-	
7-8	4.97	4.97	0	-	
8-9	4.84	4.85	0.01	VI	width VI - 0.1 m
9-10	4.96	4.98	0.02	VII	width VII - 0.07 m

5. TECTONIC ENERGY INFLUENCE ON THE MECHANICAL EFFECTS OF THE UNDERGROUND NUCLEAR EXPLOSION, CARRIED OUT IN JULY 8, 1989

5.1. Brief characteristic of the rock massif in the explosion area

Rock massif in the explosion area consists of the volcanogenic-sedimentary and metamorphic rocks of the Turney layer of Kayandian suite of the Lower Carboniferous system and volcanogenic-sedimentary and metamorphic rocks of the Amchinsky layer of Maidan suite of the Middle Cambrian System, formed in the Hercynian and Caledonian orogeny, correspondingly.

Fig. 5.1 represents review submeridional geological section and Fig. 5.2 represents more detail geological section of the rock massif near the fighting well. Rocks, typical for this area, with the exception of the intrusive formations with thickness up to 10 m, are shown at these figures. Main characteristics of the rocks typical for the Balapan Test site, are represented in Table 5.1.

Table 5.1. Physical-mechanical properties of the Balapan rocks

Rock type	Density, kg/m^3	Porosity, %	Humidity, %	Compressive strength, mPa		Sound velocity km/s		Young's modulus, 10^5 mPa	Poisson's ratio
				dehydrated	moisten	longitudinal	transversal		
Tuff	2760	1.9	0.11	96	113	5.60	3.25	0.71	0.25
Tuffstone	2740	1.4	0.25	71	68	5.54	3.33	0.71	0.25
Tuffo-aleurite	2720	2.2	0.10	98	84	5.69	3.38	0.78	0.26
Shale	2720	0.7	0.24	86	49	5.58	3.02	0.65	0.39
Sandstone	2740	0.8	0.27	80	54	5.58	3.02	0.65	0.39
Porfyrite	2700	2.2	0.20	96	104	4.90	3.20	0.70	0.29
Hornstone	2740	0.9	0.20	64	38	4.99	2.82	0.56	0.26
Granite	2660	1.1	0.28	96	106	5.56	3.22	0.68	0.29
Granodiorite	2660	2.3	-	-	-	4.60	2.85	0.53	0.18
Basalt	2760	3.5	0.35	-	66	4.80	2.97	0.57	0.24

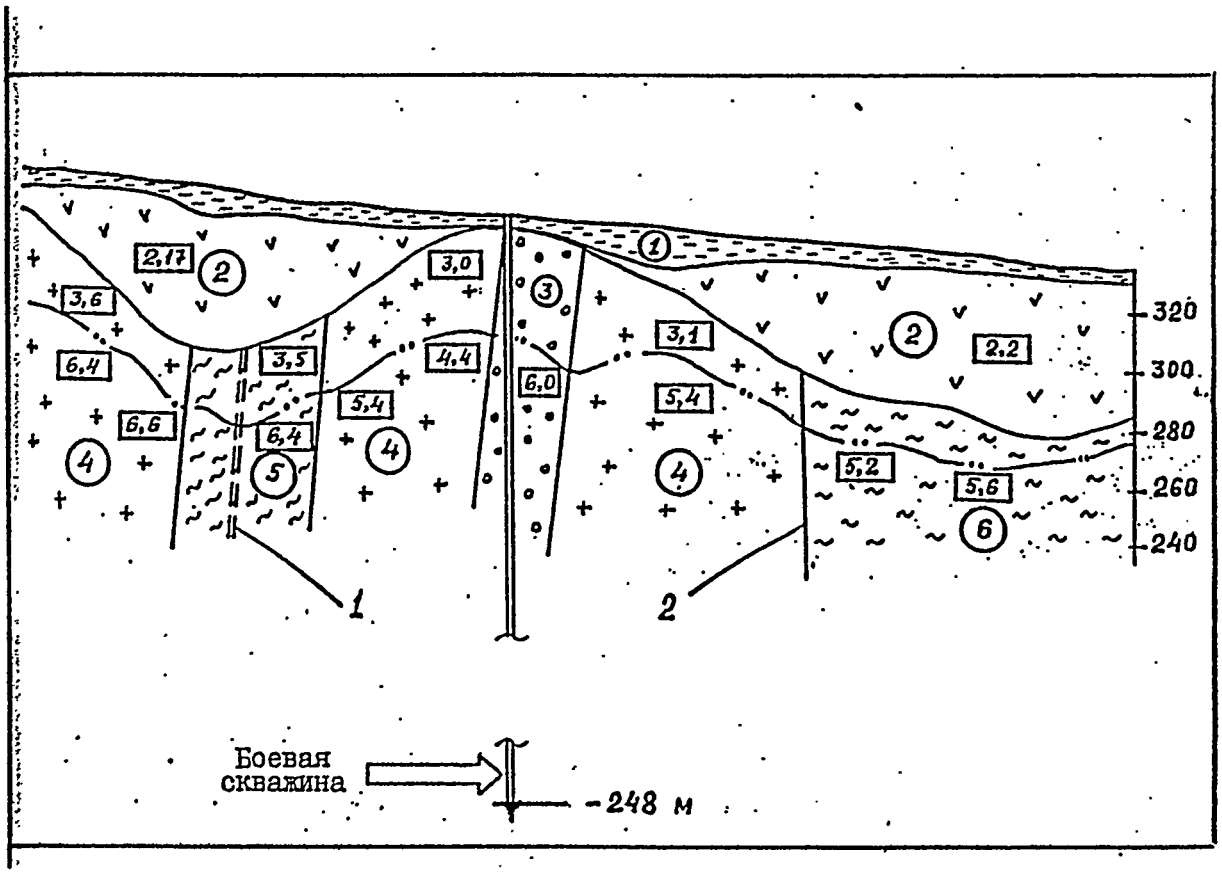

Figure 5.1. Summeridional geological section of the well (the experiment, carried out in July 08, 1989)

==== - deep tectonic fault

——— - tectonic ruptures of higher orders

1 - sandy loams, loamy soils
2 - shale
3 - hornstones
4 - tuffs
5 - granites
6 - tuffstones

- velocity of the small disturbances spreading, km/s (longitudinal)

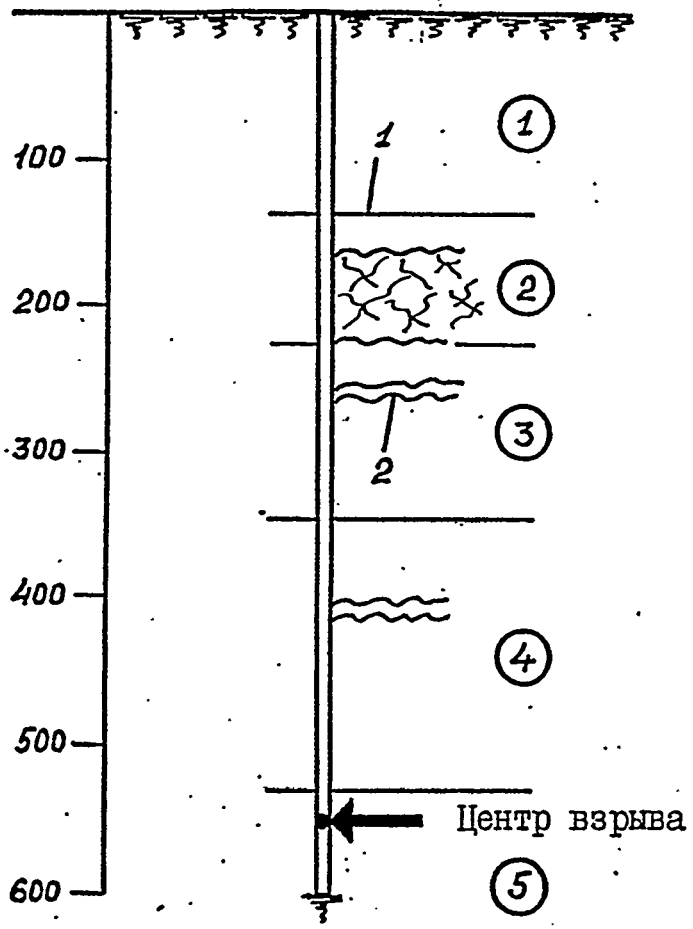

Figure 5.2. Geological section of the well
- boundaries of the main types of rocks
- boundaries of the broken zone
1 - hornstones
2 - slates
3 - tuffstones
4 - hornstones
5 - granitosyenits

Some large and small tectonic disturbances, which divide rock base into tectonic blocks of different orders, might be mark out at the explosion area (Fig. 5.3). Distinctive feature of this area is the presence of the large deep tectonic disturbance of the order I (Kolba-Chingiz regional fault).

Kolba-Chingiz regional fault is the boundary of two biggest folded systems: Chingiz-Tarbagay megaanticlinorium, formed in the Caledonian epoch of the technogenesis and composed from large-fracture rocks of the Middle Cambrian age, and Zaysay megasynclinorium of the Hercynian age, which is represented by the terrigenous deposits of the Lower Carbonic. Both systems are characterized by the intensive folding of different periods and large development of the faults, which predetermined complex block structure of the investigated massif. Thickness of the fault zone in average is estimated as 300 m. This fault zone is retraced on the base of the results of the magneto-prospects by the positive anomaly with power up to 800 nTl.

Large cracks and tectonic disturbances of different orders are accompanied by small tectonic crackness, which is represented by brecciation, rock slatiness, mirrors and furrows of slip along the cracks plane, which were registered at some control wells. Width of the tectonic cracks is equal to 1-5 mm.

Marked tectonic disturbances are accompanied by zones with low velocities of the oscillation spreading and also by step bedding and re-deepening of the refracting boundary (Fig. 5.1).

5.2.1. Results of the measurements of the seismo-explosive influence

Seismic action of the explosion was investigated by means of stationary and mobile seismic control stations. Their position at the Semipalatinsk Test Site is shown at Fig. 5.4. Some of them were dislocated in settlements and others were in field. The epicentre of the explosion, realized in July, 08, 1989, regional faults and boundaries of the Balapan Test area, where well-explosions are, usually, realized, are shown at this figure too. Epicentral distances for seismic control stations were in range from 30 to 200 km.

Summary data from the seismic network, conventional numbers of the seismic stations, their names, distances to the explosion epicentre and magnetic azimuths from the seismostations to the explosion epicentre are represented in Table 5.2.

Seismic stations N° 1-9 were equipped at outcorps of the eroded native rocks and others were located at the mellow sediments with a few tens of meters in thickness.

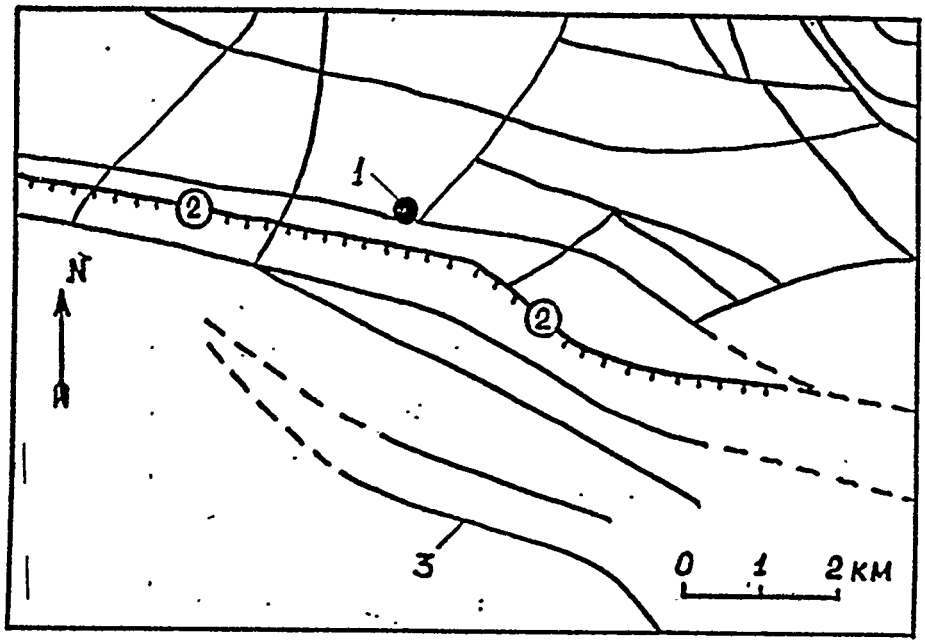

Figure 5.3. Structural-tectonic scheme of the explosion area
- explosion epicentre
- Kolba-Chingiz deep tectonic fault
- tectonic ruptures of higher orders

Table 5.2 Summary data from the seismic network

Number of seismic control station	Name of seismic control station	Epicentral distance, km	Magnetic azimuth to the epicentre, °
1	-	58.4	86
2	-	57.3	90
3	-	56.8	95
4	-	57.6	102
5	-	-	-
6	-	64.8	120
7	-	-	-
8	-	83.2	128
9	-	92.4	134
10	Belogorie	216	148
11	-	71	191
12	Comsomolsk	90	196
13	Semipalatinsk	118	232
14	Znamenka	62	240
15	Sarzhal	29.6	2

Each of these seismic control stations was equipped by six seismometers. They were installed on the concrete base, which was formed preliminary. These seismometers were free, without any attaching.

Two of them registered vertical component of oscillations (Z-component), next two seismometers were installed on the azimuth of the explosion epicenter, they registered horizontal radial component of oscillations (X-component), and last two seismometers registered tangential horizontal component (Y-component). These conventional signs X, Y, and Z will be used at the seismograms shown at Fig. 5.6.

5.2.2 Methods of the registration

Magneto-electric pendulum seismometers SM-3 and VEGIK with their own oscillation period of 2 sec and seismometers S5S with their own oscillation period of 5 sec and decay of 0.5 were used as detectors in this experiment.

Signal from the work winding of the seismometer is proportional to the velocity of the soil oscillations. It was recorded at the paper by means of the light-ray oscillograph with mirror galvanometers, which worked in aperiodical regime with a large decay coefficient (it was about 0.7). In result, the galvanometric channel allowed to register the soil

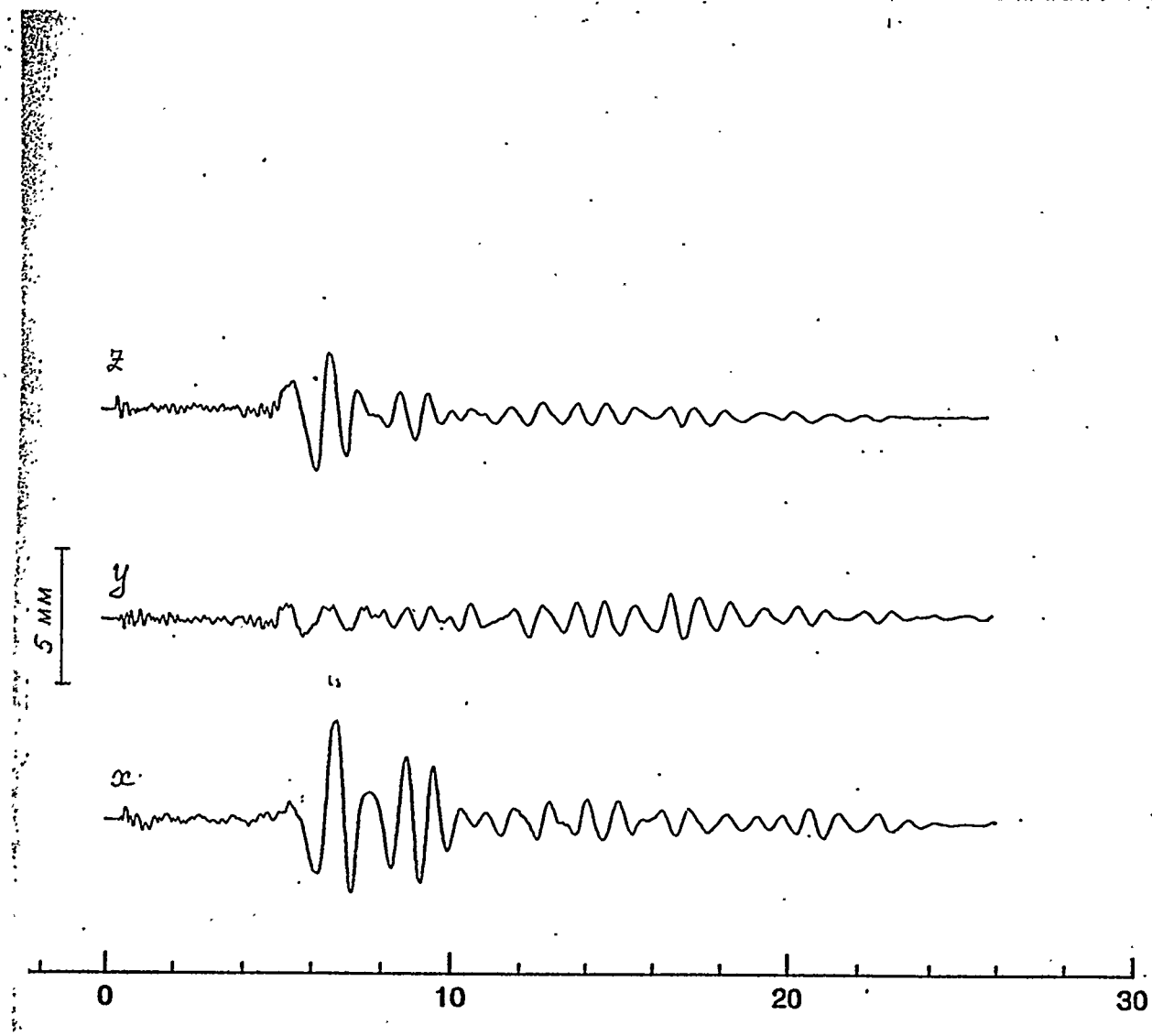

Figure 5.6. Seismic control station N°15, 29.6 km.

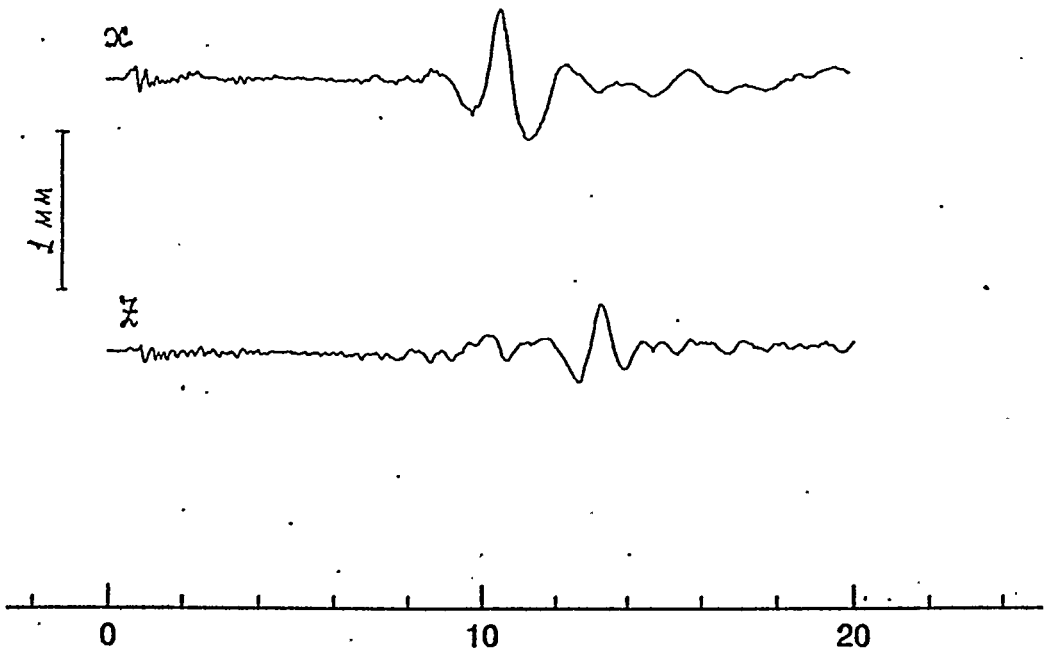

Figure 5.6. Seismic control station N°3, 56.8 km.

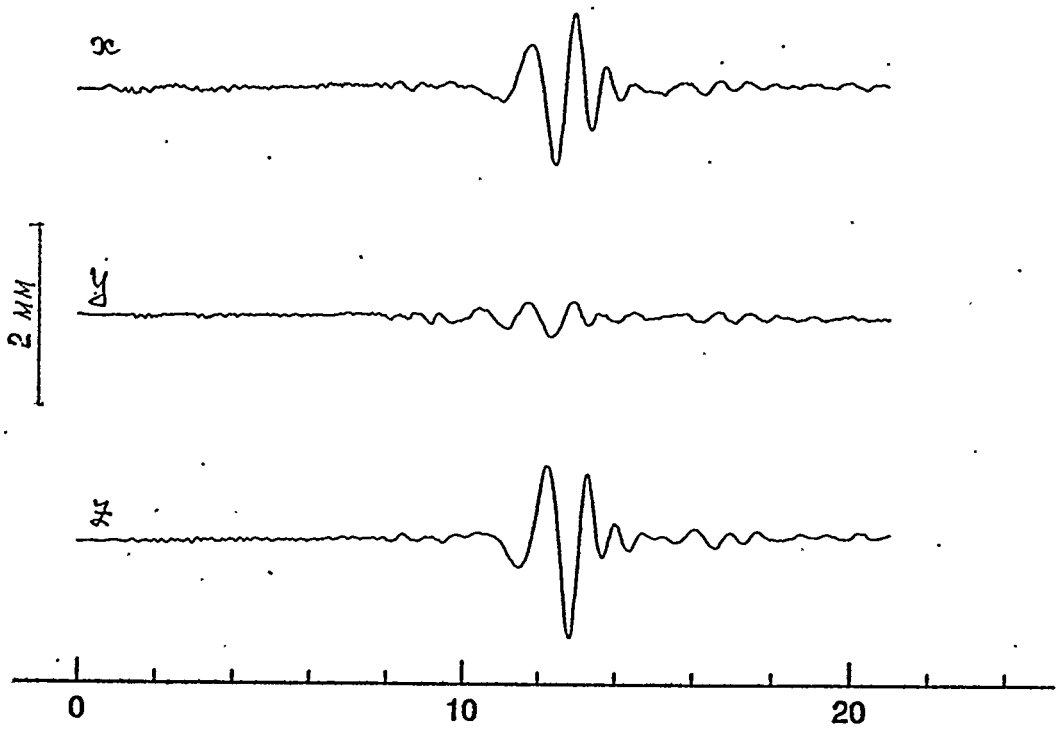

Figure 5.6. Seismic control station N°4, 57.6 km.

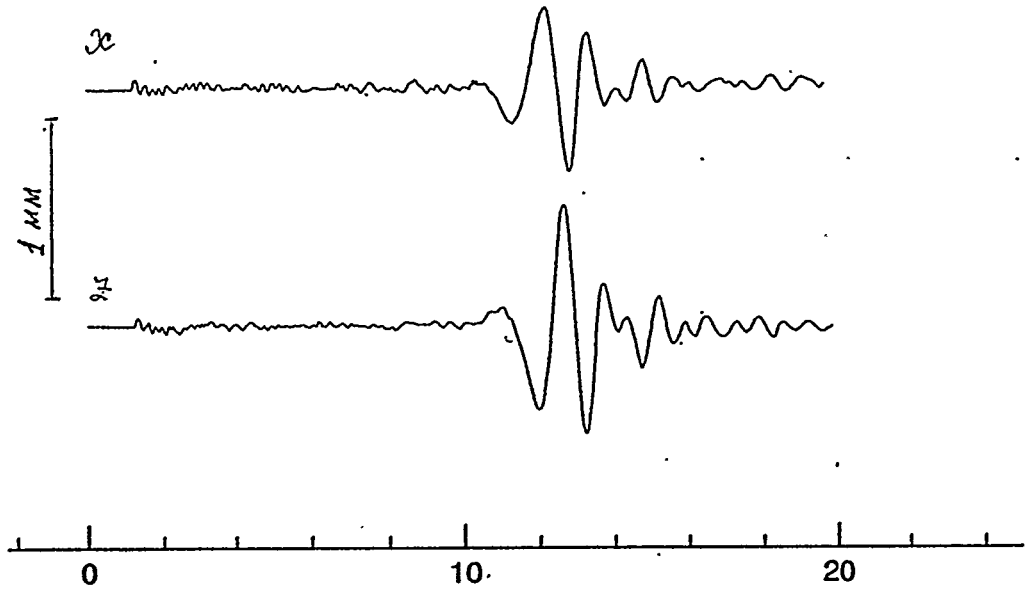

Figure 5.6. Seismic control station N°1, 58.4 km.

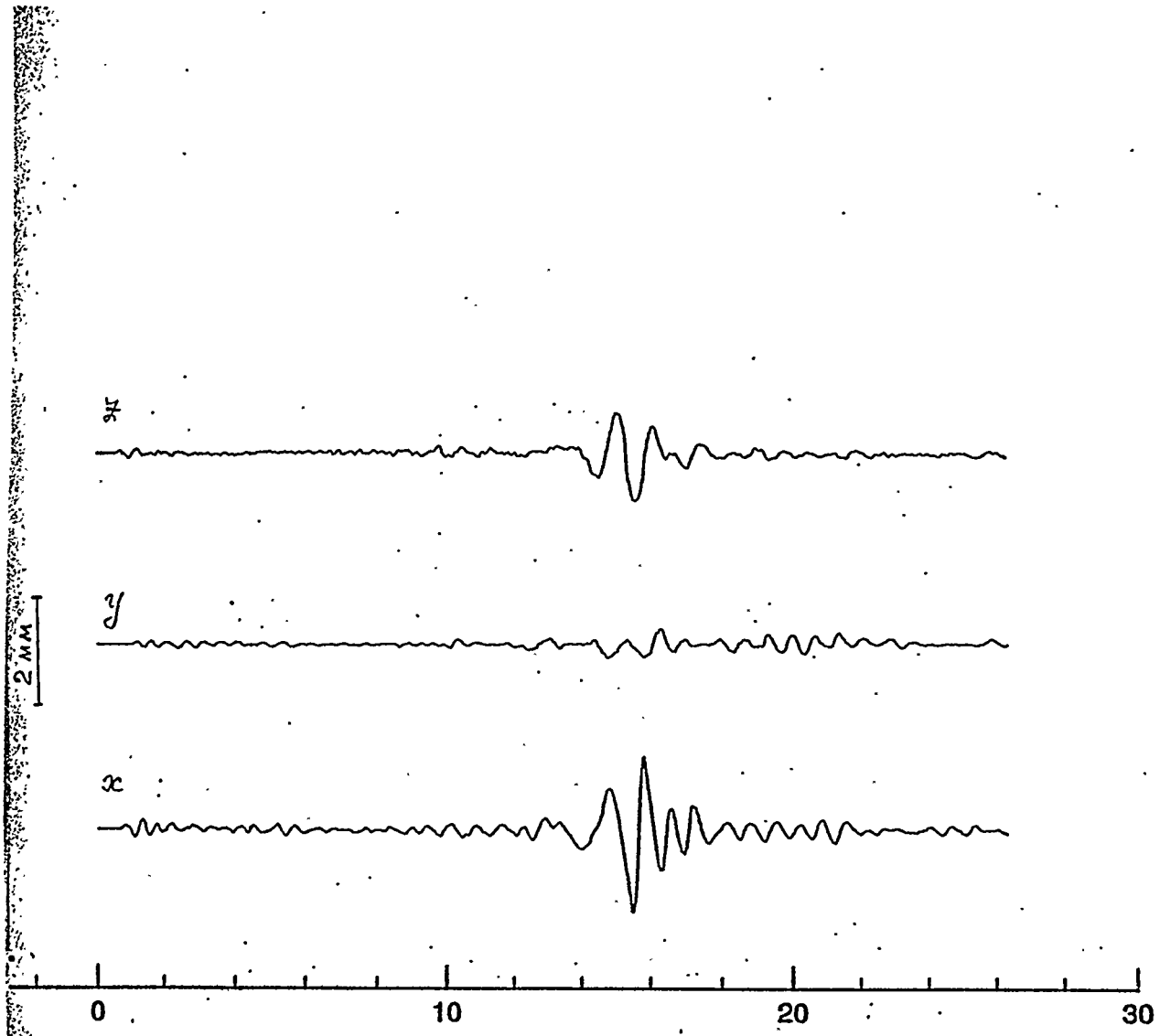

Figure 5.6. Seismic control station N°14, 62 km.

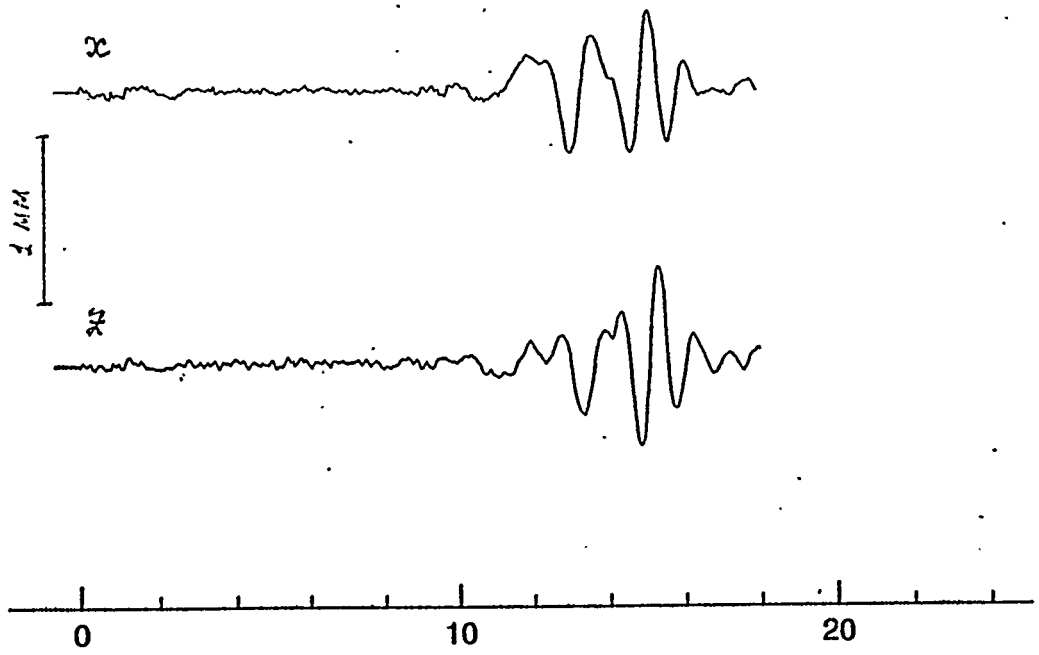

Figure 5.6. Seismic control station N°6, 64.8 km.

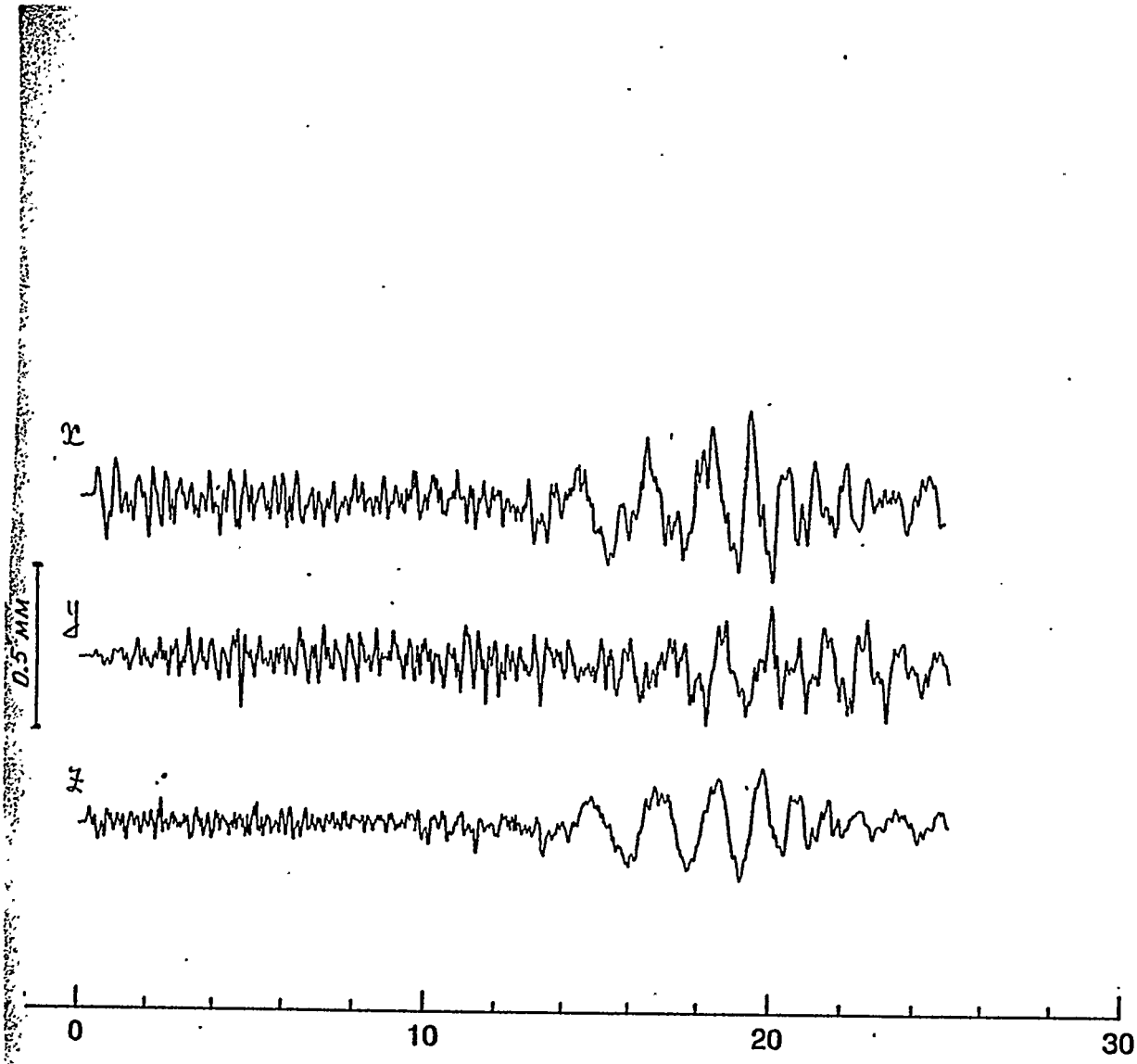

Figure 5.6. Seismic control station N°11, 71 km.

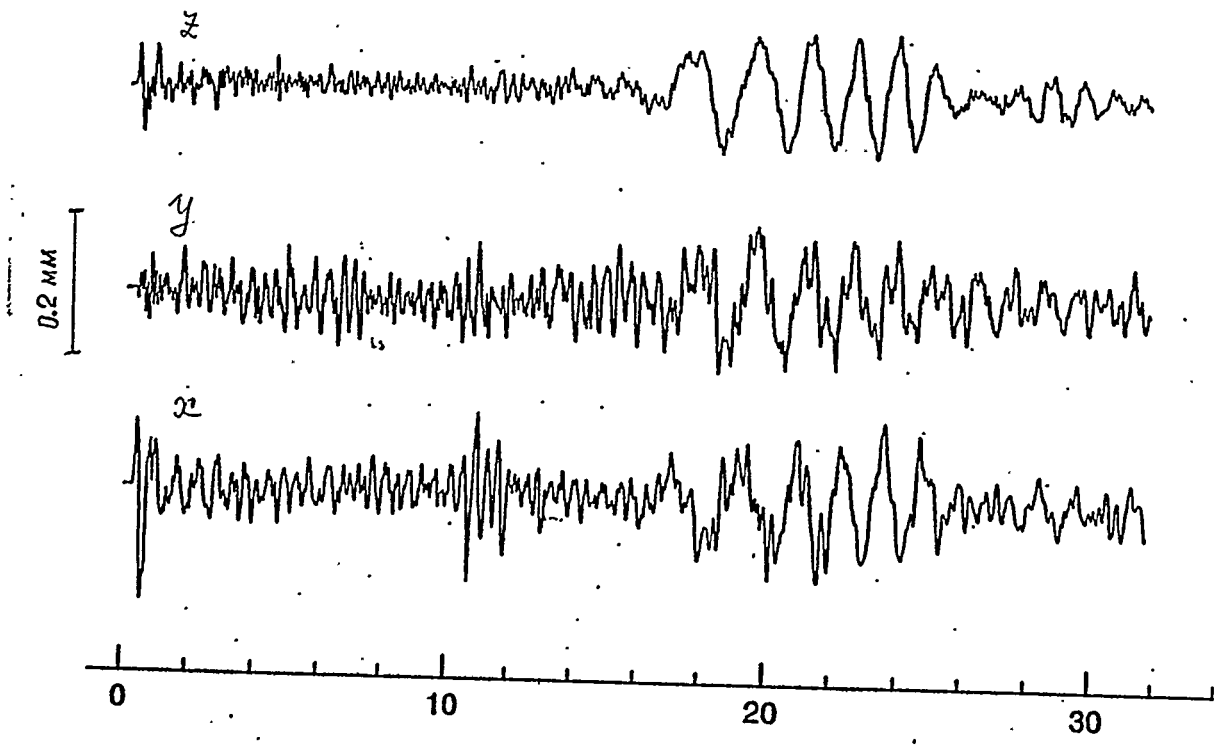

Figure 5.6. Seismic control station N°12, 90 km.

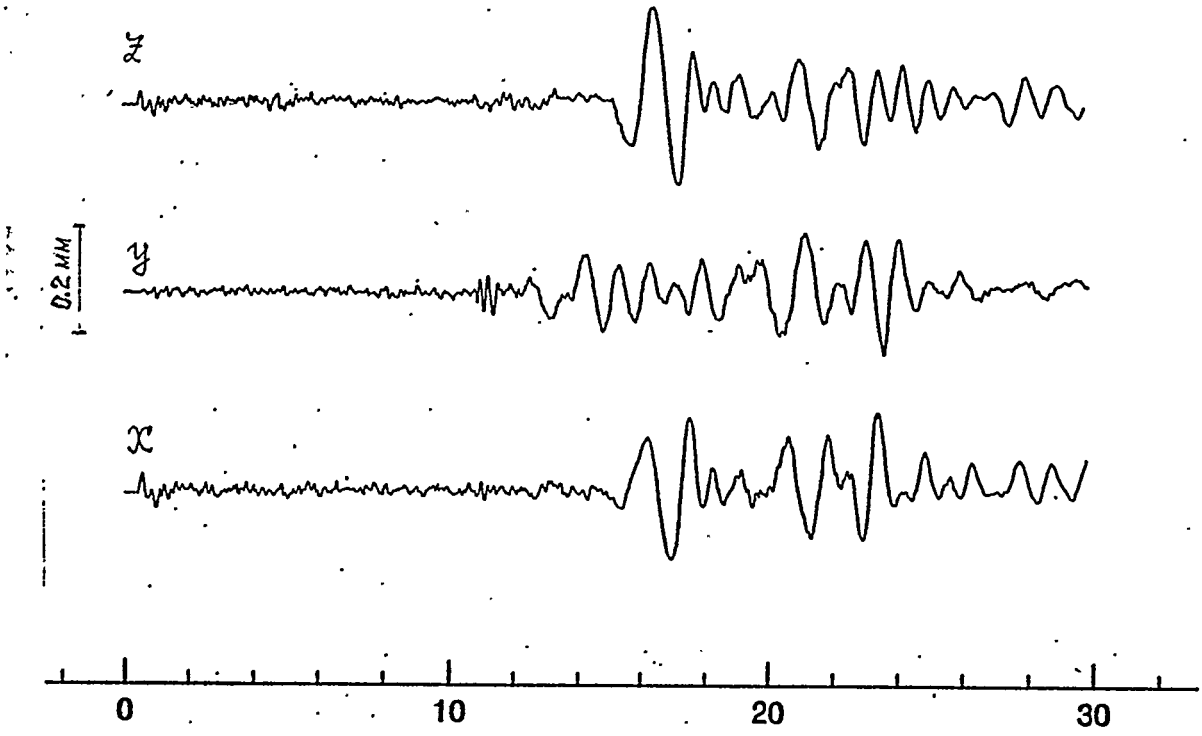

Figure 5.6. Seismic control station N°9, 92.4 km.

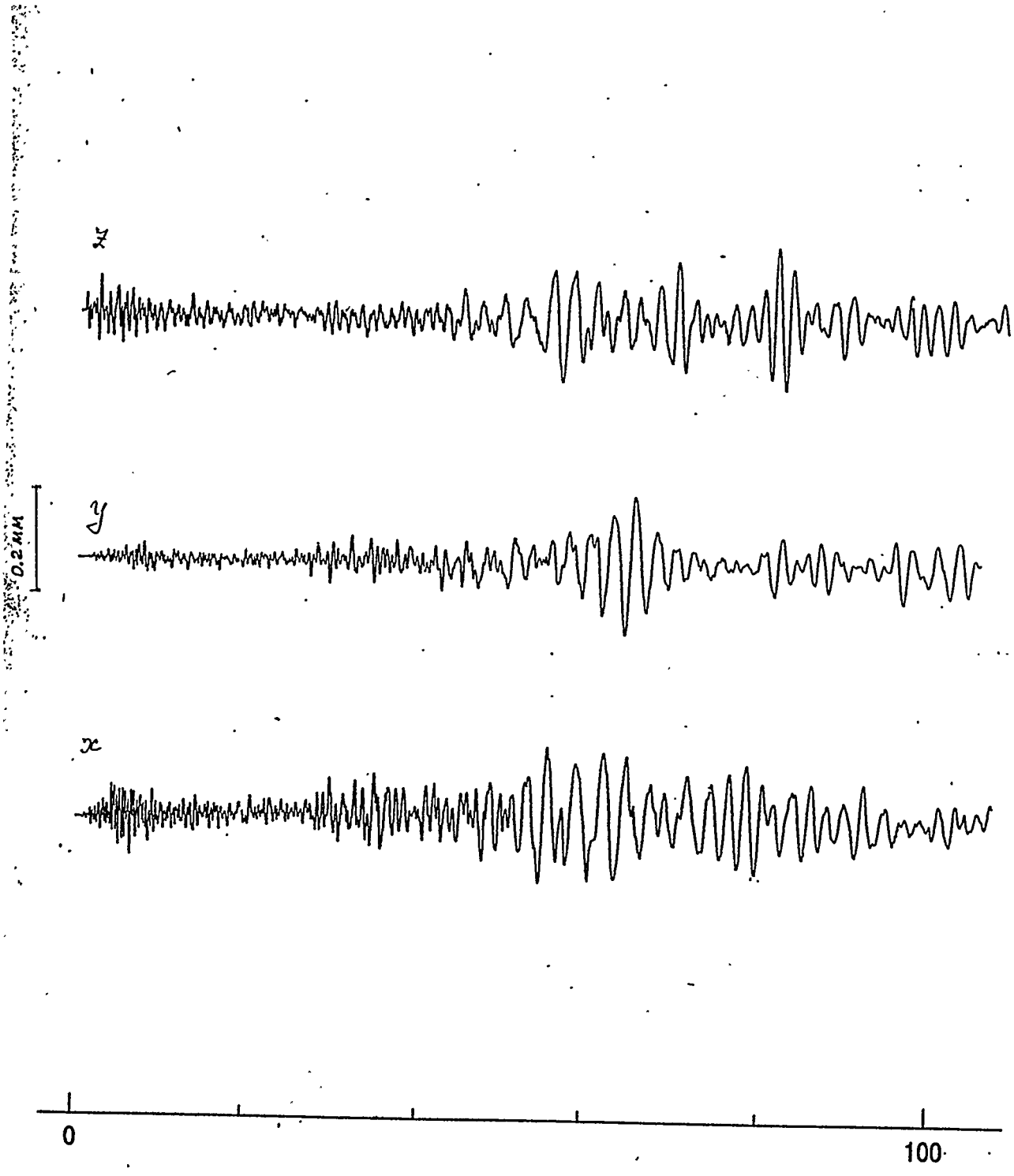

Figure 5.6. Seismic control station N°10, 216 km.

displacements with amplification up to 1200.

Typical amplitude frequency characteristics of the channels are represented at Fig. 5.5. In particular, from these characteristics we can see, that amplification coefficients in the interesting frequency interval from 10 Hz (typical frequency of the body waves) to 0.5 Hz (typical frequency of the surface waves) change at 10-20% for recording channel, equipped by seismometers S5S and SM-3 and nearly in two times for channel with seismometers VEGIK. Real dependence of the amplification coefficients from the frequency were taken into account to determine oscillations amplitudes in the body as well as in the surface waves. The results are presented in Table 5.3.

Dynamic interval of the recording channel is about 46 dB. Maximum error of the determination of the soil displacement amplitude was estimated on the base of numerous results of the measurements by means of several seismometers of the same type at the one control station. It is not greater 6%.

The registration was realized with the paper velocity of 40 mm/s. Simultaneously, one of the galvanometric channel was used to record second time marks. Unfortunately, for the technical reasons, signals from the "common time" service were not recorded in this experiment, so, the seismograms don't represent data of the arrival times for P-waves.

The seismograms were transformed with help of the laser digitizer and this information was written at the hard disk. Some seismograms, registered in July 08, 1989, are shown at Fig. 5.6. X-axis represents time in seconds, but zero time mark for each seismogram is relative.

5.2.3 General characteristic of the seismic oscillations

In zone of the nearest seismicity full wavetrain of oscillations is clearly divided into wavetrains of P-, S-, and R-waves. Oscillation periods in Rayleigh wave is in 4-10 times greater than in body waves. Maximum amplitude of the oscillations velocity, usually, is observed in the body waves, whereas maximum amplitude of the displacement is character to the surface wave.

In Table 5.3 we can see the greatest amplitudes of the displacements W in groups of P-waves and surface R-waves and typical periods of these oscillations T for the explosion, carried out in July, 08, 1989. Fig. 5.7 explains how the parameters in Table 5.3 were received.

Table 5.3 Parameters of seismic waves

Wave parameter	Seismic control stations											
	1	2	3	4	6	8	9	10	11	12	14	15
$W_{r_x}^z$, mm	0.63	0.76	0.53	0.99	0.46	0.55	0.175	0.19	0.2	0.145	1.05	2.1
W_{r_z}, mm	0.70	0.65	0.43	0.75	0.44	0.38	0.12	0.38	0.27	0.19	1.60	3.3
Tr_z^z, sec	1.21	1.36	1.41	1.14	1.06	1.33	1.60	1.69	1.24	1.93	1.20	1.25
Tr_z, sec	1.20	1.20	1.48	1.24	1.0	1.41	1.45	2.41	1.30	2.21	1.0	0.99
Wp_x^z, mm	0.035	0.052	0.029	-	0.018	0.017	0.02	0.063	0.044	0.072	0.13	0.40
Wp^x, mm	0.046	0.07	0.063	0.03	0.020	0.026	0.026	0.037	0.123	0.16	0.21	0.44

Table 3.11 Parameters of seismic waves

Wave parameter	Seismic control stations											
	1	2	3	4	6	8	9	10	11	12	14	15
$W_{r_x}^{max}$, mm	0.63	0.76	0.53	0.99	0.46	0.55	0.175	0.19	0.2	0.145	1.05	2.1
$W_{r_z}^{max}$, mm	0.70	0.65	0.43	0.75	0.44	0.38	0.12	0.38	0.27	0.19	1.60	3.3
Tr_z^{max}, sec	1.21	1.36	1.41	1.14	1.06	1.33	1.60	1.69	1.24	1.98	1.20	1.25
Tr_z^{max}, sec	1.20	1.20	1.48	1.24	1.0	1.41	1.45	2.41	1.30	2.21	1.0	0.99
Wp_x^{max}, mm	0.035	0.052	0.029	-	0.018	0.017	0.02	0.063	0.044	0.072	0.13	0.40
Wp^{max}, mm	0.046	0.07	0.063	0.08	0.020	0.026	0.026	0.037	0.123	0.16	0.21	0.44

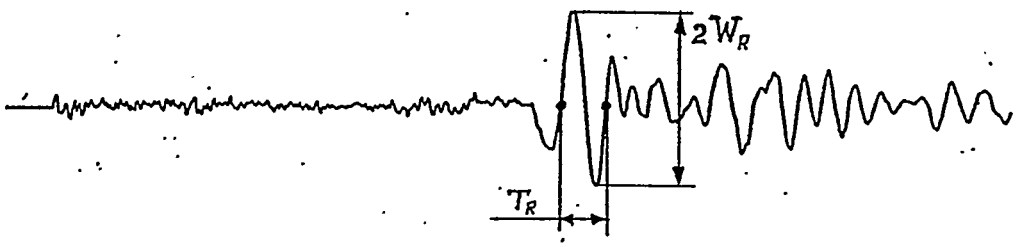

Figure 5.7. Explanation of the method of the seismic wave parameters determination.

It should be noted, that the parameters, presented in Table 5.3, are the average values, determined on the base of two seismograms, registered by two seismometers, which duplicate each other. So, amplitudes and periods of the waves from Table 5.3 might have some distinctions in comparison with the same values, determined from the seismograms, shown at Fig. 5.6.

Wavetrains oscillation have many phases. It is connected with the stratification of the real geophysical medium (the influence of the Conrad and Mochorovich discontinuities is the great). Fig. 5.8 shows experimental hodographs of the different phases of the seismic oscillations, which might be identified and connected with known boundaries in the Earth's crust.

P_1-wave is a primary wave, refracted in the upper layers of the Earth's crust. It is observed in the first arrivals up to 130 km. Its spreading velocity is in range from 5.3 to 6.6 km/s.

P_2-wave is a primary wave, refracted at Mochorovich discontinuity at the angles greater critical. At a distances 100-130 km its amplitude is the greatest. Values of spreading velocity vary from 7.7 and 9.1 km/s.

S_1- and S_2-waves are secondary waves, which are analogous to P_1- and P_2-waves. Velocity of S_1-wave spreading is about 3.1 km/s, and for S_2-wave it varies from 3.9 to 5.5 km/s. From a distance of 100 km S-wave amplitude is the greatest in the body waves group.

Surface R-wave is the wave of Rayleight type. Group spreading velocity is about 2.75 km/s. Polarization in the vertical plane is character for it.

We can see, that these hodographs are practically independent on the azimuth with respect to the explosion epicentre.

5.2.4 Estimation of the explosion power

Seismic network at the Test Site was created to ensure the seismic safety during underground nuclear explosions. At the same time it solves the task of the explosion power determination. The method of the determination of underground nuclear explosions power at the Semipalatinsk Test Site based on the dependence of the maximum displacements W_r^z and W_r^x in the surface Rayleigh wave from the explosion energy q and epicentral distance R. This relation is described by the next equation:

$$W_r = A \cdot q^{0.9} \cdot R^{-1.4}$$

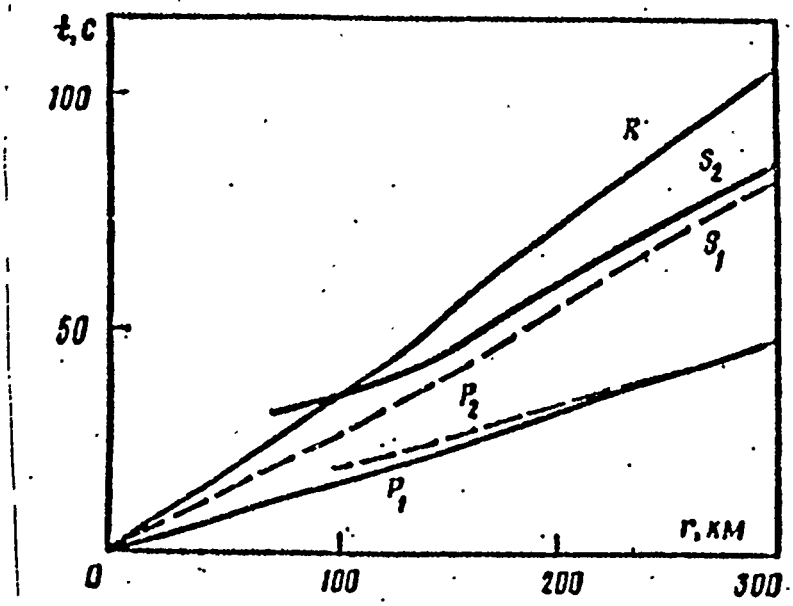

Figure 5.8. Hodograph of primary P_1- and P_2-waves, secondary S_1- and S_2-waves and surface R-waves.

In this ratio A is a coefficient, depending on the seismic control station i, i.e. station coefficient.

Necessity of the use of these station coefficients is illustrated by Fig. 5.9. Rays at this figure are plotted along the azimuths of the seismic control stations. Points on these rays represent amplitudes in the Rayleigh wave for the explosion carried out in July 08 1989, reduced to epicentral distances, i.e. values of $W_r^x \cdot R^{-1.4}$. So, we take into account the decay of the Rayleigh wave at the seismic paths with different lengths. Virtually, Fig. 5.9 represents the diagram of the surface wave radiation. Radius of the circle at the figure is equal to 44.6 mm/km, that is an average value of the reduced amplitude. But, as it is shown at Fig. 5.9, the procedure of the amplitude reduction doesn't transform the diagram of R-wave radiation into the diagram with azimuth symmetry.

Differences between the reduced amplitudes and the average value reach 100% and more. It is natural, that this scattering will remain during the estimation of the explosion power on the base of R-wave amplitude if we'll use the ratio $W(q.R)$ with common coefficient A, which is independent from the control station. (Value of the explosion power is practically proportional to the reduced amplitude $W \cdot R^{1.4}$).

The use of the station coefficients A considerably improve the precision of the explosion power estimation. The coefficients of the seismic control stations at the Test Site were determined empirically on the base of the registration of the surface wave from 10-20 explosions. The station coefficients A_1^x and A_1^z were determined separately from the radial and vertical amplitudes of the waves. Table 5.4 represents logarithms of their values and standard errors of their determination, which are used as weight coefficients in the determination of the explosion power.

Azimuth diagram of the station coefficients A_1^x is shown at Fig. 5.10. The values of these coefficients vary from 3.5 to 12.3. Radius of the circle is equal to the average value of the station coefficients $\bar{A} = 6.4$. The explosion power was estimated with help of the station coefficients and their weights on Xand Z-components of the displacements in the Raylegh wave. It is shown as a diagram at Fig. 5.11, which represents the relation between the explosion power and azimuth of the seismic control station. Radius of the circle at Fig. 5.9 is equal to the average value of the explosion power q = 33 kt. Relative error of the estimation of the average value of the power by means of this method is 6%.

The explosion power, determined on the base of the surface

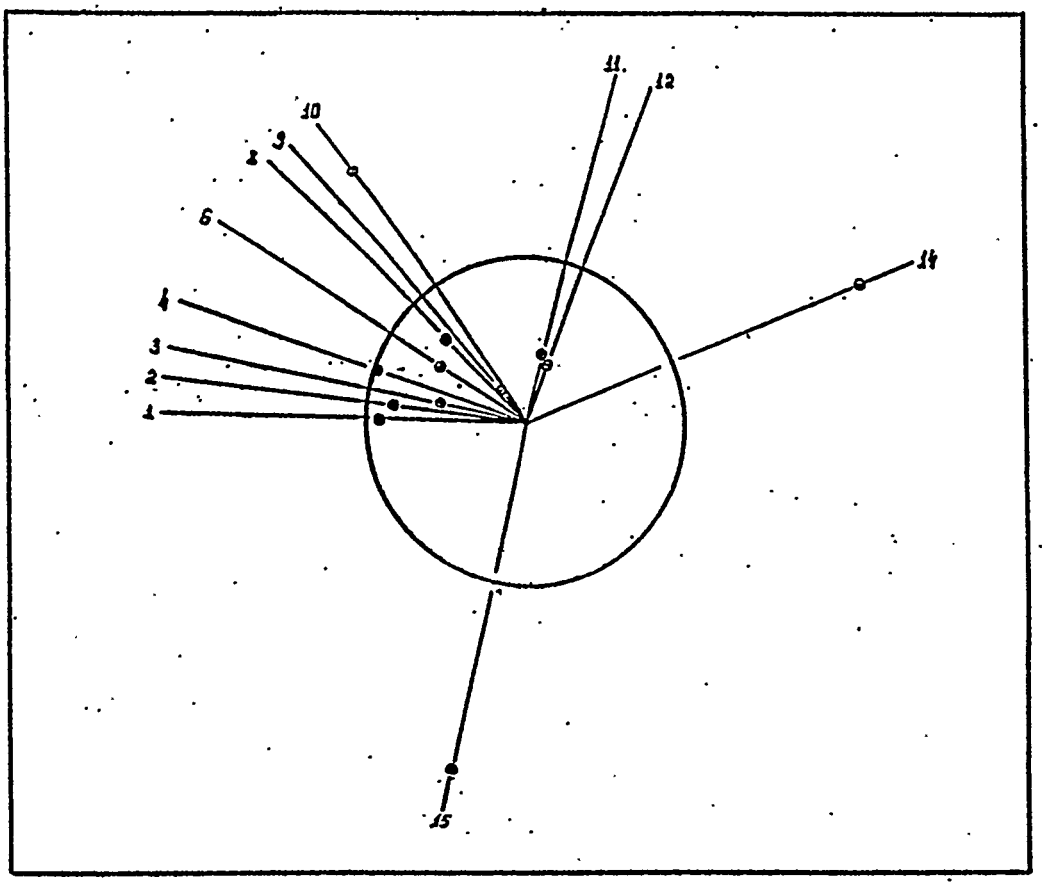

Figure 5.9. Diagram of R-wave radiation with respect to the seismic control station azimuth;
1-15 - directions to the seismic stations.

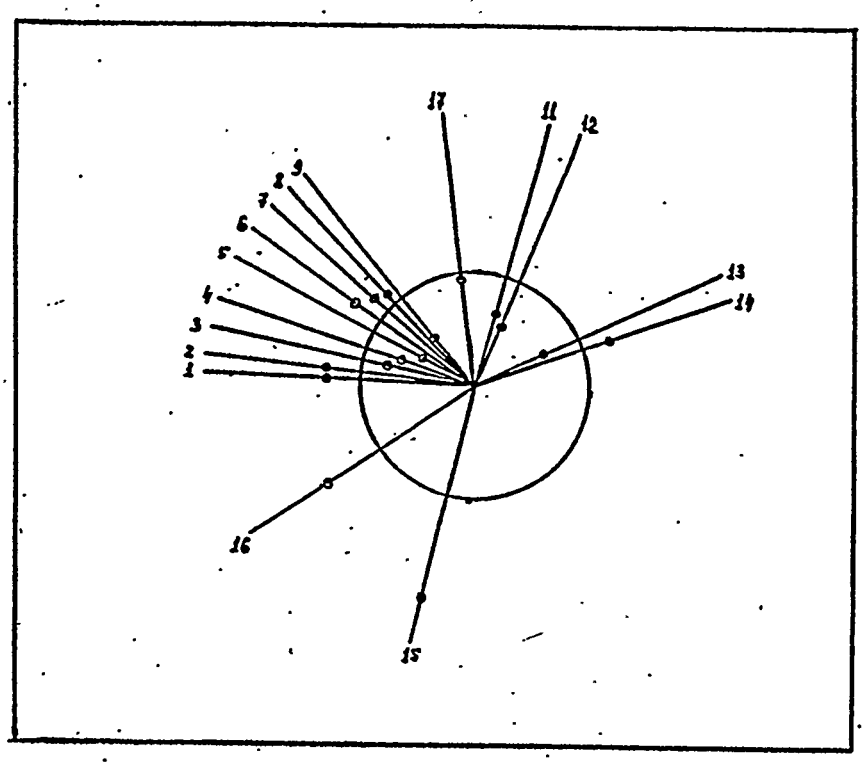

Figure 5.10. Diagram of the station coefficients A_i^x; 1-16 - direction to the seismic stations.

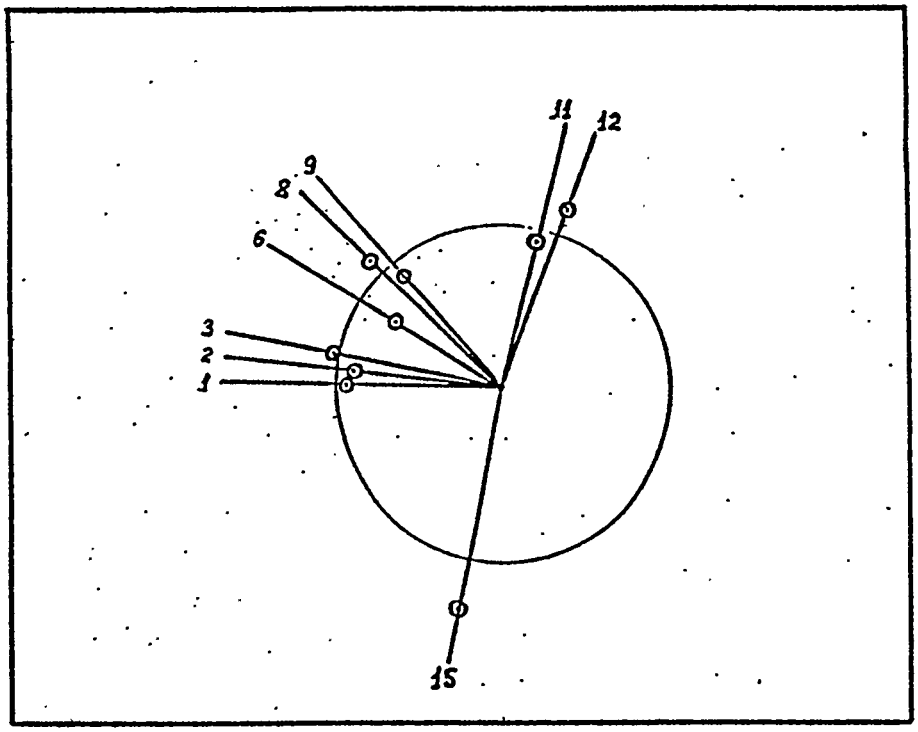

Figure 5.11. Estimated explosion power in dependence on the seismic control stations azimuth;
1-15 - directions to the seismic stations

Table 5.4 Station coefficients

Seismic control station	$\lg A_i^z$	σ_z	$\lg A_i^x$	σ_x
1	0.99	0.087	0.92	0.086
2	1.042	0.088	0.923	0.082
3	0.824	0.068	0.698	0.074
4	0.775	0.115	0.629	0.099
5	0.443	0.078	0.515	0.155
6	0.97	0.105	0.91	0.090
7	0.95	0.096	0.866	0.165
8	1.02	0.160	0.85	0.120
9	0.656	0.133	0.538	0.080
10	–	–	–	–
11	0.63	0.210	0.63	0.121
12	0.48	0.174	0.57	0.173
13	0.65	0.135	0.62	0.154
14	0.80	0.127	0.90	0.122
15	0.92	0.164	1.09	0.170

waves amplitudes, is close to the value of 33 kt, that was determined by physical methods. It is possible, that this decrease of the value of the average "seismic" power is connected with the condition of the location of the explosion hypocentre at zone of the Kolba-Chingiz fault.

Station coefficients take into account both geological conditions at the control station and the features of the path of the seismic wave spreading. It should be noted, that when we speak about the path of the wave spreading, we must consider not only the azimuth of the wave spreading, but also the position of the explosion centre. So, as it was noted early, the Balapan Test Site is divided into tree zones of the epicentres location. All of these zones have their own set of the station coefficients. It is significant to note, that the boundaries of the zones coincide with the Chinrauz and Shagan tectonic faults, crossing the Balapan Test Site. So, it is possible to consider, that the station coefficients also reflect the influence of the faults and block structure of the Test Site on the seismic effects of the explosion.

Using of the station coefficient in order to solve the problem of the estimation of the explosion power on the base of the surface waves in zone of the nearest seismicity is analogous to the method of the magnitude corrections, which is used to determine the explosion power from the body wave magnitude at teleseismic distances.

5.2.5 Passing of the seismic waves through the fault

One of the main factors, which determine the diagram of the surface wave radiation with complex asymmetry and the values of the station coefficients, is the existence of the tectonic faults at the path of the wave spreading. These faults form "the path features".

Experimental data from the explosion realized in July, 08, 1989 and some other explosions allow to estimate the influence of the Chinrauz and Shagan tectonic faults, which are located to the north from the epicentre of the explosion carried out in July 08 1989. The simplest way to study this question is to determine the parameters of the Rayleigh wave, registered at the paths, which cross and don't cross these faults.

Fig. 5.12 shows the map-scheme of the region, where we can see position of the explosion epicentres with number 1-6 and seismic control stations N° 1 and N° 12. Seismograms from these explosions were registered at these stations and studied. Epicentre with number 1 corresponds to the explosion, realized in July 08, 1989. From the figure we can see, that the epicentres 1-4 are separated from the epicentres 5-6 by the Chinrauz and Shagan faults. Seismic paths from the explosions 5-6 to the seismic control station N° 1 passe through the faults, but the paths from the explosions 1-4 don't cross these faults.

As concerns to the seismic control station N° 12, the situation is exactly opposite. In others details (such as azimuths of the wave spreading, epicentral distances, existence of some other faults of the lower order and heterogeneousnesses on the way of the wave spreading) the seismic paths from these explosions are practically identical.

Tables 5.5 and 5.6 represent the epicentral distances and displacements in the Rayleigh wave at the seismic control stations N° 1 and N° 12 for six explosions. These data and explosions powers were the base in order to estimate the next reduced wave amplitudes, which are represented in the table too:

$$W^* = W_r^x \cdot q^{-0.9} \cdot R^{1.4}$$

The average values of the reduced amplitudes were determined for the experiments 1-4 and 5-6 separately. It is possible to see from Table 5.5, that the wave amplitudes at the control station N° 1 after the explosions 5-6 are in 1.5 times less than after the explosions 1-4. This difference might be explained by the weaken influence of the Chinrauz and Shagan faults.

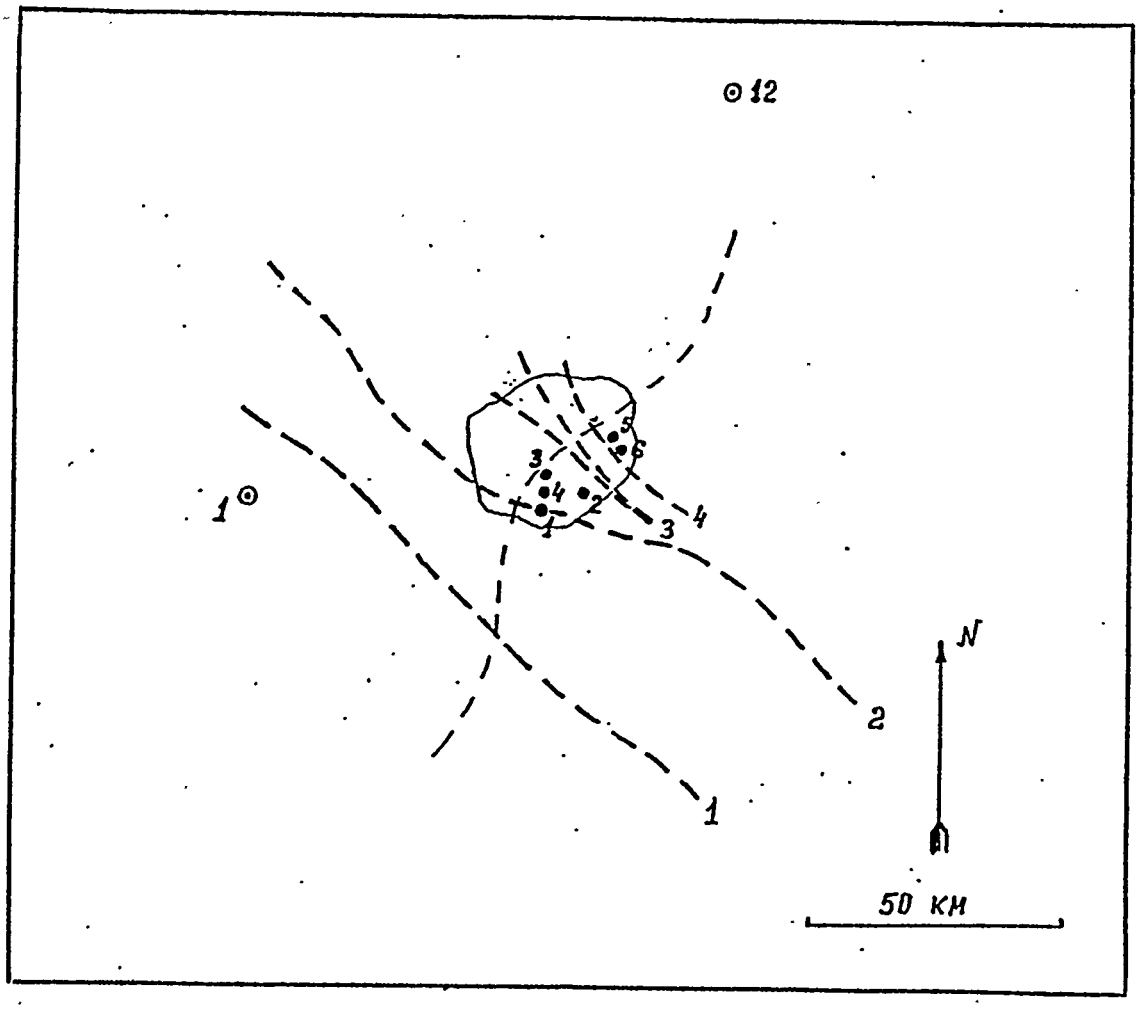

Figure 5.12 Map-scheme of the position of explosions epicenters and seismic control stations
- explosions epicentres
- seismic control stations
- faults: 3 - Chinrauz, 4 - Shagan

Table 5.5

N	q, kt	R, km	W_r^x, mm	W^*	$\overline{W}^*$
1	35	58.4	0.7	8.47	8.4
2	150	67	1.98	7.61	
3	133	60.9	2.41	9.30	
4	140	60.7	2.22	8.17	
5	142	74.8	1.21	5.87	5.63
6	146	75.3	1.14	5.47	

Table 5.6

N	q, kt	R, km	W_r^x, mm	W^*	$\overline{W}^*$
1	35	90	0.19	4.22	3.09
2	150	83.2	0.51	2.72	
3	133	80	0.47	2.66	
4	140	81.4	0.50	2.77	
5	142	71.2	1.04	4.71	5.04
6	146	73.8	1.15	5.36	

Analogous results are observed in Table 5.6. The wave amplitudes at the control station N° 12 after the explosions 1-4 are in 1.6 times less than after the explosions 5-6. Naturally, we can suppose, that in this case the cause of that result consist in the decay of the wave after its crossing of the Chinrauz and Shagan tectonic faults. The weaken influences of the faults are practically identical for the explosions 1-4 as well as for the explosions 5-6, i.e. it is independent from the direction of the wave spreading through the faults.

This effect explains the division of the Balapan Test Site into three zones exactly along the Chinrauz and Shagan faults for the created seismic network and the introduction of the own set of the station coefficients for all zones. Besides that, it demonstrates the contribution of the influence of these two faults in the asymmetry of the experimental registered diagram of the surface wave radiation.

The model of the fault in the absolute elastic medium as a flat crack with elastic filler was investigated early. From this model the decay of the amplitude of the wave passing through the fault is connected with its reflection from the boundary between the mediums with different acoustic cruelty. In particular, the amplitude of the waves, which are close to the harmonic waves with characteristic period T and spreading velocity c decreases in $K = (1+g^2)^{1/2}$ times, where $g = \pi L\gamma/cT$, when the wave passes through the fault with the width of L. Parameter $\gamma = \rho c^2/\rho_p c_p^2$ is the ratio of the massif cruelty to the cruelty of the fault filler, i.e. it is considered as the fault "contrast". We have the next experimental data: decay of R-wave amplitude K = 1.5, its period T = 1 sec, spreading velocity c = 2.75 km/s.

Using these data and total width of the Chinrauz and Shagan faults as L = 200 m we can to determine the contrast of these faults. It is equal to γ = 5. Subsequent geophysical investigations of these faults will give an opportunity to receive reliable information about them, which is necessary in order to estimate the spreading of the seismic waves through the faults.

The records of the tangential horizontal oscillations at the seismic control stations N° 9 and N° 12 are considerably stood out against the others experimental seismograms shown at Fig. 5.6. At these seismograms the arrival of the transversal wave SH with significant amplitude is shown clearly. This wave is the evidence of the yield of the tectonic energy after the explosion, carried out in July 08, 1989. Unfortunately, after this explosion the records of the tangential component were made only at a few seismic stations, so it is impossible to estimate the yield of the tectonic energy on the base of the data of the nearest seismicity.

*This work was performed under the auspices of the U.S. Department of Energy by Lawrence Livermore National Laboratory under contract No. W-7405-Eng-48.